UNIVERSITY OF CALIFORNIA SAN DIEGO

Electrical tomographic methods for defects detection in advanced structures

A Dissertation submitted in partial satisfaction of the requirements
for the degree Doctor of Philosophy

in

Structural Engineering

by

Yening Shu

Committee in charge:

Professor Kenneth J. Loh, Chair
Professor Jiun-Shyan Chen
Professor Hyonny Kim
Professor Tse Nga Ng

2023

The Dissertation of Yening Shu is approved, and it is acceptable in quality and form for publication on microfilm and electronically.

University of California San Diego

2023

DEDICATION

This thesis is dedicated to my parents, Xiaoqin Zhai and Xiaobao Shu. I am forever grateful for the values you have instilled in me and the opportunities you have provided. Thank you for being my rock, my inspiration, and my source of strength.

TABLE OF CONTENTS

LIST OF FIGURES

LIST OF TABLES

ACKNOWLEDGEMENTS

I would like to take this opportunity to express my sincere appreciation to all the people who have supported me throughout my PhD journey at UC San Diego.

First and foremost, I am deeply grateful to my advisor, Professor Kenneth Loh, for his exceptional guidance, unwavering support, and mentorship. His expertise, dedication to research, and insightful feedback have been invaluable in shaping the direction of my work. I am especially grateful for the opportunity to work in his lab during my master's studies, which sparked my interest in tomographic methods for structural health monitoring and ultimately led me to pursue my PhD.

I would like to extend my heartfelt gratitude to Professor Martin Schagerl at JKU Linz in Austria. Through the opportunity provided by Professor Loh and Professor Schagerl, I had the privilege of studying abroad in the Institute of Structural Lightweight Design, where I received invaluable support and guidance in my research. His expertise and collaborative spirit have significantly contributed to the development of my work.

I would also like to express my deep appreciation to my parents for their unwavering support and belief in my abilities. Their encouragement, sacrifices, and constant love have been the foundation of my academic journey, and I am forever grateful for their support.

I want to acknowledge and thank my lab mates for their camaraderie, support, and willingness to lend a helping hand. Their collaboration, insightful discussions, and shared experiences have enriched my research and made the journey more fulfilling.

Furthermore, I want to express my heartfelt gratitude to my boyfriend, Zihan, for his support, encouragement, and understanding throughout my PhD journey. His constant presence and words of encouragement have been a source of strength during the challenging and frustrating times. I am truly grateful for his companionship.

Finally, I want to extend my thanks to all the funding agencies and grants that have provided financial support for my research. Their support has made it possible for me to pursue my PhD and advance my studies in the field.

I am deeply thankful to everyone mentioned above, as well as to the countless others who have contributed to my academic and personal growth during my time at UC San Diego. Your guidance, support, and belief in my abilities have been instrumental in my achievements, and I am honored to have had your presence in my life.

Chapter 3 is, in full, currently being prepared for submission for publication of the material. Shu, Yening. The dissertation author was the primary investigator and author of this material. This project was conducted in the Institute of Structural Lightweight Design at Johannes Kepler University Linz and supported by the Christian Doppler Laboratory for Structural Strength Control of Lightweight.

Chapter 4 is in full, a reprint of the materials as in appears in "Multi-Defect Detection in Additively Manufactured Lattice Structures Using 3D Electrical Resistance Tomography." Shu, Yening, Saptarshi Mukherjee, Tammy Chang, Abigail Gilmore, Joseph W. Tringe, David M. Stobbe, and Kenneth J. Loh, *Sensors* 22.23 (2022), and “Electrical Resistance Tomography and Machine Learning for Lattice Structure Damage Detection.” Shu, Yening, and Kenneth J. Loh,

Measurement Science and Technology (2023). The dissertation author was the primary investigator and author of this material.

Chapter 5, in part, is currently being prepared for submission for publication of the material. Shu, Yening, Li, Sijia, and Loh, Kenneth J. The dissertation author was the primary investigator and author of this material.

Chapter 6, in part, is currently being prepared for submission for publication of the material. Shu, Yening, Dela-cueva, Janelle, Kim, Hyonny, and Loh, Kenneth J. The dissertation author was the primary investigator and author of this material.

VITA

2016 Bachelor of Science in Civil Engineering, Hunan University

2018 Master of Science in Structural Engineering, University of California San Diego

2023 Doctor of Philosophy in Structural Engineering, University of California San Diego

ABSTRACT OF THE DISSERTATION

Electrical tomographic methods for defects detection in advanced structures

by

Yening Shu

Doctor of Philosophy in Structural Engineering

University of California San Diego, 2023

Professor Kenneth J. Loh, Chair

Advanced structures, including Carbon Fiber Reinforced Polymer (CFRP) composites and lattice structures, have drawn significant attention due to their exceptional mechanical performance. However, their quality and mechanical performance can degrade because of defects introduced during manufacturing or in-service. This thesis proposes non-invasive electrical tomographic imaging techniques, electrical resistance tomography (ERT), electrical impedance

tomography (EIT), and electrical capacitance tomography (ECT), for damage detection in advanced structures. These techniques leverage boundary measurements to reconstruct the interior electrical properties distribution of the advanced structures, such as electrical conductivity and permittivity, which are directly correlated to structural damage maps. However, classical electrical tomographic methods face challenges when applied to anisotropic CFRP composites and suffer from limited central sensitivity. To overcome these limitations, this thesis incorporated specific modifications, including the use of electrical conductivity tensors and normalized sensitivity maps. These enhancements improve the applicability of electrical tomographic methods on CFRP composites and lattice structures with complex geometries. Also, the use of smart paint and frequency-difference EIT was explored to enhance damage detection in painted advanced structures without the need for baseline measurements. Additionally, to increase computational efficiency for defect detection, machine learning methods are integrated with tomographic techniques. Simulation and experimental studies were conducted to evaluate the performance of the proposed techniques, and comparisons were made with classical solvers. The results demonstrate the effectiveness of the proposed ERT, EIT, and ECT methods in detecting damage in advanced structures. This comprehensive investigation provides valuable insights for damage detection in advanced structures, contributing to more efficient and effective inspection processes.

CHAPTER 1 INTRODUCTION

1.1 Advances Structures

Lightweight engineering has emerged as a critical area of research and development in recent years, driven by the need to reduce weight while maintaining or improving performance in a variety of applications [1–3]. Lightweight engineering is particularly important in automotive, naval, and aerospace industries, where weight reduction can translate into significant fuel savings, increased range, and improved overall functionality [4–7]. Lightweight engineering relies heavily on advanced materials and structures, such as composites, polymers, and alloys, and sophisticated design techniques that optimize structural efficiency. Among these different types of advanced structures, carbon fiber reinforced polymer (CFRP) composites and lattice structures, have become increasingly important in the field of lightweight engineering due to their superior mechanical properties. These materials offer high strength and stiffness with low weight, making them ideal for use in lightweight engineering applications where weight reduction is critical [2,3].

CFRP is a composite material consisting of carbon fibers embedded in a polymer matrix. The unique properties of CFRP composites stem from the arrangement of multiple layers of carbon fibers, where typically each layer is laid out in a specific direction within the polymer matrix [8,9]. This orientation allows the carbon fibers to bear the majority of the load, while the polymer matrix serves as a binding agent, resulting in a material that is both strong and lightweight. Another significant advantage of CFRP composites is their exceptional fatigue performance. Fatigue failure, which occurs under cyclic loading, is a critical concern in lightweight engineering. Traditional materials can experience fatigue failure over time, limiting their durability. However, CFRP composites have inherent resistance to fatigue due to their ability to dissipate energy through fiber

bridging and matrix toughening mechanisms [10]. This property allows them to endure millions of load cycles without significant degradation, making them suitable for applications subjected to dynamic loading, such as aircraft wings or wind turbine blades.

Another class of lightweight structures is lattice structures, which are complex networks of interconnecting beams and nodes that distribute loads efficiently throughout the structure [11,12]. Lattice structures are bio-inspired 3D configurations of repeated and open unit cells [3,13]. Relative to conventional bulk materials, topologically ordered lattice structures can exhibit impressive mechanical strength, stiffness, thermal, and electrical properties while using significantly less material. In other words, they possess higher strength- and stiffness-to-weight ratios. These advantages have led to their broad applications in advanced lightweight naval, automobile, aerospace, and other engineered structures [4–6,11]. Moreover, lattice structures exhibit superior energy absorption capabilities. The interconnected lattice framework distributes external forces across multiple struts or beams, allowing for efficient energy dissipation during impact or dynamic loading events[14]. This property makes lattice structures ideal for lightweight applications requiring impact resistance and crashworthiness. Lattice structures provide a compelling solution for lightweight engineering due to their exceptional strength-to-weight ratio, energy absorption capabilities, and design flexibility. These structures offer significant weight savings while maintaining structural integrity, enabling the development of efficient, lightweight, and high-performance structures for a wide range of applications.

For both these types of emerging advanced structural materials, their real functionality relies heavily on their structural integrity, which can be compromised by damage or defects that may occur during manufacturing or operations. For instance, CFRP composites can be vulnerable to delamination, fiber misalignment, and voids or porosity, which can degrade their mechanical

performance and lead to premature failure [15,16]. Similarly, lattice structures are susceptible to defects such as cracking, buckling, and deformation, which can compromise their structural integrity and reduce their load-carrying capacity [17–19]. The detection and characterization of such defects are critical to ensure the reliable and safe operations of these advanced structures. Therefore, there is an urgent need for the development of effective and efficient methods for damage detection in CFRP composites and lattice structures.

1.1.1 Defects in CFRP Composites

The usual manufacturing process for CFRP composites involves several steps, including the layup of carbon fiber sheets, impregnation with resin, and curing under heat and pressure. The layup process involves the orientation and placement of carbon fiber sheets in a specific pattern to achieve the desired mechanical properties [20]. The impregnation process involves the infiltration of the carbon fiber sheets with a resin matrix, which binds the fibers together and provides additional mechanical properties. Finally, the curing process involves the application of heat and pressure to the composite to solidify the resin matrix and create a strong and durable material [8,9].

However, during the manufacturing process, defects such as voids, delamination, fiber misalignment, and porosity can occur due to various factors, including improper processing conditions, inadequate quality control measures, and operator error [1,15,16]. When the porosity or void content increases, the mechanical properties of the material can be severely affected. Voids can cause stress concentrations during loading, leading to local failures and cracks. These local failures can exacerbate stress concentrations and reduce the overall strength and stiffness of the material. Misalignment and delamination are the other two types of defects that can significantly influence the performances of CFRP composites. Misalignment can occur when the fibers are not

perfectly aligned in the matrix, leading to stress concentrations at the interface between the fibers and the matrix [21]. This inefficient load transfer causes some fibers to bear more load than others, leading to higher stresses and ultimately failure. Delamination occurs when there is a separation between layers in the composite material, leading to a reduction in the mechanical properties of the material [16,22]. These defects too can reduce the load-bearing capacity of the material, leading to premature failure.

During the operational life of CFRP composites, they may experience various loads and environmental effects that can cause damage or even failure. For example, unexpected impacts, such as collisions or drops, can cause visible as well as nonvisible damage, including delamination, matrix cracking, and fiber breakage. Other severe loadings, such as cyclic loading, can cause fatigue damage, leading to microcracks and progressive failure of the material [23]. Furthermore, environmental effects such as moisture, temperature variations, and exposure to ultraviolet radiation can cause degradation of the material over time, leading to a reduction in mechanical properties and ultimate failure [24]. Therefore, it is crucial to inspect and monitor the structural health of CFRP composites during their operational life to detect and address any damage or degradation in a timely manner and ensure the optimal performance and reliability of the material.

1.1.2 Defects in Lattice Structures

Lattice structures are widely used in lightweight engineering due to their high strength and stiffness while minimizing weight. Increasing performance demands for lightweight engineering applications means that lattice structures need to be fabricated with greater complexity and with smaller feature sizes. Conventional manufacturing processes, such as wire weaving [25], high-temperature forming and diffusion bonding [12], and the interlocking method [26], are unsuitable

and too time-consuming for fabricating lattice structures with complex nodal connections. Recent advances in additive manufacturing (AM) have enabled methods to realize cellular lattice structures with intricate geometries [27,28]. Some of the widely used AM methods include fused deposition modeling [29] and stereolithography [30] for polymer-based structures, as well as extrusion [27], powder bed fusion [31], and direct ink write [32] for metallic cellular lattice systems.

Despite the ability to use AM to fabricate complex cellular structures, their functional performance strongly depends on manufacturing quality. The presence of minor defects could compromise the structural integrity of the entire part [17]. For instance, nozzle clogs, micro-voids, and pores that occur during extrusion or uncontrolled thermo-mechanical behavior in powder bed fusion may induce cracks, shrinkage, uneven surfaces, and nodal disconnections in the struts [18]. During storage, transit, or use, these weakened struts are prone to stress concentrations, which can lead to defect propagation, broken struts, and partial or complete lattice structure failure [19]. Therefore, quality assurance and control of AM parts require that the type of defects and damage locations be identified whether they are incurred during manufacturing or when in service.

1.2 Current State-of-the-Art of Non-destructive Evaluation Methods

Considering the possible damage occurrence in advanced structures during manufacturing or operations, particularly due to easily overlooked damage precursors that could propagate and compromise structural integrity, it becomes crucial to detect and monitor any existing defects or damage precursors to guarantee their long-term safety and reliability. To address this issue, there are various non-destructive evaluation (NDE) techniques that are widely employed to detect defects and damage in advanced structures, such as by using strain gages and optical sensors [33–

35], vision-based methods [36–38], thermography, radiographic testing [39–41], ultrasonic testing [42,43], and electrical tomographic methods [44,45].

1.2.1 Strain and Optical Sensing Techniques

In advanced structures, strain gages, and optical sensing techniques are commonly used for monitoring structural health and detecting damage. Foil-based strain gages are commonly used in advanced structures due to their high sensitivity and small size. These sensors work by using a metallic foil or wire attached to the structure's surface [35]. Strain gages can be used to detect damage in a structure by measuring the strain at specific locations. When damage occurs, the material around the damage site undergoes a change in its mechanical properties, resulting in a change in strain. Yeow et al. [35] and Griffith et al. [46] applied strain gages on the composite materials and applied an epoxy precoat to fill surface irregularities, which eliminates bond failure but results in a relatively thick bond line that exhibits high levels of adhesive creep at elevated temperatures. Other than applying on the surface of the inspected structures, advanced materials can also have strain gages embedded within them to monitor strain and detect damage. Embedding strain gages within the composite structure provide a more direct measurement of strain and deformation and offer more reliable data because of exemption from damage or detachment over time. For example, Kanerva et al. [47] implemented fully embedded electrical resistance strain gages in a hybrid material system of CFRP and tungsten accurately sense thermal expansion when appropriate correction functions are used.

Optical sensors are another type of sensor that uses light to measure strain and deformation. These sensors work by using a fiber optic cable that is embedded within the structure [34]. As the structure deforms, the cable experiences a change in its optical properties, which is measured using

a light source and a photodetector. Fiber optic sensors are highly sensitive, and they can detect changes in strain and deformation that are too small to be measured using traditional sensors. Optical sensors are ideal for monitoring large structures and complex geometries. In recent years, distributed optical fiber sensing techniques have been developed, allowing for the monitoring of strain and temperature changes along the entire length of a fiber optic cable. Glisic et al. [34] applied a distributed optical fiber sensing technique (a sensing cable) on a bridge for crack detection and structural integrity monitoring, but it could only monitor the one-dimensional strains along the sensors' installed locations.

While strain gages and optical sensors can provide accurate and stable measurements, they are limited in their ability to offer a comprehensive view of the structure being monitored. Discrete sensors can only provide localized monitoring in the installation area, and, in the case of optical sensors, they can only acquire strain along the one-dimensional length along the sensor's installed location. Therefore, in order to obtain a more comprehensive and spatially distributed view of the structure being monitored, other NDT methods are needed.

1.2.2 Vision-based Methods

One of the most common and easiest damage monitoring technique today is based on visual inspection, however, the process is labor-, cost- and time-consuming, and it could not offer timely spatial damage information. Automated vision-based inspection has been developed to address this issue. Vision-based techniques that utilize photographed images from high-speed cameras and imaging processing developed in computer vision are more labor-saving and accurate for detecting structural abnormalities [36,38]. This approach is becoming increasingly popular due to its ability to provide high spatial resolution and real-time monitoring capabilities. One advantage of using

vision-based methods is that they are non-contact, which means they can be used to inspect surfaces that are difficult to access or that may be damaged by other inspection methods. In addition, the use of high-speed cameras and advanced algorithms for image processing allows for the detection of small defects that may be missed by other inspection techniques. Recent advancements in vision-based methods using image processing and machine learning techniques have shown promising results in damage detection for various types of infrastructure, such as reinforced concrete bridges, precast tunnels, and underground concrete pipes. The use of transfer learning and deep convolutional neural networks has been investigated as an alternative to training original neural networks, and data augmentation techniques have been implemented to improve accuracy and robustness [36,38].

However, there are some limitations to the use of vision-based methods for damage monitoring. One of the main challenges is the need for good lighting conditions and the presence of contrast between the structure and its surroundings. Additionally, the presence of non-damage features in the image, such as joints, wires or boundaries, can make it difficult to distinguish between actual damage and these features. Also, the complexity of the background and the diverse surface textures can also impact the performance of vision-based techniques [48]. Finally, vision-based method inspection is typically limited to surface damage and cannot penetrate the material to detect internal cracks or other types of damage. As a result, additional NDE methods, such as ultrasonic testing or X-ray imaging, may be needed to fully assess the extent of damage in advanced structures.

1.2.3 Thermography

Thermography is another NDE technique that utilizes the measurement of surface temperature to detect anomalies in the material beneath the surface. This technique is based on the principle that variations in the material's internal structure cause variations in the heat flow through the surface. In thermography, a heat source is applied to the surface of the material, and the heat distribution is measured using an infrared camera [49,50]. The resulting image, called a thermogram, shows the temperature distribution on the surface of the material. Any anomalies in the internal structure of the material will cause variations in the heat flow, which will be visible in the thermogram.

Thermography is a widely used technique for the detection of defects such as cracks, delaminations, and voids in composite and lattice structures. It is a fast NDE method that can detect defects over a large area. However, thermography has some limitations. First, the technique is highly dependent on the material's thermal properties, and it may not be effective for materials with low thermal conductivity, such as some polymers. Besides, since the thermal energy may not be able to penetrate deep into the structure, it may not be able to detect subsurface damage embedded too deep within the material.

1.2.4 Radiographic Testing

Radiographic Testing (RT) is a non-destructive testing method that uses X-rays or gamma rays to examine the internal structure of a material or component [51]. The basic principle of RT is to pass high-energy radiation through the material or component and capture the resulting image on a photographic film or digital detector. The areas of the material that absorb more radiation appear darker on the image, while areas that absorb less radiation appear lighter. This creates a

contrast that can reveal hidden defects. RT can be performed in two ways: film radiography, which uses a photographic film to capture the image, and computed tomography (CT), which uses computer algorithms to create a three-dimensional image of the internal structure of the material or component. CT provides reliable and quickly readable data as it enables the observation of structures at a microscopic scale, thereby modifying the scale of observation from macroscopic to microscopic, leading to accurate results [39].

These radiography methods can detect large voids, inclusions, trans-laminar cracks, non-uniform fiber distribution, and fiber misorientation such as fiber wrinkles in composite materials. Penetrant-enhanced radiography is employed specifically to detect small matrix cracks and delaminations in a composite sample. Also, CT has been shown to be a promising technique for the inspection and characterization of AM parts. CT allows for 3D visualization and analysis of internal features including defects such as voids, cracks, and inclusions. It also provides quantitative information on geometric features, such as porosity and density, which are critical to ensure the functionality and mechanical properties of AM parts. CT has been used for the inspection of various AM processes, including selective laser melting (SLM), electron beam melting (EBM), and binder jetting (BJ).

While RT is a powerful tool for detecting internal flaws, it does have some limitations, including the potential for exposure to radiation, and the need for specialized equipment and trained operators. Besides, they can be inefficient for inspecting complex cellular lattice structures. For example, CT reconstruction of defects in lattice structure struts requires multiple projection slices and can be computationally intensive, slow, and expensive [51].

1.2.5 Ultrasonic Testing

UT utilizes high-frequency sound waves to detect and evaluate flaws or defects within the material being inspected. The technique can detect internal cracks, voids, and other inhomogeneities in composite materials, as well as changes in thickness, corrosion, and other structural anomalies in metals. UT works by emitting ultrasonic waves from a transducer, which are then reflected back to the transducer and analyzed to determine the presence, location, and size of any defects. UT can be performed in pulse-echo mode, where the transducer sends and receives the waves, or in through-transmission mode, where one transducer sends the waves and another receives them. UT has the advantage of being able to provide real-time results and can be performed on curved or irregularly shaped surfaces.

However, it requires skilled operators to interpret the data, and it can be affected by the presence of coatings or rough surfaces that can reflect or scatter the ultrasonic waves. Especially for lattice structures with complex geometries, UT requires a dense array of transducers and complicated wave generation and propagation patterns to evaluate the different scales and locations of defects [43].

1.3 Electrical Tomographic Methods

While NDE methods such as optical sensors, vision-based methods, and thermography can provide valuable insights into damage detection for advanced structures, they do have limitations to offer spatial damage maps or detect damage that is located deep within the structure. Other methods such as ultrasonic testing and radiographic testing are capable of detecting interior damage, but they require extensive setup time and complex installation processes, making them less practical for certain applications. Given these challenges, it may be more advantageous to

explore the inherent properties of CFRP composites for self-sensing, rather than relying on additional devices and labor for sensor installation.

Numerous studies have utilized the electrical properties of CFRP composites or lattice structures for self-sensing, including embedded electrical resistance strain gages and electrical tomographic techniques. Electrical tomography is a non-invasive imaging technique used to visualize and monitor the internal structure and properties of materials. It involves applying electrical fields to a material and measuring the resulting electrical responses. Three commonly used electrical tomography techniques are electrical resistance tomography (ERT), electrical impedance tomography (EIT), and electrical capacitance tomography (ECT).

1.3.1 Electrical Resistance and Impedance Tomography

ERT is a technique used to image the internal conductivity distribution of a material. ERT involves injecting a direct or a low-frequency electrical current through the material, typically in the range of 1 Hz to 1 kHz, and measuring the resulting voltages at the electrodes placed on the boundary of the material [52,53]. Because the electrical conductivity change will influence the boundary voltage measurements, the distribution of electrical conductivity can then be reconstructed using boundary measurements, providing images of the internal structure of the material. For advanced structures that have coupled electrical properties and mechanical properties, ERT could be employed to infer the presence of certain defect features, such as voids, cracks, or overstrains.

EIT is another technique used to image the internal structure of materials. EIT involves injecting a high-frequency electrical current through the material, typically in the range of 1 kHz to 10 MHz, which is injected into the material being imaged. This high-frequency current causes

the material to behave like a capacitor, resulting in impedance or the complex conductivity change that is measured at the boundary. Similarly, the boundary measurements could capture the interior complex conductivity distribution change that correlated to structural health maps and could offer reconstructions that could be effectively interpreted as spatial damage or overstrain maps.

The ERT and EIT methods have been extensively leveraged in geophysical and clinical applications since the 1980s and have recently gained attention for structural health monitoring (SHM) applications. This spatial sensing technique provides more sufficient information than discrete installed sensors by reconstructing interior electrical conductivity maps that correlated to mechanical properties maps [54]. Therefore, it could be effectively employed in damage and spatial strain sensing on electrically conductive composites and nanocomposite thin film coupled structures [55,56]. The utilization of a target's electromechanical properties exempts inspection from complex operations (i.e. multiple projections of CT) [52,57]. For instance, Loyola et al. [57] investigated the use of EIT for spatial scalar strain sensing with nanocomposite thin films, while Gupta et al. [52] used EIT for localizing damage features in smart concrete casted with conductive-film-coated aggregates.

Moreover, the ERT and EIT methods have been investigated for detecting damage in advanced structures by leveraging the structure's intrinsic electromechanical properties. Baltopoulos et al. [58] directly leveraged EIT for defect localization of nearly electrically isotropic CFRP laminate with electrodes attached to the boundary. Instead of introducing additional devices and extra labor for sensor installation, Nonn et al. [14] employed ERT with built-in connecting rivets and the inherent electrical properties of CFRP composites to localize a damaged hole in an anisotropic CFRP composite laminate. The damage localization capability of the EIT method on CFRP laminate benefits from its connected electrical and mechanical field coming from interior

carbon fibers. Reconstructed conductivity maps could be efficiently transferred to damage state maps because of the relation between electrical conductivity decrease and defects such as damages, fiber fracture, and delamination [59]. Shu et al. [60] applied 3D ERT on AM lattice structures with the normalized sensitivity map and reconstructed the damaged strut in the complex lattice structures.

However, ERT and EIT methods have limitations due to their reliance on scalar-based solvers, which may not be effective for anisotropic materials. Moreover, the boundary measurements may result in low central sensitivity, making it difficult to detect defects in certain areas. To overcome these limitations, specific modifications have been incorporated, such as the use of electrical property tensors and normalized sensitivity maps. These modifications can improve the use of ERT for anisotropic CFRP composites and lattice structures with complex geometries. Additionally, the use of smart paint and frequency difference EIT have been explored to improve detection in painted structures without baseline measurements. These modifications will be stated in detail in the following sections. By addressing these limitations, electrical tomography methods have the potential to become increasingly valuable NDE tools for advanced structures.

1.3.2 Noncontact Electrical Capacitance Tomography

ECT is a noncontact technique used to image the internal electrical permittivity and conductivity distribution of a target. In ECT, an electric field is propagated by applying an alternating current to an electrode, and this electric field then interacts with the material being studied. The interaction between the electric field and the material results in changes to the electrical capacitance between pairs of electrodes, which are then used to reconstruct the electrical

permittivity distribution of the material [61]. One of the significant advantages of ECT is its non-contact feature. It can measure the properties of the material being studied without using contact probes or inserting sensors into the material.

ECT has been successfully applied in various industrial process monitoring applications since its discovery in the late 1980s. It has also been used for nondestructive inspection of structural components and monitoring of epoxy curing and subsurface defects in composites. For example, Gupta et al. used ECT coupled with passive thin-film sensors to achieve non-contact pH and strain sensing. While damage in CFRP panels is consistently associated with decreased electrical permittivity and conductivity, the damage distribution would be interpreted from reconstructing electrical properties [22]. The classical ECT operates by measuring the changes in capacitance between multiple electrode pairs surrounding the object of interest, and the sensing domain is usually defined as the circular area enclosed by the boundary electrodes [62]. Circular ECT offers impressive sensitivity in the sensing domain, however, its primary limitation is the constraint on the shape of the objects that can be inserted within the circular electrode array.

As an advanced variant, planar ECT focuses on a two-dimensional electrode arrangement, which expands the applicability of ECT to structures with different dimensions and shapes [22,63]. The advent of planar ECT has also unlocked its potential for detecting damage in large-scale complex structures, such as ships and aircraft. Inspectors can employ the designed planar ECT electrode array to efficiently scan these structures, enabling rapid and accurate assessments of their internal properties. This non-invasive approach to damage detection ensures the early identification of potential issues, thereby enhancing overall safety and operational efficiency. Gupta et al. [22] demonstrated that planar ECT could detect and visualize the presence and location of delamination damage of different sizes in CFRP composites. Fan et al. [63] optimized the

sensitivity matrix of the Planar ECT sensor by rotating the electrodes and investigated the reconstructed image quality of different Planar ECT arrays for detecting damage locations in CFRP composite.

To apply planar ECT arrays as an effective scanning NDE system, the processing time must be minimized. Classical model-based ECT methods can be time-consuming due to the complex inverse problem process, including the iterative solver and the calculation of the Jacobian matrix [62]. Therefore, it is important to identify and implement techniques that can accelerate the ECT process and reduce processing time.

1.4 Machine Learning Methods

Machine learning is a rapidly developing field of computer science that allows machines to learn from data and make predictions or decisions without being explicitly programmed [64]. This is done using established algorithms and training data to build models that can be used to process and analyze large amounts of data in a timely manner. Machine learning algorithms can quickly and accurately process large and complex data sets, which would be impossible for humans to analyze in a reasonable amount of time. In general, there are two main categories of machine learning: supervised learning and unsupervised learning. Supervised learning involves the use of labeled data for training, while unsupervised learning involves the discovery of hidden patterns or anomalies in data without any prior knowledge.

First, supervised learning involves training an algorithm using labeled data with known outcomes, with the goal of predicting outcomes for new and unseen data. This can be used for tasks such as classification, where the algorithm must assign a label to a given input, or regression,

where the algorithm must predict a continuous value. Common methods of supervised learning include decision trees, logistic regression, support vector machines, and neural networks.

Second, unsupervised learning is used when the data set is not labeled and the goal is to identify patterns or groupings in the data. This can be used for tasks such as clustering, where the algorithm groups data points that are similar to each other, or anomaly detection, where the algorithm identifies unusual or abnormal data points. Common methods of unsupervised learning include k-means clustering, principal component analysis, and autoencoders.

1.4.1 Machine Learning on Tomographic Methods

In recent years, the data-driven artificial neural network (ANN) method has emerged as a powerful tool for addressing complex and nonlinear problems. ANN are composed of interconnected neurons organized in layers, designed to learn and process complex data patterns. These neurons are linked through weighted connections, which are adjusted during training to improve the network's performance [65].The layered structure of ANN enhances their ability to capture nonlinearity, making them well-suited for solving nonlinear problems such as electrical tomographic problems. For example, Quqa et al. [66] employed ANN to solve the EIT problem and validate the better performance of deep ANN versus the traditional total variation method. Zheng et al. [21] and Garbaa et al. [22] used autoencoder neural networks to solve the ECT image reconstruction problem and apply it to estimate flow patterns inside a circular electrode array. The reconstructions exhibit better image quality with more time efficiency than the classical linear back projection (LBP) method results. As an alternative, machine learning techniques can be employed to accelerate the process.

1.5 Thesis Outline

Continuing from the introduction, the subsequent chapters of this dissertation delve into the specific aspects of electrical tomographic methods and their application in damage detection for advanced structures. Chapter 2 provides a comprehensive exploration of electrical tomographic methods, discussing the forward problems and inverse problem of ERT, EIT, and ECT, as well as the application of artificial neural networks in the tomographic method. This chapter serves as the foundation for the subsequent chapters, which focus on the practical implementation and evaluation of these methods in various contexts.

In Chapter 3, the application of 2D ERT in detecting damage in anisotropic CFRP composites was discussed. The anisotropic solver employed, simulation details, and experimental results are thoroughly described to highlight the capabilities of this approach.

Chapter 4 focuses on the detection of multiple defects in additively manufactured lattice structures using 3D ERT. The chapter presents adjusted absolute imaging and normalized sensitivity map to improve the low central sensitivity. Simulation results are provided, illustrating the ability of 3D ERT on single and multiple defects detection. Experimental details, testing, and results are also discussed, validating the effectiveness of 3D ERT in detecting defects in lattice structures.

Chapter 5 delves into the utilization of EIT along with frequency-dependent nanocomposite smart paint. The integration of EIT offers a promising approach for reconstructing damage and strain states without the need for baseline measurements. Both simulations and experiments were conducted to validate the effectiveness of this method. These validation efforts demonstrate the

potential of EIT and frequency-dependent nanocomposite smart paint in accurately detecting and characterizing damage and strain states.

Chapter 6 centers on the application of planar noncontact capacitive imaging and deep learning techniques for the detection of damage in composite materials. The chapter outlines the utilization of a complex impedance model in the planar ECT method, along with the implementation of reduced measurements and deep ANN. To validate the effectiveness of the proposed method, a series of experiments were conducted, including the use of modularized conductive PLA, detection of impact damage, and identification of delamination in CFRP composites.

Each chapter follows a structured approach, providing an introduction to the topic, describing the methods and techniques used, presenting simulation or experimental details, and discussing the results and conclusions derived from the research.

CHAPTER 2 ELECTRICAL TOMOGRAPHIC METHODS

2.1 Introduction

In this chapter, the mathematical background and numerical techniques used for ERT, EIT, and ECT will be introduced. The electrical properties distribution, such as electrical conductivity and permittivity would be reconstructed from the solvers. Because of the correlation between the damaged/strained states and the electrical properties of the inspected objects or surfaces, once the electrical properties distribution is reconstructed, the regions of the object that have undergone changes in their electrical properties due to damage or strain could be identified.

In the first part of this chapter, the classical solvers based on the finite element method (FEM) are stated. These tomographic methods consist of forward and inverse problems. In the forward problem solver, the boundary voltages or capacitances can be calculated based on a known electrical properties distribution and the excitation schemes [52]. The Laplace equations governing the physical model of these tomographic methods are stated, along with detailed descriptions of the forward problem.

In practice, practical implementations of the tomographic methods require solving the inverse problem, which reconstructs electrical properties distribution from a set of experimental boundary potential or capacitance measurements [52]. There are two types of imaging methods for the inverse problem, absolute imaging and difference imaging methods. Absolute imaging involves directly computing the electrical properties distribution within the object based on the measurements. This method assumes that the electrical properties of the object are homogeneous, and the reconstruction is performed without any reference to a baseline or background image. The aim of this method is to obtain a quantitative estimate of the interior distribution, but its

effectiveness will be easily affected by errors generated from measurement, inaccurate model assumptions, and spatial inhomogeneity [67]. Difference imaging, on the other hand, utilizes the difference between two measurements to reconstruct the distribution difference of the two states. Time-difference and frequency-difference imaging are both valid methods for the difference imaging process. Since the difference imaging is reconstructing the changes in electrical properties by subtracting the measured data of a reference state, such as an undamaged state or a damaged stated in another excitation frequency, it could effectively compensate for drift or noise in the measurements and extract useful damage information from the background images.

In addition to the classical solvers, data-driven approaches using deep ANN for reconstructions are also introduced. The model-based method for solving the inverse problem of reconstructing the electrical conductivity distribution within an object can be time-consuming and computationally intensive. This is especially true for the iterative reconstruction methods, where the nodal potentials of each finite element in each excitation scheme must be calculated to generate the Jacobian matrix for each iteration, which can be computationally intensive. In contrast, data-driven methods such as deep ANN can avoid the computationally intensive calculation of the Jacobian matrix while still capturing the nonlinearity of the reconstruction process. Here, the deep ANN systems were trained by multiple damaged cases and learned the mapping between the measurements and the internal electrical properties distributions, allowing for fast and accurate reconstruction of images.

2.2 Forward Problems

2.2.1 ERT Forward Problem

ERT is a nonintrusive soft-field imaging method that relies on boundary current injections and voltage measurements for reconstructing the conductivity distribution of a conductive body (or target) [54,56]. It is known that localized damage (e.g., voids, cracks, or broken parts) in the target can prevent or limit electric current propagation through that specific region. Therefore, identifying the magnitudes and locations of localized conductivity changes in reconstructions would enable direct visualization of damage severity and their respective locations.

In the forward problem, electric current propagation within a conductive target, Ω, with no interior current source, is governed by Laplace's equation [52,54,68]:

$$\nabla \cdot (\sigma \nabla \phi) = 0 \text{ in } \Omega \tag{2.1}$$

where σ is the conductivity distribution of Ω, and ϕ is the electric potential in the domain. The Dirichlet and Neumann boundary conditions and the complete electrode model are also defined in Equations (2.2) to (2.4), respectively [52,54]:

$$\int_{e_l} \sigma \frac{\partial \phi}{\partial n} dS = I_l \text{ on } \Gamma_1 \tag{2.2}$$

$$\sigma \frac{\partial \phi}{\partial n} = 0 \text{ on } \Gamma_2 \tag{2.3}$$

$$\phi + z_l \sigma \frac{\partial \phi}{\partial n} = V_l \text{ on } \Gamma_1 \tag{2.4}$$

where e_l is the location of the l^{th} electrode, n is the normal direction from the boundary, z_l is the contact impedance at the l^{th} electrode, and I_l and V_l are the injected current and electric potential

on the lth electrode, respectively. Here, Γ_1 is the boundary with electrodes, while Γ_2 refers to the remainder of the boundary. Equations (2.1) to (2.4) are numerically solved by the finite element (FE) method with a known σ distribution for simulated voltage responses V(σ) [52,54].

The second partial differential equation is usually numerically solved by FE method with a Galerkin approximation,

$$\phi^h = \sum_{i=1}^{m} \phi_i N_i \tag{2.5}$$

Here, ϕ^h is the approximated electric potential distribution, ϕ_i and N_i are the nodal potential and shape function of the i^{th} node. The Galerkin approximation transforms the continuous formulation to discrete in meshed finite element domain and constructs a set of linear equations (2.6) and (2.7) for computing nodal electrical potentials ϕ_i and electrodes electric potentials V_l which are responsible for boundary voltages calculation [52,54]. Currents could be applied between an adjacent, diagonal, or opposite pair of electrodes according to different current injection patterns, and measured boundary voltage in experiments would be compared with the calculated voltages in the forward problem for further reconstructions [11,15].

$$\sum_{i=1}^{m} \phi_i \left[\sum_{j=1}^{m} \left(\iint_{\Omega} \sigma \nabla N_i \cdot \nabla N_j dx^2 + \sum_{l=1}^{L} \frac{1}{z_l} \int_{e_l} N_i N_j dx \right) \right] - \sum_{l=1}^{L} V_l \left(\sum_{j=1}^{m} \frac{1}{z_l} \int_{e_l} N_j dx \right) = 0 \tag{2.6}$$

$$- \sum_{i=1}^{m} \phi_i \left(\sum_{l=1}^{L} \frac{1}{z_l} \int_{e_l} N_i dx \right) + \sum_{l=1}^{L} \frac{1}{z_l} V_l |e_l| = \sum_{l=1}^{L} I_l \tag{2.7}$$

2.2.2 EIT Forward Problem

EIT is also a non-invasive electrical imaging method that can be used to visualize the interior complex conductivity distribution of a conductive body using only current injections and corresponding voltage measurements at boundary electrodes [54,69]. EIT involves injecting

alternating currents into the object and measuring the resulting voltage changes on the boundary. Since the current flow in the target is depending on the distribution of the internal complex conductivity, the boundary voltage measurements of the target could reflect the change in the interior complex conductivity distribution [67]. In the EIT forward problem, boundary voltages are estimates based on a known complex conductivity distribution [52]. When a direct current is applied at the boundary to interrogate a conductive domain Ω (which has a known complex conductivity distribution), the corresponding boundary electric potentials can be evaluated using the updated Laplace's equation with γ_ω, which is the complex conductivity distribution of Ω in the injecting frequency ω, [52,60,70]:

$$\nabla \cdot (\gamma_\omega \nabla \phi) = 0 \text{ in } \Omega \tag{2.8}$$

The Dirichlet and Neumann boundary conditions, as well as the complete electrode model, are also updated with the complex conductivity γ_ω:

$$\int_{e_l} \gamma_\omega \frac{\partial \phi}{\partial n} dS = I_l \text{ on } \Gamma_1 \tag{2.9}$$

$$\gamma_\omega \frac{\partial \phi}{\partial n} = 0 \text{ on } \Gamma_2 \tag{2.10}$$

$$\phi + z_l \gamma_\omega \frac{\partial \phi}{\partial n} = V_l \text{ on } \Gamma_1 \tag{2.11}$$

When a current is injected in a specific pair of electrodes, the electric potentials of the boundary electrodes could be solved with Equations (2.8) – (2.11) similarly using FE method as in ERT forward problem. The complete set of boundary voltages (V_ω^i) (i.e., for Ω with an assumed complex conductivity distribution (γ_ω^i) corresponding to an i^{th} condition) is obtained by injecting current with frequency ω across different unique pairs of boundary electrodes. The adjacent,

opposite, or diagonal current injection pattern can all be used to interrogate Ω. The forward problem can be used to solve for boundary voltages, $V_{\omega a}{}^{i}$ and $V_{\omega b}{}^{i}$, which correspond to i^{th} damaged state with different current injecting frequencies ω_a and ω_b. Because the complex conductivity in the damage region is always 0 S/m while the complex conductivity may change with excitation frequency, the different distribution $\gamma_{\omega a}{}^{i}$ and $\gamma_{\omega b}{}^{i}$ are measured when currents with different frequencies are injected respectively. The change in conductivity distribution between those two states ($\delta\gamma$) can also be used to solve for the corresponding boundary voltage difference, δV [52,54]. This method will be efficiently applied to frequency-difference EIT (fdEIT).

2.2.3 ECT Forward Problem

In ECT, an object is surrounded by a set of electrodes, and a voltage excitation is applied to the electrode. The resulting electric field induces a distribution of charges within the object, which can be measured by the capacitance between pairs of electrodes. This noncontact measurement technique allows for the assessment of the object's internal electrical properties without the need for physical contact, making it particularly suitable for noninvasive and nondestructive evaluation of various structures. When a non-conductive object is inside the electrode array, the governing equation will be:

$$\nabla \cdot (\varepsilon \nabla \phi) = 0 \text{ in } \Omega \tag{2.12}$$

while the ε is the electrical permittivity of the material. The Dirichlet and Neumann boundary conditions are stated below:

$$\phi = V_l \text{ on } \Gamma_1 \tag{2.13}$$

$$\varepsilon \frac{\partial \phi}{\partial n} = 0 \text{ on } \Gamma_2 \tag{2.14}$$

The voltage is excited on the boundary electrodes in sequence, and the potential of excited boundary electrodes will be equal to the magnitude of the excitation voltage, and the electrical potentials of other electrodes are zeros because they are grounded. The equations could also be solved with the FE method and the nodal electric potentials of each finite element could be computed.

After obtaining the nodal electric potentials, the corresponding capacitances between electrodes could be calculated using the finite difference method, respectively.

$$C_{lm} = \frac{1}{V}\int_{e_l} \varepsilon \frac{\partial \phi_l}{\partial n} dS \tag{2.15}$$

Where e_l is the excitation electrodes and ϕ_l is calculated nodal electric potentials when e_l is excited. Here, m is selected from all other electrodes that are grounded.

2.3 Inverse Problem

The inverse problems of tomographic methods involve calculating the electrical properties distribution within the object or material based on the measured voltage data obtained from the boundary electrodes. The inverse problem is a complex task, as there exists an infinite number of possible distributions that could result in the same measured data. This issue poses a challenge for ERT image reconstruction, as the reconstruction of the true internal electrical resistivity distribution requires the identification of the most probable solution among the infinite possibilities. In response to this challenge, various inversion algorithms have been developed, which include linear and nonlinear methods, regularization techniques, and data-driven approaches. These methods aim to minimize the difference between the measured data and the predicted data from

the model, by incorporating additional regularization methods that reduce the number of possible solutions [44,69].

The one-step linearization and iterative nonlinear algorithms are used to minimize the difference between the measured and predicted data. The regularization techniques aim to reduce the number of possible solutions by incorporating additional information or constraints, such as smoothness or sparsity of the electrical properties distribution [69,71]. These techniques offer a range of solutions for the inverse problem in ERT, EIT, and ECT, and the choice of method depends on the specific application and the desired accuracy of the reconstruction.

2.3.1 Absolute Imaging

Absolute imaging is a method that directly reconstructs absolute electrical properties distribution using the measured voltage or capacitance data. Here, the inverse problem aims to reconstruct the interior electrical properties of Ω by minimizing the difference between experimentally measured boundary voltages (V_m) and simulated voltages $V(\sigma)$ or $V(\gamma_\omega)$, or between measured capacitances (C_m) and simulated capacitances $C(\varepsilon)$, starting with an assumed distribution. Because absolute imaging assumes that the electrical properties of the object are homogeneous, it is useful in applications where the electrical properties of the object are relatively uniform. Moreover, since the reconstruction process is performed without any reference to a baseline or background image, it is easily influenced by environmental noise and model inaccuracies [67]. But absolute imaging has the advantage to offer a quantitative estimate of the electrical properties distribution. Quantitative absolute imaging is useful in application of structural damage detection because it allows for the characterization of the electrical properties, which can provide valuable insight into the structural health of the material. For example, changes in conductivity may indicate

the presence of microcracks or other forms of damage that are not visible to the naked eye. By quantitatively characterizing the conductivity distribution within the material, EIT can help to identify the severities of defects, and prevent them lead to catastrophic failure [60,67].

2.3.1.1 Objective Functions and Regularization Methods

In ERT, EIT, and ECT processes, to reconstruct the distribution of electrical properties, the objective functions to minimize the differences between measurements and calculated data in the forward problems are stated in Equation (2.16) – (2.18) respectively:

$$g_{\sigma} = \arg\min_{\sigma}\{\|V_m - V(\sigma)\|^2\} \tag{2.16}$$

$$g_{\gamma_\omega} = \arg\min_{\gamma_\omega}\{\|V_m - V(\gamma_\omega)\|^2\} \tag{2.17}$$

$$g_{\varepsilon} = \arg\min_{\varepsilon}\{\|C_m - C(\varepsilon)\|^2\} \tag{2.18}$$

However, tomographic methods are of ill-posed nature, which means that there are an infinite number of possible solutions that can fit the measured data equally well. This is because electrical property distributions within bodies or materials cannot be directly measured, while only boundary measurement can be assessed. Therefore, reconstructed internal electrical property distributions from these measurements are inherently uncertain and highly vulnerable to noise and errors during measurement.

Regularization is a mathematical technique designed to eliminate this uncertainty in the reconstruction process by adding extra constraints. By taking into account prior knowledge about the physical characteristics of material, regularization methods can improve image quality, reduce noise levels, and mitigate measurement errors [54,72]. Reconstructions without regularizations can

be highly susceptible to noise and other sources of error, leading to poor image quality and reduced diagnostic precision. Regularization methods enable us to control the tradeoff between fitting data and producing a smooth or structured solution, producing more precise and dependable images.

There are a few regularization methods that are commonly utilized in tomographic imaging methods. One popular regularization technique is Tikhonov regularization, which involves adding a penalty term to the objective function used to solve an inverse problem. This penalty term is proportional to the square root of the L2 norm of the solution vector and helps to solve for smooth solutions. Hence the objective function becomes:

$$g_\sigma = \arg\min_\sigma \{\|V_m - V(\sigma)\|^2 + \lambda\|R\sigma\|^2\} \tag{2.19}$$

$$g_{\gamma_\omega} = \arg\min_{\gamma_\omega} \{\|V_m - V(\gamma_\omega)\|^2 + \lambda\|R\gamma_\omega\|^2\} \tag{2.20}$$

$$g_\varepsilon = \arg\min_\varepsilon \{\|C_m - C(\varepsilon)\|^2 + \lambda\|R\varepsilon\|^2\} \tag{2.21}$$

Where λ is the hyperparameter, and R is a regularization matrix, which is the square root of the diagonal of the matrix Hessian matrix [62]. Tikhonov regularization can reduce noise in images while producing more reliable ones by damping out the small singular values from the system, but it may result in blurring or loss of details in reconstructions [69].

Total variation (TV) regularization is another popular technique to promote sparsity or piecewise constant solutions [71]. This involves adding a penalty term proportional to the total variation of the solution, encouraging smooth transitions or edges. TV regularization helps preserve details in the reconstruction and also maintains the contrast. However, it may introduce artifacts in regions with high curvature. The objective functions added with TV regularization are:

$$g_\sigma = \arg\min_{\sigma}\{\|V_m - V(\sigma)\|^2 + \lambda TV(\sigma)\} \tag{2.22}$$

$$g_{\gamma_\omega} = \arg\min_{\gamma_\omega}\{\|V_m - V(\gamma_\omega)\|^2 + \lambda TV(\gamma_\omega)\} \tag{2.23}$$

$$g_\varepsilon = \arg\min_{\varepsilon}\{\|C_m - C(\varepsilon)\|^2 + \lambda TV(\varepsilon)\} \tag{2.24}$$

The total variation of electrical properties distribution *TV*(*) could be written as:

$$TV(*) = |L*| \int_\Omega \nabla\delta\boldsymbol{\sigma}\ \mathrm{d}\Omega \tag{2.25}$$

Where *L* is a sparse matrix that represents the edge information of the mesh used in reconstructions. Specifically, each row of matrix *L* represents one edge in the mesh, and each row contains two non-zero values of the edge length that correspond to the two elements connected by the edge. Here, l_k is the length of the k^{th} edge in the mesh, and the k^{th} row of the matrix *L* is defined as:

$$L_k = [0,\ldots,l_k,0,\ldots,-l_k,0,\ldots,0] \tag{2.26}$$

2.3.1.2 Jacobian Matrix

To solve the inverse problem in tomographic methods, The calculation of Jacobian matrix, or say the sensitivity matrix, is needed. The Jacobian matrix is used to calculate the gradient of the objective function, which represents the direction of the steepest descent in the search for the optimal solution. It could be further used in further one-step linearization algorithm as *J*, or in the nonlinear iterative algorithm as J^i:

$$J^i = -\int_\Omega (\nabla\phi_p^i)^T \nabla\phi_q^i dx^3 \tag{2.27}$$

For ERT and EIT, the entries of the Jacobian matrix are the derivatives of $V(\sigma)$ or $V(\gamma_\omega)$ with respect to the σ or γ_ω in each finite element. Each row of the Jacobian matrix corresponds to a single measurement of the vector $V(\sigma)$ or $V(\gamma_\omega)$, and the corresponding ϕ^p and ϕ^q are the nodal electric potentials considering current passing through the pair of current injection electrodes p and current passing through the measuring electrodes q, respectively [62,69,71,73]. For ECT, ϕ^p and ϕ^q are the nodal electric potentials considering the two electrodes for the capacitance measurements are excited respectively [73]. The sensitivity matrix effectively interprets the influence of interior electrical properties in each element on every single measurement. Each element of the sensitivity matrix represents the sensitivity of a single measurement to changes in the distribution of internal electrical properties. By multiplying the sensitivity matrix with the vector of known electrical properties, data that would be measured at the boundary electrodes for a given electrical properties distribution could be predicted. Inversely, the interior electrical properties distribution could be calculated from known measurements using a sensitivity matrix.

2.3.1.3 One-step Linearization and Nonlinear Iterative Algorithms

One-step linearization is a computationally efficient approach for solving the inverse problem for tomographic methods. The linearization method involves approximating the sensitivity matrix, which describes the relationship between the internal electrical properties distributions and the measured voltage data, using a first-order Taylor series expansion. This approximation assumes that small changes in the internal conductivity distribution result in small changes in the measured voltage data, which can be represented by a linear relationship between the two [74]. The linear relationship is expressed with the sensitivity matrix J^i calculated at the current estimate of electrical properties distribution, and J^i stays the same during the reconstruction process. In this thesis, only the Tikhonov regularization method was utilized for the inverse

problem. Therefore, further discussions only focus on the inverse problem process with Tikhonov regularization. By solving the objective functions, the increment could be calculated for ERT, EIT, and ECT as follows, respectively:

$$\Delta\sigma = ({J^i}^T J^i + \lambda R^T R)^{-1} \cdot {J^i}^T \cdot [V_m - V(\sigma^i)] \tag{2.28}$$

$$\Delta\gamma_\omega = ({J^i}^T J^i + \lambda R^T R)^{-1} \cdot {J^i}^T \cdot [V_m - V({\gamma_\omega}^i)] \tag{2.29}$$

$$\Delta\varepsilon = ({J^i}^T J^i + \lambda R^T R)^{-1} \cdot {J^i}^T \cdot [C_m - C(\varepsilon^i)] \tag{2.30}$$

While the linearization method simplifies the relationship between the internal distribution and the measured voltage data, it also introduces errors due to the nonlinear nature of the problem. These errors can be reduced by using higher-order Taylor series expansions, or by using nonlinear iterative algorithms that do not require the linearization of the forward problem. The Gauss-Newton iterative algorithm [54,69] is an effective way to maintain the nonlinearity of the problem. The algorithm uses a linear approximation of the forward problem to update the estimate of the internal distribution in each iteration. Instead of using the same sensitivity matrix, the algorithm calculates the sensitivity matrix J^i based on the current estimate of internal distribution using Equation (2.27), and the increment in each iteration could be calculated using Equation (2.28) - (2.30). The estimation of internal distribution for ERT, EIT, and ECT could be continuously updated:

$$\sigma^{i+1} = \sigma^i + \Delta\sigma^{i+1} \tag{2.31}$$

$${\gamma_\omega}^{i+1} = {\gamma_\omega}^i + \Delta{\gamma_\omega}^{i+1} \tag{2.32}$$

$$\varepsilon^{i+1} = \varepsilon^i + \Delta\varepsilon^{i+1} \tag{2.33}$$

The sensitivity matrix J^{i+1} calculated based on the distribution in the *i+1* step will be used to compute the increment in the following step. The reconstruction process continues until the error ratio, which is defined as the norm of the difference between the measurements and the calculated data from the forward problem, is not improving by 0.1% for the following iterations, then returns the final reconstructed distribution [52].

The main advantage of the Gauss-Newton algorithm is its ability to handle nonlinear problems and produce high-quality reconstructions with good spatial resolution and contrast. However, the algorithm can be computationally expensive due to the iterative calculation of the sensitivity matrix and the regularization term.

2.3.2 Difference Imaging

Difference imaging is an imaging technique used in tomographic methods to improve the spatial resolution and contrast of reconstructed images. Other than absolute imaging, this technique involves subtracting two sets of measurements obtained under different conditions to isolate the changes in the internal conductivity distribution. The two sets of measurements correspond to two different electrical property distributions, which may be obtained at different time points where the electrical properties change, or at different frequencies where the electrical properties have different values. By subtracting the two sets of measurements, the resulting difference data contain information about the changes in the conductivity distribution between the two conditions. Hence the objective functions of the difference imaging for ERT, EIT, and ECT are:

$$g_{\delta\sigma} = \arg\min_{\delta\sigma}\{\|\delta V - J\delta\sigma\|^2 + \lambda\|R\delta\sigma\|^2\} \tag{2.34}$$

$$g_{\delta\gamma_\omega} = \arg\min_{\delta\gamma_\omega}\{\|\delta V - J\delta\gamma_\omega)\|^2 + \lambda\|R\delta\gamma_\omega\|^2\} \tag{2.35}$$

$$g_{\delta\varepsilon} = \arg\min_{\delta\varepsilon}\{\|\delta C - J\delta\varepsilon)\|^2 + \lambda\|R\delta\varepsilon\|^2\} \quad (2.36)$$

By solving the objective functions with one-step linearization or Gauss-Newton iterative algorithms as similar as in absolute imaging, the difference between the two distributions from the specific conditions, $\delta\sigma$, $\delta\gamma_\omega$, and $\delta\varepsilon$, could be obtained and used for further damage characterizations.

Unlike the absolute imaging technique, difference imaging does not provide quantitative values that directly represent electrical properties distribution. However, it is possible to obtain quantitative information about severities from difference images by calibrating the data against a reference or using a priori information about the internal distribution. Moreover, difference imaging has several advantages over absolute imaging, including improved spatial resolution and contrast in the reconstructed images. This is because the use of difference data instead of the original data in the reconstruction process can help to isolate the changes in the internal conductivity distribution and improve the quality of the reconstructed images. It could be effectively used to detect and localize abnormalities in the internal distribution, while the resulting difference data can highlight areas where there are significant changes. In addition, difference imaging can also help to mitigate the effects of modeling errors and measurement noise. Since the difference data isolate the changes in the internal distribution, any modeling errors or noise that affect both sets of measurements equally will be canceled out in the difference data. This can lead to more accurate and robust reconstructions, particularly in situations where the noise or modeling errors are significant.

2.3.2.1 Time-difference Technique

Time-difference imaging involves subtracting two sets of measurements obtained at different time points, typically corresponding to the same object in different physical states. By subtracting the two sets of measurements, the resulting difference data can highlight changes in the internal electrical properties distribution over time caused by the stress or loading event [75,76]. The method is particularly useful in the detection and characterization of cracks, which are known to cause changes in the electrical properties of the material surrounding the cracks [44]. The resulting difference image can then be used to locate the position and extent of the defects in the structure. Overall, time-difference imaging is a valuable tool for detecting and localizing changes in the internal electrical properties distribution of structures and can provide important information for assessing the health and safety of a system.

2.3.2.2 Frequency-difference Technique

Frequency-difference technique, unlike the time-difference technique that could be easily applied to all three tomographic methods, is usually adopted in the EIT process. In frequency-difference imaging, two sets of measurements are obtained at different frequencies, typically using a range of excitation frequencies or harmonic frequencies. This imaging technique is primarily effective for materials that exhibit a frequency-dependent response, such as some composite materials or frequency-dependent conductive nanomaterials. In these materials, changing excitation frequencies can result in variations in the electrical properties distribution of the material as a function of frequency.

To fulfill the frequency-difference technique, first, the complete set of boundary voltages (V_ω^i) (i.e., for Ω with an assumed complex conductivity distribution (γ_ω^i) corresponding to an i^{th}

condition) is obtained by injecting current with frequency ω across different unique pairs of boundary electrodes in the forward problem process. The adjacent, opposite, or diagonal current injection pattern can all be used to interrogate Ω, but only the adjacent current injection pattern was utilized in this thesis. It should be mentioned that the fdEIT forward problem can be used to solve for boundary voltages, $V_{\omega a}{}^{i}$ and $V_{\omega b}{}^{i}$, which correspond to an i^{th} damaged state with different current injecting frequencies ω_a and ω_b. Because the complex conductivity in damage region is always 0 S/m while the frequency-dependent conductive surrounding is changing with excitation frequency, the different distribution $\gamma_{\omega a}{}^{i}$ and $\gamma_{\omega b}{}^{i}$ are measured when currents with different frequencies are injected respectively. The change in conductivity distribution between those two states ($\delta\gamma$) can also be used to solve for the corresponding boundary voltage difference, δV [27,28].

During the inverse process, measurements are obtained under two excitation frequencies. By subtracting the two sets of measurements, the resulting difference data could be used to reconstruct the difference images for highlighting changes in the internal electrical properties distribution as a function of frequency. The damaged state could be extracted from it as the electrical properties in the crack or damaged regions would stay the same even when interrogated using different frequencies of excitation signals.

2.4 Deep Artificial Neural Network

The classical EIT method for solving the inverse problem is usually time consuming and computationally intensive. Especially, in the model-based tomographic method, the nodal potentials of each finite element in each excitation scheme are required to calculate the Jacobian matrix *J*, which is computationally intensive [31]. Moreover, the chosen of one-step linearization algorithm could not capture the nonlinearity of the tomographic problems and the employment of

the regularization method may also not successfully reconstruct the topological images because of the difficulty to select an optimal hyperparameter [24,29].

In contrast, data-driven methods, such as the deep ANN method, can avoid the computationally intensive calculation of the Jacobian matrix while preserving the nonlinearity of the reconstruction process as compared to a model-based tomographic approach with one-step linearization [25]. An ANN or a deep ANN framework, consisting of multiple layers connected with edges and nonlinear activation functions in neurons, can adapt to the nonlinear electrical tomographic problem and improve reconstructed images with higher accuracy [25,26]. During training, the weights for the neurons and edges would be updated to conform to the data. This approach has shown promise in improving the accuracy and speed of tomographic image reconstruction, making it a potentially valuable tool for NDT on advanced structures.

2.4.1 ANN Architecture

The basic structure of an ANN consists of three types of layers: an input layer, one or more hidden layers, and an output layer. In the case of a deep ANN, there are multiple hidden layers between the input and output layers, allowing for a more complex and hierarchical representation of data. The input layer receives the data and passes it to the hidden layers for processing. The

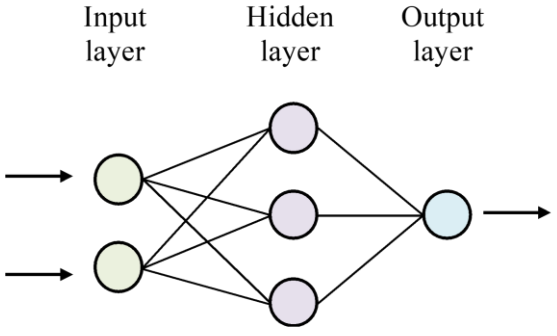

Figure 2.1: A simple ANN is illustrated.

hidden layers are responsible for extracting meaningful features from the input data, and the output layer produces the final prediction based on the learned features. Each layer of an ANN consists of multiple nodes or neurons that are interconnected. Each neuron receives input from the neurons in the previous layer and produces an output that is passed to the neurons in the next layer. The connections between neurons are weighted, and the weights are learned during the training process to optimize the performance of the network.

To introduce nonlinearity into the model, activation functions are applied in the network. The activation function is applied to each neuron in the hidden layers of the network. It takes the weighted sum of the inputs and bias of a neuron and applies a nonlinear transformation to produce an output value, which is then passed to the next layer or the output of the network. The activation function introduces nonlinearity into the network, which is essential for modeling complex, nonlinear relationships between inputs and outputs [66]. Without an activation function, a neural network would simply be a linear regression model. The choice of activation function depends on the problem being solved and the characteristics of the data. For example, sigmoid and tanh functions are often used in deep ANN because they are smooth and differentiable, which allows for efficient gradient-based optimization during training. On the other hand, ReLU (Rectified Linear Unit) is often used in the output layer because it is simple and computationally efficient. Here in this thesis, ELU (Exponential Linear Unit) is utilized for the tomographic problems because computational efficiency and its ability to maintain negative values.

The deep ANN architectures used in this thesis consist of an input layer, four hidden layers, and an output layer. The input layer for each tomographic method corresponds to a whole set of measurements, while the output layer corresponds to the conductivity, complex conductivity, or electrical permittivity values of finite element in the region of interest, or localized damage

coordinates. After the input layer, batch normalization was performed, followed by the fully connected hidden layers that implement an exponential linear unit activation function. At the end of the network, one last fully connected layer operated as the output layer for regression, without any activation function.

The forward propagation of the deep ANN in the hidden layers can be expressed as:

$$x_l = elu(W_l x_{l-1} + b_l) \tag{2.37}$$

where x_l and b_l are the output and the bias vectors of the l^{th} layer, respectively, while $elu(*)$ represents the exponential linear unit activation function. The matrix W_l represents the weights associated with the connections between the neurons of the $l\text{-}1^{th}$ and l^{th} layer. The sizes of x_l, b_l, and W_l differ between $l = 1$ and $l = 5$ due to the varying number of neurons in the input and output layers.

2.4.2 Training Process

Obtaining large amounts of real-world data for training the ANN model can be challenging and time-consuming. In this thesis, the training set for a deep ANN is obtained using synthetic data from the forward problem solver. First, damage in arbitrary locations would be generated while causing the change of electrical properties distribution, then the simulated measurement on the specific distribution will be calculated from the solver. During training, the deep ANN adjusts its weights and biases to minimize the difference between the predicted and actual conductivity distribution, based on the synthetic data generated by the forward solver. The entire weight set $W_l = \{W_1, \ldots, W_5\}$ is determined during the training procedure using the sets for ERT, EIT, and ECT respectively as follows:

$$W = \arg\min_{W}\{\|\delta\sigma - x(W, \delta V)\|^2\} \tag{2.38}$$

$$W = \arg\min_{W}\{\|\delta\gamma_{\omega} - x(W, \delta V)\|^2\} \tag{2.39}$$

$$W = \arg\min_{W}\{\|\delta\varepsilon - x(W, \delta C)\|^2\} \tag{2.40}$$

Once the ANN is trained, it can be used to reconstruct the electrical properties distribution from new measurements obtained from a subject. This approach can be effective in solving the inverse problem of tomographic methods in practice. However, it is important to note that the accuracy of the reconstruction depends on the quality of the training data and the assumptions made by the forward solver.

2.5 Summary and Conclusion

This chapter introduces the mathematical background and numerical techniques used in ERT, EIT, and ECT for reconstructing the distribution of electrical properties. The methods allow for identifying regions of damage or strain based on changes in electrical properties. Classical solvers based on the FEM are discussed, along with the forward and inverse problems. In the inverse problem, absolute and difference imaging methods are explored, with absolute imaging offering quantitative reconstructions for assessing the severity of damage and difference imaging effectively compensating for measurement errors. Additionally, data-driven approaches using deep ANN are introduced, enabling fast and accurate reconstruction without intensive computations. These methods demonstrate the versatility and effectiveness of tomographic techniques in detecting and visualizing damage in various materials and structures.

CHAPTER 3 2D ERT FOR DAMAGE DETECTION ON ANISOTROPIC CFRP COMPOSITES

3.1 Introduction

The ERT method can effectively detect and locate damage in CFRP laminates due to the correlated electrical and mechanical fields created by the conductive carbon fibers within the material. Reconstructed conductivity maps could be efficiently transferred to damage state maps because of relation between electrical conductivity decrease and defects such as damages, fiber fracture and delamination [59]. However, electrical anisotropy is inherently generated in CFRP laminate with oriented carbon fibers and complex electrical mechanism from ply to ply. Therefore, a scalar conductivity distribution produced by classical ERT would include artifacts and inaccuracy if electrically anisotropic objects are involved and could not totally reveal the general damage state. Nonn et al. [77] discovered inescapable artifacts and shift of the reconstructed damage when applied classical ERT on damage localization of a anisotropic composite laminate. Many research recently conducted attempted to improve ERT solutions on anisotropic objects. Hamilton et al. [78] used a unique conductivity to represent the whole conductivity tensor, and Zhao et al. [79] connected determinant of the strain tensors to the ERT reconstructed scalar conductivity. Abascal et al. [80] conducted ERT on simulations of brain imaging function with the eigenvector ratio of conductivity tensor affixed. Gao et al. [81] utilized the method for damage detection on a 2.5D C/SiC composites, but determined the anisotropic conductivity tensor with additional long-strips samples. Hence an integrated non-destructive damage localization method including electrical anisotropy characterization and the difference between using classical and anisotropic ERT on electrically anisotropic objects are worthy of research and discussions.

In this chapter, anisotropic ERT was used to localize damage (in the form of holes) in electrically anisotropic CFRP laminates. The anisotropic conductivity tensor was first experimentally examined with non-destructive Montgomery method, then the fixed conductivity tensor ratio was leveraged to solve this inherently anisotropic ERT problem. Except the complex anisotropy inherently generated in CFRP laminates, electrical contacts are an additional experimental challenge for successfully examining CFRP laminates with the anisotropic ERT method. Instead of using standard silver paint or silver epoxy contacts, rivets were chosen as electrode contacts because of their contact stability, wide utilization as protection element in CFRP structures, and elimination of additional elements [82]. The performance of damage localization with anisotropic ERT was compared to classical ERT and the reconstructions were evaluated with position errors and shape deformation factors.

3.2 Methods

3.2.1 Anisotropic solver

In a general case, σ is generally a tensor rather than a scalar. For electrically isotropic object, a scalar conductivity reconstruction could represent the electrical property distribution. Nevertheless, classical ERT is not sufficiently capable to deal with electrically anisotropic material such as composite laminates discussed in this paper. In anisotropic ERT, the governing equation of ERT mechanism should be:

$$\nabla \cdot (\boldsymbol{\sigma} \nabla \phi) = 0 \text{ in } \Omega \tag{3.1}$$

with $\boldsymbol{\sigma}$ as a tensor. Given the inherent electrical anisotropy of the composite laminate and near zero conductivity of damage holes, only variation of the tensor with fixed eigenvectors and eigenvalue ratios was considered here, such that $\boldsymbol{\sigma}$ equals $\gamma\boldsymbol{\sigma}_0$ [80]. $\boldsymbol{\sigma}_0$ is a dimensionless fixed tensor inherently

given from the material properties. Its determinant det($\boldsymbol{\sigma}_0$) equals 1, thus γ could be used as the representative conductivity for anisotropic materials. The forward problem operator in anisotropic ERT produces adjusted voltage responses based on Equation (3.1), and the construction of sensitivity matrix is modulated as:

$$J_\gamma = -\int_\Omega \left(\nabla\phi_p\right)^T \boldsymbol{\sigma}_0 \nabla\phi_q dx^2 \tag{3.2}$$

with respect to representative conductivity γ. As same in classical ERT, Gauss-Newton iterative algorithm was also adopted here to obtain addition of representative conductivity $\Delta\gamma$ in each step until certain criterion was satisfied. After subtracting γ reconstruction of pristine state from damaged state, the defect distribution could be extracted given that defects like damage holes lessen local conductivity.

3.2.2 Montgomery Method

The anisotropic electrical property of the CFRP composite laminate was characterized for analysis of electrical behavior and modelling with conductivity fixed tensor. Montgomery method was adopted here owing to its non-invasive four-probe measurement approach which determines anisotropic conductivities of the object with only one specimen [79,83]. On the account of applied electrical current traveling in combination of three axes instead of only one principal direction, anisotropic conductivities are always evaluated through resistance tests of multiple long-strip samples. Except for inconvenience, those tests conducted on separate samples could be marred by low signal-to-noise ratio caused by high contact resistance of conventional electrodes attachments and low resistivity of individual carbon fibers, hence unmatched results [77,81]. Montgomery method takes advantage of the theorem that an anisotropic object could be hypothetically transformed into an equivalent with isotropic resistivity and alterative dimensions whose length

ratios are correlated to resistance ratio of the anisotropic object, i.e., $L_1' = L_2'$, $\sigma_1 \neq \sigma_2$, and $L_1 \neq L_2$, $\sigma_1 = \sigma_2$ as shown in Figure 3.1. The transformation is associated with equivalent electrostatic potentials dropping and the depth to which current flow within the object [83]. In this chapter, the process was simplified to two-dimensional (2D) anisotropic resistivities characterization with σ_1, σ_2 and σ_{12}, because only laminated material and in-plane spatial conductivity were investigated.

The normal conductivities were calculated through Montgomery measurements with four electrodes on the corner of one face of the square-shaped pristine CFRP laminates. Currents were applied through the electrode contacts on two neighboring corners, longitudinally and transversely, and voltage measurements were conducted between contacts on the other two corners. The normal conductivities σ_1 and σ_2 could be calculated based on the isotropic equivalent as [77,79,83]:

$$\frac{L_2}{L_1} \approx \frac{1}{2}\left\{\frac{1}{\pi}\ln\left(\frac{R_2}{R_1}\right) + \sqrt{\left[\frac{1}{\pi}\ln\left(\frac{R_2}{R_1}\right)\right]^2 + 4}\right\} \tag{3.3}$$

$$\sigma_1 = \frac{1}{\sinh\left(\frac{\pi L_2}{L_1}\right)}\frac{8}{\pi d}\frac{L_1'}{L_2'}\frac{L_2}{L_1}\frac{I_1}{U_1} \tag{3.4}$$

$$\sigma_2 = \frac{1}{\sinh\left(\frac{\pi L_1}{L_2}\right)}\frac{8}{\pi d}\frac{L_2'}{L_1'}\frac{L_1}{L_2}\frac{I_2}{U_2} \tag{3.5}$$

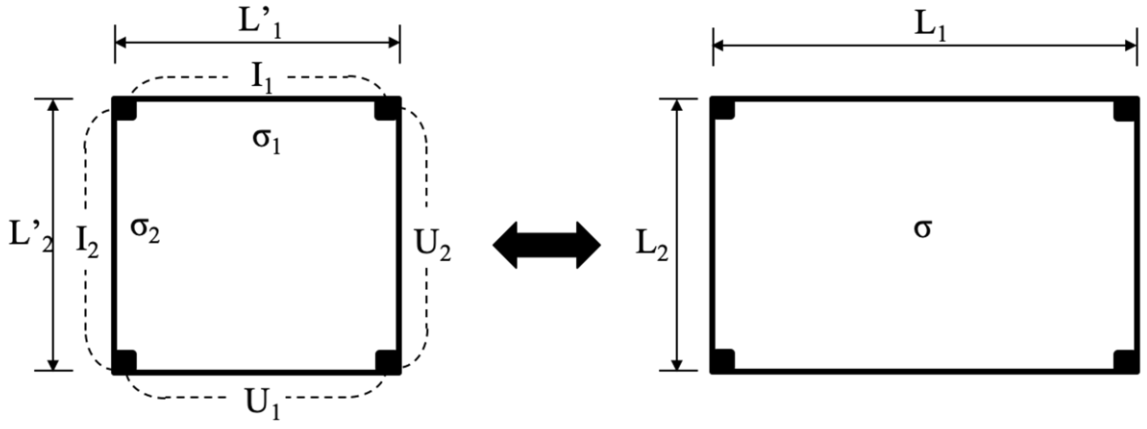

Figure 3.1: Four-probe Montgomery measurements on an anisotropic object are transformed to its isotropic equivalent.

where d is the specimen's thickness, U_1, U_2 and I_1, I_2 are voltage responses collected and currents injected in the transverse and longitudinal direction, respectively.

Measuring electrical anisotropy in principal crystallographic directions make the four-probe Montgomery method appropriate for anisotropy characterization of the [0°/90°/0°] layup composite laminate, given the high coincidence between global coordinate axes and electrically principal axes of the laminate [83]. However, the principal axes would shift from the global coordinate axes slightly with a small angle θ due to manufacture errors like carbon fiber and ply misalignments. So, the measured conductivity tensor $\boldsymbol{\sigma}$ would differ from the perfectly orthotropic $\boldsymbol{\sigma}'$ with relations shown in Equation (3.6).

$$\boldsymbol{\sigma} = T\boldsymbol{\sigma}'T^T = \begin{pmatrix} \cos\theta & \sin\theta \\ -\sin\theta & \cos\theta \end{pmatrix}\begin{pmatrix} \sigma_1' & 0 \\ 0 & \sigma_2' \end{pmatrix}\begin{pmatrix} \cos\theta & -\sin\theta \\ \sin\theta & \cos\theta \end{pmatrix} = \begin{pmatrix} \sigma_1'\cos^2\theta + \sigma_2'\sin^2\theta & (\sigma_2' - \sigma_1')\cos\theta\sin\theta \\ (\sigma_2' - \sigma_1')\cos\theta\sin\theta & \sigma_2'\cos^2\theta + \sigma_1'\sin^2\theta \end{pmatrix} \tag{3.6}$$

Hinckley et al. [84] and Yurgartis et al. [85] found that fiber misalignments of prepreg is usually axially symmetric, and ply orientation of high-quality commercial laminates could be maintained within two degrees of stated nominal value. Considering the small angle variation which maximumly would only results approximate 0.05 change on shear conductivity and 0.005 change on normal conductivities, $\boldsymbol{\sigma}$ could assume to be approximating $\boldsymbol{\sigma}'$ in this study. In Section 3.3, the influence of misalignments in ERT measurements was detailed described which substantially stands for the feasibility of conductivity tensor approximation. With assumption that electrical principal axes coincide with global axes, the conductivities components of CFRP laminates were measured with Montgomery method as σ_1 = 11.77 (Ωmm^{-1}) and σ_2 = 6.35 (Ωmm^{-1}). The

conductivity ratio of σ_{11}/σ_{22} = 1.85, which is close to the theoretical value of 2 (classical laminate theory) for the [0°/90°/0°] stacked laminates.

3.3 Simulation Details and Results

3.3.1 Damage Localization Simulation Results

To examine the feasibility of this anisotropic ERT solver to localize damages on the anisotropic CFRP composite laminate, simulations were conducted in advance. A 2D model was built in Abaqus with dimension 250×250 mm^2, and 16 electrodes were equidistantly spaced on the boundary. A supposed circular hole damage was imposed in the plate which theoretically reduce conductivity inside the circle to nearly zero. Linear triangular elements were leveraged here for its fast operability and adaptability for different shapes. First, isotropic material was considered for evaluation the functionality of the ERT solver. The reconstruction process was conducted with Gauss Newton iterative algorithm based on voltages measurements from opposite injection pattern. Then, simulation tests were conducted to evaluate capability of classical and anisotropic ERT on anisotropic plates. The pristine state is an anisotropic plate with electrical conductivity ratio of 1.85:1 in two directions, and the damaged state is the plate with a damage hole where representative conductivity γ was set to 0. At last, the influence of ply misalignments was considered in simulation to evaluate our approximation was of reason.

The functionality of ERT solver on an isotropic material is shown in Figure 3.2a, the reconstructed representative conductivities were normalized by the maximum amplitude. And the errors between simulated voltages $V(\sigma)$ and target voltages V_m in iterations shown in Figure 3.2b validate the high performance of Gauss-Newton optimization method. The reconstructed conductivity distribution perfectly reveals the position and size of the hole damage, which

substantially support the performance of the iterative ERT solver. To systematically study how electrical anisotropy influences ERT reconstruction results, three fixed conductivity tensors were considered to simulate voltage measurements. In Equation (3.7), $\boldsymbol{\sigma}_0'$ and $\boldsymbol{\sigma}_0''$ expressed the anisotropy resulted from unequal number of plies in principal directions, and $\boldsymbol{\sigma}_0'''$ considered the anisotropy resulted from maximum ply misalignments.

$$\boldsymbol{\sigma}_0' = \begin{pmatrix} 0.735 & 0 \\ 0 & 1.360 \end{pmatrix}, \boldsymbol{\sigma}_0'' = \begin{pmatrix} 1.360 & 0 \\ 0 & 0.735 \end{pmatrix}, \boldsymbol{\sigma}_0''' = \begin{pmatrix} 1.354 & -0.014 \\ -0.014 & 0.732 \end{pmatrix} \tag{3.7}$$

Performances of classical and anisotropic ERT solver on the anisotropic laminate were both evaluated by criteria proposed by Adler et al. [86]. The elements with negative conductivity lower than one-fourth of minimal conductivity value were regarded as being within the defected region corresponding to a damage hole. The position error was exhibited as the distance between center of actual imposed damage hole and the centroid of the reconstructed defect region. The shape deformation factor determined by the areal portion of reconstructed defect region that was not

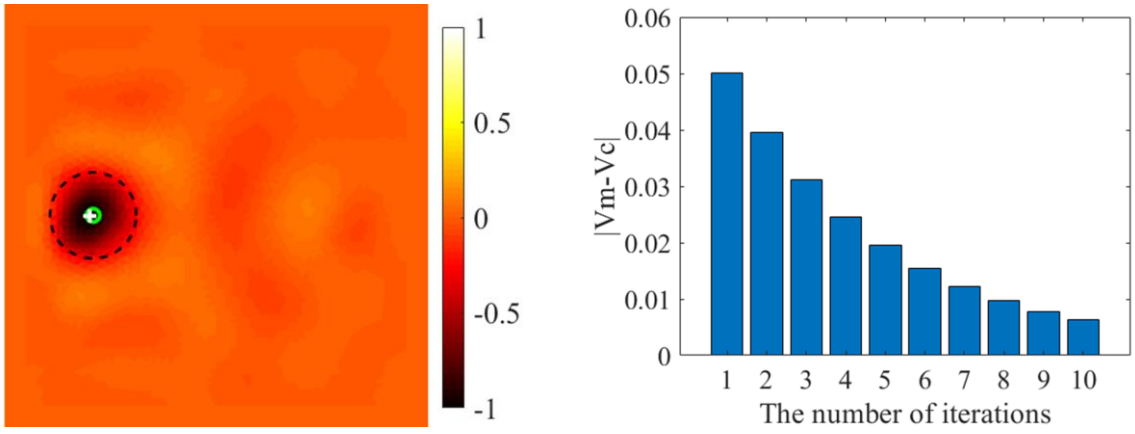

(a) (b)

Figure 3.2: (a) Reconstructed representative conductivity distribution of a damaged isotropic material using classic EIT solver. The hole damage center is marked by a white '+', and the EIT damage center is marked by a green 'o'. (b) Errors between simulated voltages Vc and dummy measured voltages Vm with iterations.

included in the equal-area circle, represented by the black dashed line in reconstructions, could be recognized efficiently in the images. These criteria are commonly used in resolution evaluation of ERT method and speak volumes in anisotropic ERT study [77,87].

The reconstructions of representative conductivity γ distribution with opposite current injection pattern are shown in Figure 3.3. Detailed discussion of current injection patterns would be stated in Section 3.3.2 and Section 3.4 with experimental data. With anisotropic materials, classical ERT could reconstruct a rough location of the damage hole (Figure 3.3a, 3.3c, 3.3e and 3.3g), however, the results are with significant distortion and inaccuracy. Not only the shape of damage holes got stretched, also unexpectable noises were induced around the damage area. When using classic ERT to solve data obtained from $\boldsymbol{\sigma}_0 = \boldsymbol{\sigma}_0'$, where the conductivity is higher in direction 2 than in direction 1, the reconstructed damage was elongated in direction 2 while squeezed in direction 1. Similar phenomenon is shown in Figure 3.3c and 3.3g with measurements calculated from a plate with $\boldsymbol{\sigma}_0 = \boldsymbol{\sigma}_0''$. Moreover, the bright artefacts shown in the first and third columns of

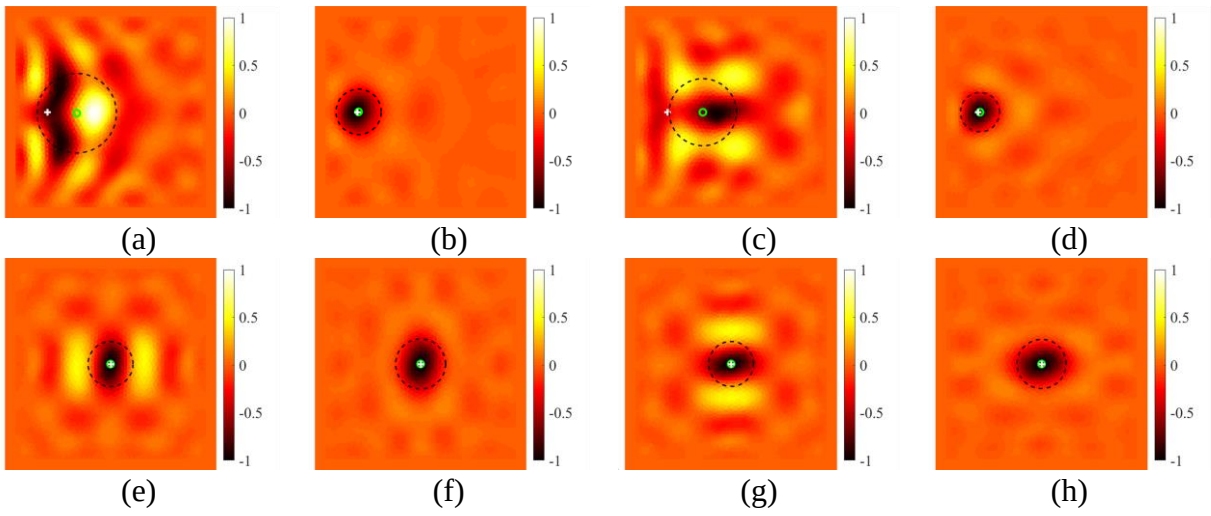

Figure 3.3 Representative conductivity γ distributions were reconstructed with simulated measurements with conductivity fixed tensor $\boldsymbol{\sigma}_0 = \boldsymbol{\sigma}_0'$ (first and second columns) and $\boldsymbol{\sigma}_0 = \boldsymbol{\sigma}_0''$ (third and fourth columns) by using classical EIT (first and third columns) and anisotropic EIT (second and forth columns). The damage holes were localized near the boundary (first row) and in the center (second row). The imposed damage center and EIT damage center are marked by a white '+' and green 'o' respectively.

Figure 3.3 may provide false information in decision-making step by mistakenly being recognized as mechanically generated conductivity increase. Anisotropic ERT solver with initially built-in fixed conductivity tensor $\boldsymbol{\sigma}_0'$ or $\boldsymbol{\sigma}_0''$ that perfectly avoided the reconstruction distortion and shift of damage center, shown in the second and fourth columns of Figure 3.3. However, the results were still influenced by sensitivity difference in the domain. Due to the low sensitivity in the center, the reconstructions of holes shown in the second row of Figure 3.3 exhibit stretches with certain levels even if utilizing anisotropic ERT.

Voltage measurements generated from a plate with $\boldsymbol{\sigma}_0 = \boldsymbol{\sigma}_0'''$ that included maximum possible ply misalignments were also tested here. The reconstructions of γ distribution solved by anisotropic ERT with approximate conductivity fixed tensor $\boldsymbol{\sigma}_0''$ which neglected ply misalignments are shown in Figure 3.4a and 3.4b. The images exhibit great coincidence with reconstructions in Figure 3.3d and 3.3h. This consistency demonstrates that assumption of coincidence between electrical principal axes and global axes does not influence ERT

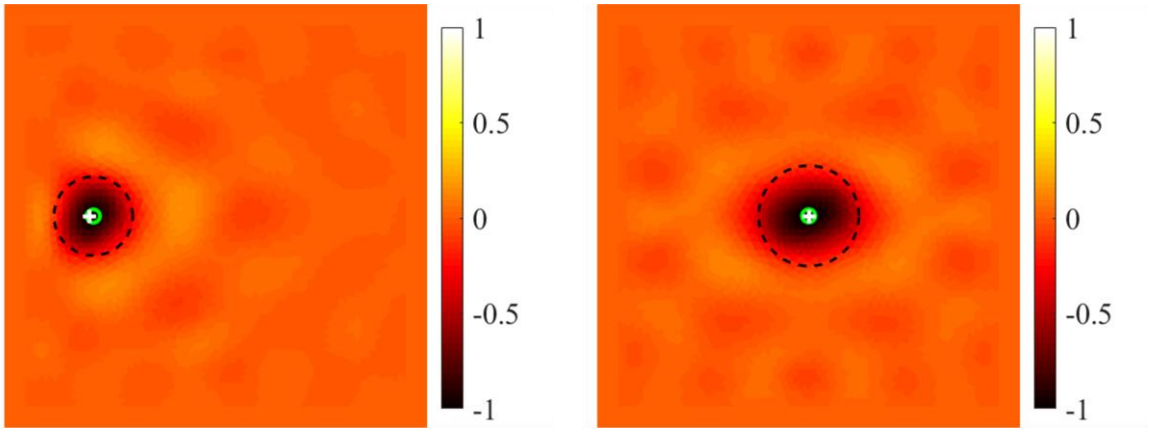

(a) (b)

Figure 3.4: Representative conductivity γ distribution were reconstructed with simulated measurements with conductivity fixed tensor $\boldsymbol{\sigma}_0 = \boldsymbol{\sigma}_0'''$ by using anisotropic EIT with built-in tensor $\boldsymbol{\sigma}_0 = \boldsymbol{\sigma}_0''$. (a) A damage hole was located near boundary and (b) a damage hole was in the center. The supposed damage center and EIT damage center are marked by a white '+' and green 'o' respectively.

reconstruction of the [0°/90°/0°] composite laminate used in this chapter. Hence, the small errors resulted from ply misalignments could be neglected for convenience in the following discussions.

3.3.2 Anisotropy discussion in simulation

The electrical anisotropy tends to alter current flow in the plate towards the direction with higher electrical conductivity, which differentiates the electrical field and voltage measurements from the one generated in an isotropic material plate. Thus, simply utilizing classical ERT solver with voltage measurements of anisotropic objects easily produces distorted reconstruction. The normalized differences between simulated voltage measurements in an isotropic plate and an anisotropic plate with fixed tensor equal to $\boldsymbol{\sigma}_0'$ were calculated and plotted in Figure 3.5. Significant normalized differences of voltage responses arise from the electrically anisotropic model, and the high normalized differences were generated from voltage measurements far away from the pair of current injection electrodes. These low measurements play a more important role in the inverse problem than measurements with larger response because they include more extensive interior information.

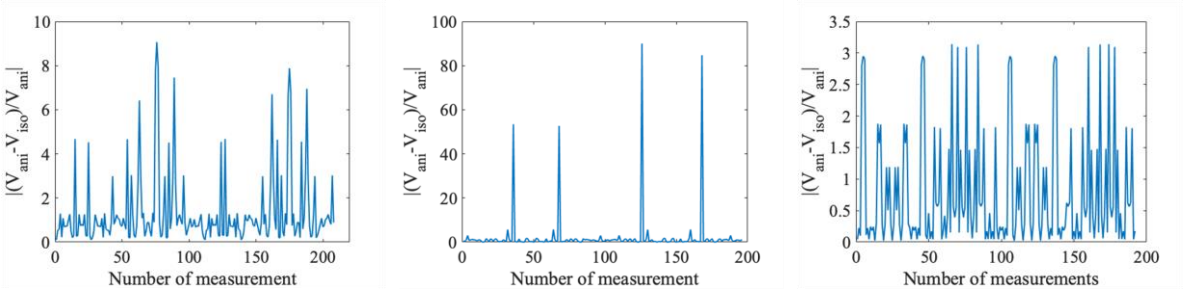

(a) (b) (c)

Figure 3.5: Normalized differences of simulated voltage responses between an isotropic model and an anisotropic model with (a) adjacent pattern, (b) diagonal pattern, and (c) opposite pattern were plotted.

3.3.3 Current injection patterns

The delicacy of voltage measurements renders the difficulties of ERT reconstruction in practice considering experimental noise. Besides reducing noise by enhancing data acquisition (DAQ) system, choosing current injection pattern with high sensitivity is required to minimize signal to noise ratio (SNR) in practice. Sensitivity map reveals how one specific measurement responds to disturbance from each element, which assist to visualize highly sensitive area in the region of interest. To discuss sensitivity among three different current injection patterns, the sensitivity map for each measurement were overlaid in addition and normalized by Equation (3.8) and (3.9). Here, J_{sum} is normalized sensitivity in addition, i and k mean each measurement and each element, and n is the number of total measurements.

$$J_{(ik)} = \frac{\Delta V_i}{\Delta \gamma_k} \tag{3.8}$$

$$J_{sum(k)} = \frac{\sum_{i=1}^{n} J_{(ik)}}{n} \tag{3.9}$$

Figure 3.6 demonstrates a unit change of electrical conductivity of a single element reacting on the set of boundary measurements in total for each pattern. Sensitivity reaches to highest on the boundary and mitigate to the center for all patterns. High sensitivity speaks volumes in practice

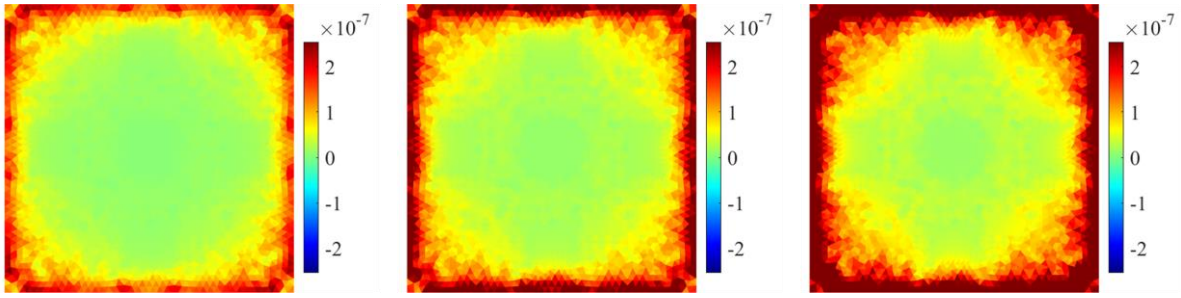

(a) (b) (c)

Figure 3.6: Normalized sensitivity maps in summation with (a) adjacent pattern, (b) diagonal pattern, and (c) opposite pattern were plotted.

with more reliable experimental data and further accurate reconstruction images. In opposite pattern, current is injected between electrode pairs positioned horizontally or vertically, while in diagonal pattern current is injected 45° or -45° angle across the domain. They both provide higher spatial sensitivity over the entire material than adjacent pattern because of current spreading [81,88]. The performance of three injection patterns will be further exhibited in Section 3.4 with experimental data.

3.4 Experimental Details and Results

3.4.1 Experimental Details

The defect detection ability of anisotropic ERT solver was evaluated experimentally with commercial electrically anisotropic CFRP composite laminate. Sixteen electrodes with rivets contact were installed on the boundary of the CFRP composite laminate plate, with four on each side. The contact between rivets and the laminate was improved by conductive silver grease which offered stable contact impedance. Cuts were made on the edges between electrodes to prevent short circuits between adjacent rivets and enhance electric field propagation in the whole domain. Those rivets were directly connected to a multiplexer and a microcontroller for current injection and voltage measurements depending on different current injection patterns. Currents of 10 mA were injected in the specific pairs of electrodes by a Keithley 6220 precision current source and voltages were measured by a Keithley 2182A nanovoltmeter (Figure 3.7a). Delta mode was utilized to couple the current source and nanovoltmeter because it ensured reduced noise and accurate measurements by eliminating the effects of thermal offsets. A 5 mm hole (around 0.03% of the plate area) was drilled in the plate as a damage in the damaged state. The hole was enlarged to 15 mm (around 0.3% of the plate area) in the second damaged state (Figure

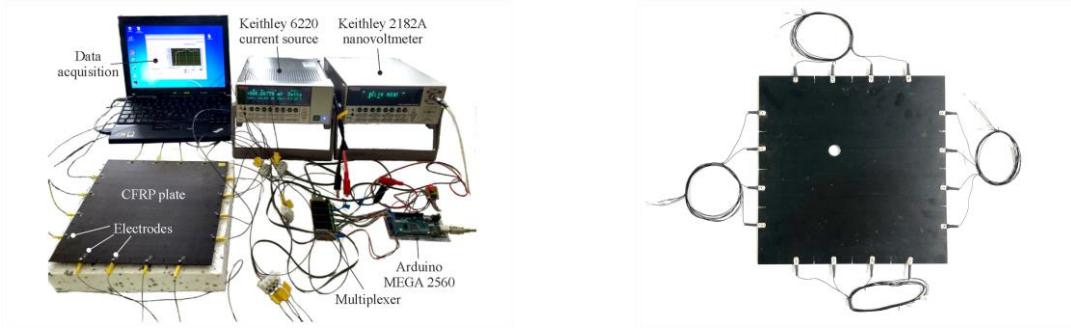

(a) (b)

Figure 3.7: (a) The CFRP laminate was examined by EIT data acquisition (DAQ) system in the pristine state [14]. (b) The CFRP laminate was drilled with a 15 mm hole inside.

3.7b). Adjacent, diagonal and opposite current injection patterns were all conducted, and the average of two measurements for each pattern were employed for noise reduction.

3.4.2 Experimental voltage measurements

The model was completely rebuilt to imitate the real plate. Voltages on the boundary were generated from the FE method solver and compared with experimental measurements. The voltage measurements in the pristine state and voltages from the anisotropic model for all three patterns are shown in Figure 3.8. Considering the error of electrodes installation, inaccuracy introduced by environmental noise and complexity of current flow in actual 3D composite plate, mismatches that

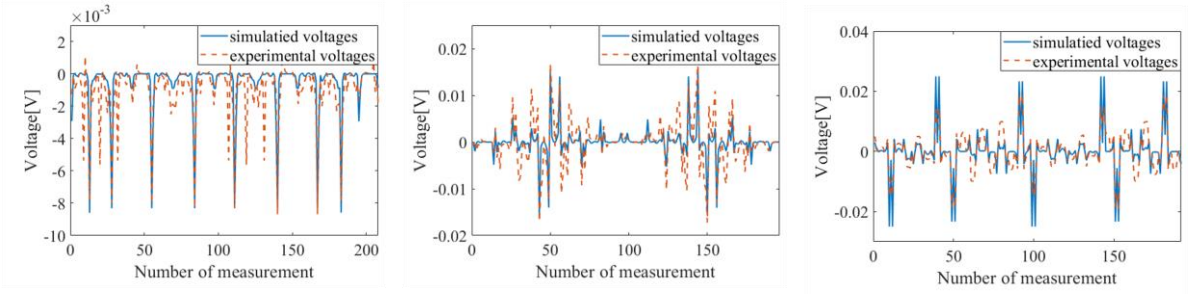

(a) (b) (c)

Figure 3.8: Simulated voltages were compared to experimental voltage measurements with (a) adjacent pattern, (b) diagonal pattern, and (c) opposite pattern.

varies experimental data from modeling measurements. However, the mismatches are admissible because only the difference between pristine and damaged states would make an impact.

The existences of damages such like cracks, delamination and fiber fractures would change spatial mechanical and electrical properties of the composite, alter electrical field propagation and hence different voltage responses from pristine state measurements. Assuming there was no other influence on the structure, the voltages change corresponding spatial conductivity change could certify presence of damages. In this study, only a damage hole where electrical conductivity was nearly zero was drilled. In opposite pattern measurements, the maximum voltage difference between pristine and damaged states is in the range 10^{-4} V, which is quite small compared to the maximum voltage that is in the range 10^{-2} V. These small variations were resulted from the interior low sensitivity and may be damaged with noises. Therefore, image artefacts are usually unable to be eliminated in ERT reconstructions with experimental data.

3.4.3 ERT Results with Experimental Data

Anisotropic ERT and classical ERT were both employed with the experimental data to detect the damage hole in the plate. To improve the reconstruction results, regularization hyperparameter (λ) which influences the reconstruction quality should be optimized. Low λ value ensures higher level of diffusion and spatial resolution toward center of the domain by promoting small singular value decomposition (SVD) components which contain more information away from boundary electrodes. However, overweighting small SVD components may generate reconstruction without physical meaning due to noise contamination [58]. The shown reconstructions were solved with the optimal hyperparameter selected by L-curve method which balances the norm of ($\mathrm{d}\gamma$) versus the norm of minimizing penalty part ($J\mathrm{d}\gamma$-$\mathrm{d}V$). The optimal

hypermeters selected in this chapter for adjacent, diagonal, and opposite pattern were 10^{-10}, 10^{-8} and 10^{-5} respectively. Besides, choosing proper current injection pattern which enhances image quality would benefit diagnosis in the decision-making procedure. The representative conductivity reconstruction normalized by the maximum value generated with measurements from three patterns are shown in Figure 3.9. The first row with reconstructions from classical ERT solver exhibits large position errors, shape deformations and areal noises for every current injection pattern. Reconstruction with adjacent pattern (Figure 3.9a) are with an elongated damage and artificial defects downside. Likewise, reconstructions with diagonal and opposite patterns shown in Figure 3.9b to 3.9c display damage shift, shape deformation and bright noises with positive value outside of the defected hole. These outer noises originally express different meshed elements responding to the boundary electrical potential change, which are usually with relatively small values compared to values of real defects. Nevertheless, the measurements did not conform to the

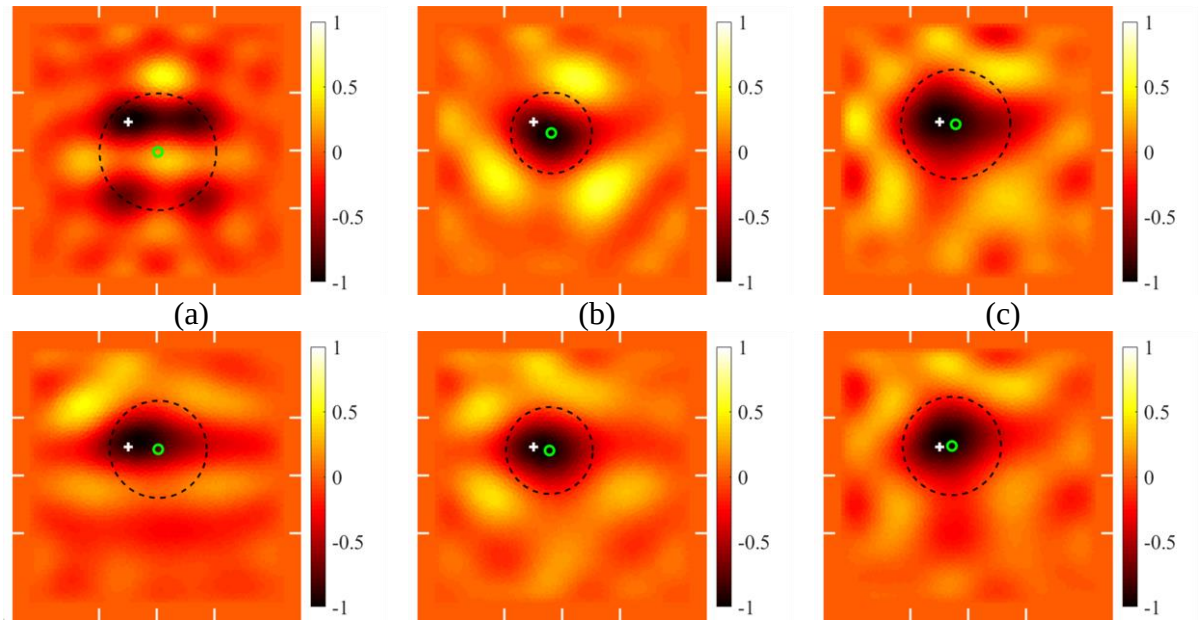

Figure 3.9: Representative conductivity distributions were reconstructed with (a)-(c) classical EIT solver and (d)-(f) anisotropic solver. The first, second and third columns respectively correspond to adjacent, diagonal, and opposite pattern. The actual damage center and EIT damage center are marked by a white '+' and green 'o' respectively.

classical ERT model due to the disturbance of electrical anisotropy and produced noises which were hard to be characterized as numerical errors or mechanical conductivity increase such as compressive overstrains.

The reconstructions solved by anisotropic ERT shown in Figure 3.9d to 3.9f exhibit more coincidence with circular damage hole and less artifacts beyond the defected hole. Consistent with the sensitivity study shown in Figure 3.6, the results solved with measurements from the opposite and diagonal patterns eclipse results with measurements from the adjacent pattern, expressing smaller position error and less shape deformation in the direction of higher conductivity. Except from the error induced by noises from experimental measurements, the low sensitivity in the damage hole location and neglect of through thickness anisotropy explain the imperfection of reconstruction produced by anisotropic ERT solver. These results are consistent with reconstructions in Section 3.3.1, shown in Figure 3.3h, where the reconstructed damage hole remains shape deformation even with anisotropic ERT solver due to the low central sensitivity. From Nonn et al. [77], solutions form classical ERT with measurements generated by a detailed 3D model shows higher consistent artefacts with experimental results than leveraging a 2D model. This demonstrates the existence of artefacts beyond region of the hole even with anisotropic ERT solver. In general, the reconstruction with measurements from the opposite pattern exhibits better spatial accuracy with small position errors, shape deformation, and less artefacts among these three current patterns. Therefore, the opposite pattern was used for following study.

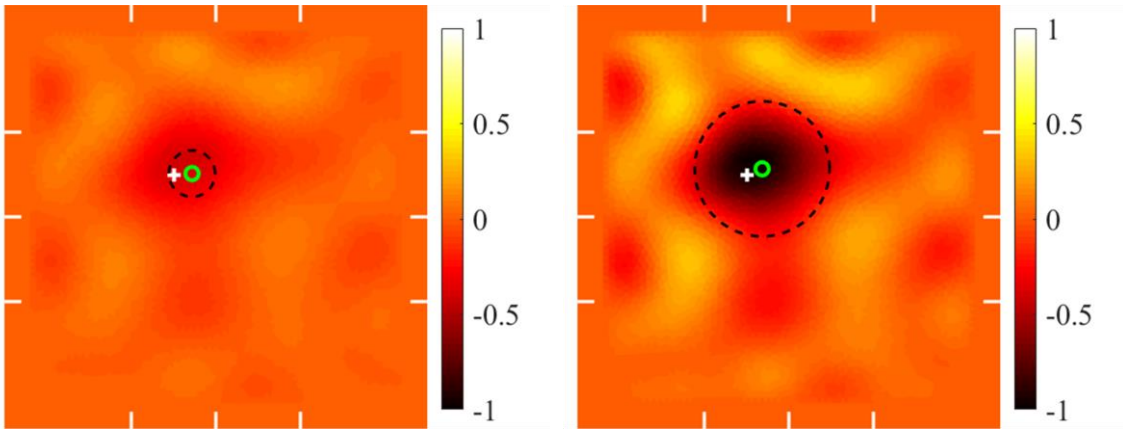

(a) (b)

Figure 3.10: Representative conductivity distributions of composite laminates with (a) a 5 mm hole and (b) a 15 mm hole were solved by using the opposite pattern measurements. The actual damage center and ERT damage center are marked by a white '+' and green 'o' respectively.

According to the comparison above, anisotropic ERT solver displayed superior performance than classical ERT on anisotropic materials. While damage detection in composite laminates consists of not only the localization of defects but also the evaluation of deterioration degree. Thanks to a 5mm hole (0.03% of the plate area) and a 15mm hole (0.3% of the plate area) were drilled in sequence during the experiments, the two sets of data were inputted in the solver for severity diagnosis. The reconstructed representative conductivity was normalized with the maximum absolute value obtained from the damaged case with a 15 mm hole, as thus the comparisons were clearly revealed. It is clearly shown the diameter of equal-area circle in the reconstruction with a 15 mm hole is around 3 times of the one with a 5 mm hole, expressing the anisotropic ERT solver has potential to quantitively evaluate the damage propagation in composite laminates. The reconstructed image shown in Figure 3.10b with a 15 mm damage hole approached the realistic situation more with a smaller position error, which was benefited from its greater responses in boundary voltage measurements due to the damage.

3.5 Conclusion

This chapter proposed an integrated non-destructive anisotropic characterization and ERT solver for defect detection on an electrically anisotropic CFRP laminate. The anisotropic properties resulted from UD plys and misalignments were also considered and investigated. The anisotropic ERT solver exhibited better performance on damage assessment of the CFRP laminate than utilizing classical ERT, producing solutions with much less shape deformations, position errors and artefacts. The advantages of this solver on anisotropic material compared to classical ERT were discussed both in simulation and experiments. Besides, different current injection patterns were investigated, and the opposite pattern showed excellent ability to accurately localize and quantify defects far away from boundary electrodes than adjacent and diagonal patterns. The 2D ERT solver could efficiently reconstruct conductivity distribution corelated to defects distribution, however, errors generated from neglect of through-thickness anisotropy limit its performance in material damage assessment. In the future study, a 3D anisotropic ERT method with detailed model needs to be developed, and the ability of ERT method on detecting defect propagation should be investigated.

Acknowledgement

Chapter 3 is, in full, currently being prepared for submission for publication of the material. Shu, Yening. The dissertation author was the primary investigator and author of this material. This project was conducted in the Institute of Structural Lightweight Design at Johannes Kepler University Linz and supported by the Christian Doppler Laboratory for Structural Strength Control of Lightweight.

CHAPTER 4 MULTI-DEFECT DETECTION IN ADDITIVELY MANUFACTURED LATTICE STRUCTURES USING 3D ERT

4.1 Introduction

Lattice structures are 3D configurations of interconnected struts and nodes that offer superior mechanical, thermal, and electrical properties compared to conventional materials [3,13]. They are widely used in various industries due to their high strength-to-weight ratios [4–6,11]. AM techniques have enabled the fabrication of intricate lattice structures, but their performance is highly dependent on manufacturing quality [27,28]. Minor defects such as clogs, voids, and thermo-mechanical issues can compromise the structural integrity of the part, leading to failure [19]. Therefore, identifying the locations and severities of defects and damage is required, whether they occur during manufacturing or while in service.

This chapter aims to leverage 3D ERT to directly detect and accurately identify the locations of damaged struts in cellular lattice structures. ERT aims to reconstruct the conductivity distribution of a conductive target that is directly correlated to damage or strain states by using only boundary electric potential measurements [52,53]. The utilization of a target's electromechanical properties exempts inspection from complex operations [52,57].

A major challenge when using electromagnetic tomographic methods is that the accurate reconstruction of electrical properties (e.g., conductivity) distribution around the interior of the target is challenging due to the lower sensitivity of measurements in its interior versus near the boundaries [89,90]. This limitation may cause inaccurate localization and quantification of defects and may be even more severe for open cell lattice structures. To solve this problem, Baltopoulos et al. [58] proposed reserving smaller SVD components of the sensitivity map for efficient conductivity reconstruction of the center region by choosing a smaller hyperparameter, but this

solution may introduce additional artifacts in the region of interest, hence deteriorating reconstruction quality. Li et al. [90] used a normalized sensitivity map to compensate for the low central sensitivity, but the proposed normalized methods are element-based and are computationally intensive. The element-based normalization is effective for detecting perturbations with large-area conductivity change. However, the method is not as effective for small-area defects, such as small defects in open cell lattice structures with small cross-section struts, where reconstructions would still suffer from image artifacts. These image artifacts may result in inaccurate defect detection or incorrect decisions. Thus, to improve reconstruction performance with respect to small perturbations, the normalized sensitivity map should be adjusted to be capable of compensating for low central sensitivity and restraining image artifacts.

In this chapter, a high-throughput, 3D, iterative, absolute conductivity distribution ERT system was presented for identifying single and multiple damaged struts in conductive cellular lattice structures. The significance of this work is that the ERT algorithm employs a strut-based normalized map that preconditions the sensitivity map for enhancing conductivity reconstruction sensitivity while mitigating artifacts due to the ill-conditioning of the ERT inverse problem. The efficacy of this method was assessed by quantifying the relationship between damage severity and the corresponding reconstructed conductivity changes. Both numerical simulations and corresponding experiments of cellular lattice structures with different damage features were performed. To demonstrate that ERT could examine conductive cellular lattice structures, experiments were performed using 3D-printed polymer cellular lattice structures, which were then coated with a soluble, sacrificial, and electrically conductive nanocomposite thin film. Damage scenarios with single and multiple damaged struts were considered.

4.2 Theory and Methods

It is known that localized damage (e.g., voids, cracks, or broken parts) in the target can prevent or limit electric current propagation through that specific region. Therefore, identifying the magnitudes and locations of localized conductivity changes in reconstructions would enable direct visualization of damage severity and their respective locations. In this section, the theory of the adjusted absolute ERT method is introduced first. Then, the strut-based normalized sensitivity map and the quantitative defect detection method are discussed in detail.

4.2.1 Adjusted Absolute Imaging

To quantitatively identify the damage in the lattice structure, absolute imaging which could reconstructs absolute conductivity distribution should be adopted in this chapter. However, in practical ERT implementations, errors from measurements, inaccuracies from spatial inhomogeneity, and the modeling of electrode positions could affect the accuracy of the reconstruction result of the target in the damaged state when using absolute imaging directly [67]. In this chapter, an adjusted absolute imaging method which efficiently compensates for those errors was employed, and the workflow is illustrated in Figure 4.1. This method calculates the

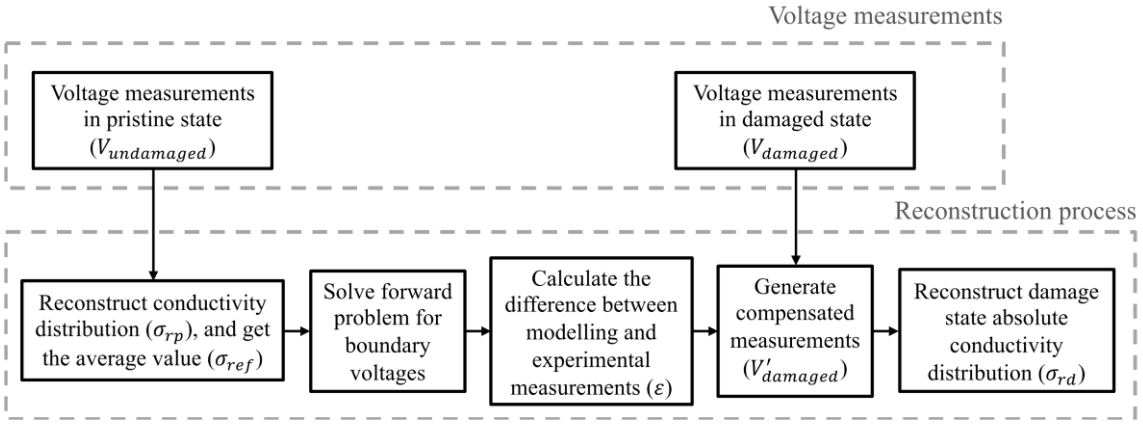

Figure 4.1: The flow chart illustrates the adjusted absolute imaging process.

modeling error (ε) between experimental undamaged state measurements ($V_{undamaged}$) and the voltages $V(\sigma_{ref})$ calculated by the assumed homogenous model, before locally subtracting them from damaged state measurements ($V_{damaged}$), as is shown in Equations (4.1) and (4.2). The undamaged state measurements usually could be easily obtained from itself or other qualified structures in a mass production [56,67]. The updated measurements ($V'_{damaged}$) compensate for modeling inaccuracy and are directly used to reconstruct the absolute conductivity distribution (σ_{rd}) of the target. This mechanism enhances reconstruction quality by transforming the inverse problem from a global to a local minimization process [67].

$$\varepsilon = F(\sigma_{ref}) - V_{undamaged} \tag{4.1}$$

$$V'_{damaged} = V_{damaged} - \varepsilon \tag{4.2}$$

4.2.2 Modification of the Sensitivity Map

In ERT, reduction of sensitivity in the target's central causes relatively low reconstructed conductivity changes and more image artifacts, especially considering measurement noises [88,90]. To address this limitation, a strut-based normalization procedure is proposed and can be imposed on the sensitivity map to improve σ reconstruction.

Figure 4.2 outlines the procedure for the strut-based normalization process, where the objective is to obtain uniform boundary-voltage-to-conductivity-perturbation sensitivity in each strut (*i.e.*, regardless of their location in a cellular lattice structure). To calculate the normalized sensitivity, the reconstruction results from classical ERT for each damaged state (where a damaged strut *k* is assigned with 0 S/m) are obtained first in steps (1) to (3). A total of *s* damaged states are solved considering the total of *s* number of struts in the structure. Among all states, the largest

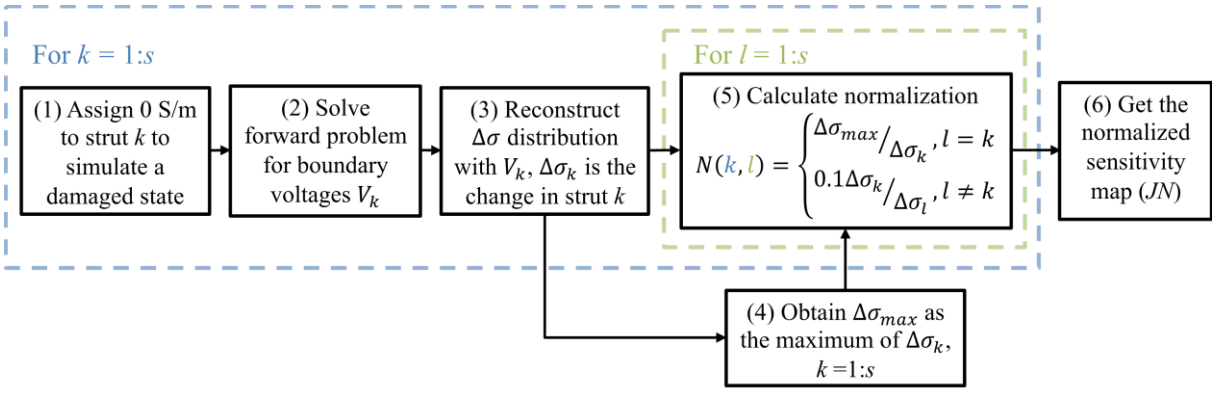

Figure 4.2 The flow chart illustrates the calculation of the normalized sensitivity map.

reconstructed change within the damaged strut ($\Delta\sigma_{max}$) could be acquired in step (4) when damage is assigned on the boundary strut. During the calculation of the strut-wise normalization matrix (N) in step (5), diagonal components of the matrix N are normalized to compensate for relatively low responses in the central struts, and the non-diagonal components are used for suppressing artifacts to $0.1\sigma_k$, which would not affect the defect evaluation. With this normalization, the adjusted sensitivity map could be obtained as JN in step (6), and the change in voltage measurements corresponding to a single perturbation would be:

$$\delta V = (JN)(N^{-1})\delta\sigma \tag{4.3}$$

The results, which show the benefits of using the normalized sensitivity map to improve interior sensitivity and mitigate image artifacts, will be discussed in Sections 4.3 and 4.4.

4.2.3 Representative Strut Conductivity and Defect Quantification

Damage severity within each strut can be reflected by a single index, which is referred to in this work as strut representative conductivity, σ_s. Here, σ_s is the equivalent conductivity of a damaged strut, which is calculated using the electric potential drop between the two ends of the

strut, V_{ab}, while assuming its dimensions remain the same. V_{ab} is affected by the size, shape, and amount of damage developed in the strut. With known damage features shown in Figure 4.3, σ_s could be calculated as:

$$V_{ab} = \int_0^L \frac{I}{A_r \sigma_0} dl \tag{4.4}$$

$$\sigma_s = \frac{IL}{V_{ab} A_0} = \frac{L}{A_0 \int_0^L \frac{1}{A_r \sigma_0} dl} \tag{4.5}$$

where σ_0 is the material conductivity in its undamaged state, L is the length of the strut, and A_r is the residual area (*i.e.*, the cross-sectional area where the defected region A_d is subtracted from the undamaged cross-section A_0) for a differential length, dl.

During ERT inspection, defects in struts with small cross-sectional areas could not be effectively localized given the limited resolution and electric field propagation pathways in topologically ordered open cell structures. However, the reconstructed conductivity (σ_r) in each strut could be used to examine damage severity. Here, σ_s which corresponds to the damage could

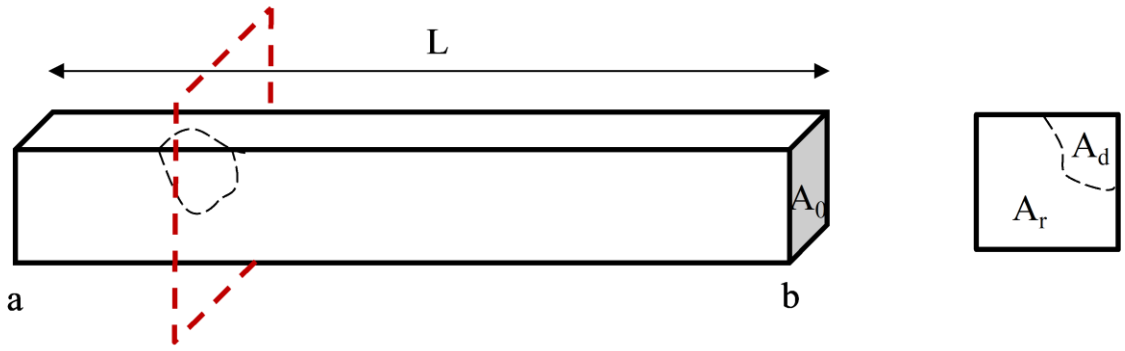

Figure 4.3: Damage that was introduced in a strut is illustrated, and the strut representative (σ_s) conductivity could be further calculated.

serve as a comparison parameter with respect to σ_r solved by ERT with an invariant struts model. In this study, σ_r was compared with σ_s in both simulations and experiments to validate the quantitative defect detection capabilities of the proposed ERT method.

4.3 Simulation Details and Results

4.3.1 3D ERT Numerical Simulations

The feasibility of 3D ERT for detecting and localizing damaged struts in cellular lattice structures was first assessed with numerical simulations. A 3×3×1 lattice structure with cubic unit cells consisting of 40 mm long and 2×2 mm^2 cross-section struts was constructed in Abaqus, as is shown in Figure 4.4; the cellular lattice structure was meshed using 9,229 tetrahedral elements. Electrodes were defined at the 24 intersecting nodes along the boundaries. The conductivity of all the elements was assumed to be 1,000 S/m, based on the resistance measurements of the (carbon nanotube) CNT thin film coat used in the following experiments.

A quantitative damage assessment study was performed by executing the 3D ERT forward and inverse algorithms on the undamaged lattice structure, as well as on assumed single-defect cases. Defect severity was simulated by considering two defect propagation situations in an interior

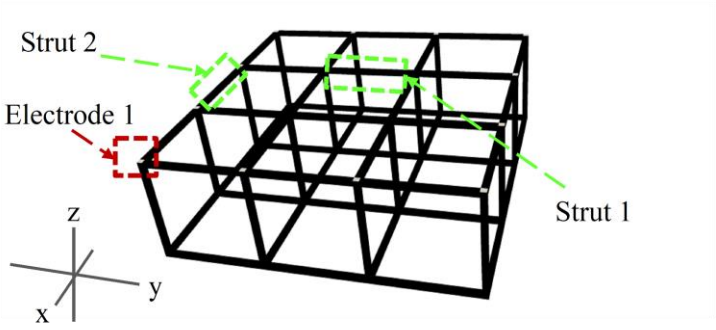

Figure 4.4: A 3×3×1 lattice structure model was created in Abaqus. Electrodes in the upper z-plane are marked in white.

strut (strut 1), where the size of the damage feature could grow along the length or depth of the strut. Damage propagating along the strut length was modeled by assigning 0 S/m to adjacent finite elements in the longitudinal direction of the initial damage site, while damage propagating along depth considered 0 S/m elements in the transverse direction and along the strut cross-section. A fully damaged strut was simulated by assigning 0 S/m to all elements along the strut cross-section (*i.e.*, the strut is completely broken).

To simulate a multi-defect damage case, an additional full strut length breakage was then introduced in strut 2 by assigning all finite elements within the strut to be 0 S/m. For each undamaged and damaged scenario, the 3D ERT forward problem was executed by applying direct current (DC) between all adjacent electrode pairs (*i.e.*, adjacent current injection pattern) on each z- or 3×3 plane (Figure 4). The complete set of 504 boundary voltages calculated from the forward problem were corrupted with Gaussian white noise signal with a signal-to-noise ratio (SNR) of 66.2 dB, considering the measured SNR is between 65 dB and 68 dB and simulations conducted by Polydorides et al. [91]. The voltage dataset was then used as the input for the ERT inverse solver to reconstruct the 3D conductivity distribution of the lattice structure model.

4.3.2 Sensitivity Discussion

The sensitivity map relates the conductivity perturbation of each finite element to the corresponding variations in boundary electrode voltages. The magnitude of sensitivity is correlated to electric field propagation induced by current injected in a pair of boundary electrodes [73]. In general, the electric field in the center of the target would be much lower than near the boundary, resulting in lower sensitivity in the center. Figure 4.5a plots the summation of the absolute values of sensitivity for each finite element when the lattice structure was interrogated using the adjacent

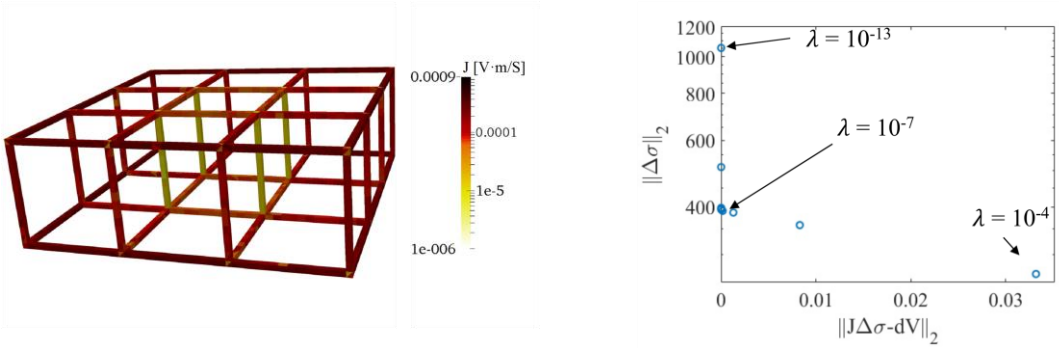

(a) (b)

Figure 4.5: (a) The summed sensitivity map of the lattice structure was calculated. (**b**) The L-curve was plotted, with λ ranging from 10^{-13} to 10^{-4}.

injection pattern (in logarithmic scale). The bright color in the central struts illustrates the decreased sensitivity at the center. Because of the in-plane current injection scheme, the sensitivity of vertical struts along the z-axis is lower than the in-plane struts. The hyperparameter in the inverse problem controls the number of valid SVD components of the sensitivity map. Usually, choosing a smaller hyperparameter will reserve more small SVD components and improve reconstructions of central conductivity changes [58]. However, it is difficult and inefficient to select the appropriate hyperparameter regarding conductivity perturbation happening in different regions of an open cell lattice structure.

Therefore, instead of adjusting the hyperparameter for different conductivity perturbation situations, a normalized sensitivity map was implemented. In accordance with the uniform normalized sensitivity map, the hyperparameter for a uniform conductivity perturbation in the entire region was chosen with the L-curve method for the reconstruction process [58]. In this case, the L-curve with the hyperparameter ranging from 10^{-13} to 10^{-4} is plotted in Figure 4.5b, and 10^{-7} (near the inflection point) was chosen.

4.3.3 Assessment of Conductivity Reconstruction

Classical image evaluation criteria and an additional quantitative criterion were employed to evaluate the conductivity imaging performance of ERT with and without the normalized sensitivity map. It should be clarified that the scope of this chapter only considered damaged struts, so only strut-based errors were evaluated. The image evaluation criteria of position error e_C and area error e_A are calculated as:

$$e_C = \frac{|C_r - C_s|}{L_p} \tag{4.6}$$

$$e_A = \frac{|A_r - A_s|}{A_p} \tag{4.7}$$

where C_s and A_s are the centroid and damage area of the real damaged strut, respectively, while C_r and A_r are the reconstructed damage centroid and damage area, respectively, which are defined by conductivity changes larger than one-fourth of the maximum conductivity change [87,92]. The undamaged strut's length L_p and area A_p are included for normalization. In addition, the reconstructed error value, e_σ, is defined to assess the difference between reconstructed conductivity (σ_r) and the calculated strut representative conductivity (σ_s) normalized by undamaged state conductivity σ_p.

$$e_\sigma = \frac{|\sigma_r - \sigma_s|}{\sigma_p} \tag{4.8}$$

4.3.4 Single-defect Detection

Different damage severities were imposed in the single-defect case, and only the reconstructed conductivity values were affected but not the localization of the defect. Thus, the

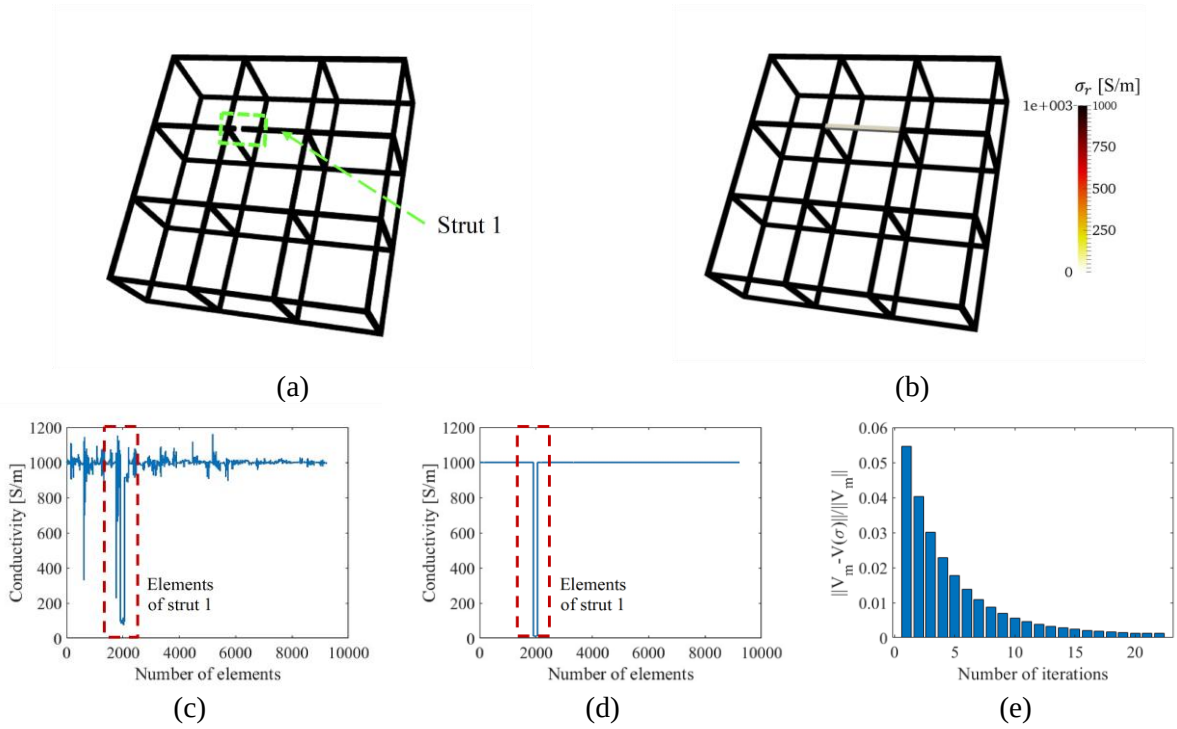

Figure 4.6: (a) A lattice structure was imposed with damage. (b) An ERT reconstruction was solved with the normalized sensitivity map. (c) The reconstructed conductivity values of each element when solved without and (d) with the normalized sensitivity map are plotted. (e) The normalized errors are plotted with iterations.

single-defect case with a fully damaged strut (Figure 4.6a) was investigated and reconstructed by ERT (Figure 4.6b) first. The ERT conductivity distribution of the single-defect lattice structure was reconstructed without and with the normalized sensitivity map; plots of reconstructed conductivity values with respect to the finite elements are shown in Figure 4.6c and 4.6d, respectively. A total of 22 iterations were conducted in the inverse process with the normalized sensitivity map to reach the error ratio tolerance. The decrease of the error ratio is shown in Figure 4.6e. Classical ERT (*i.e.*, without the normalized sensitivity map) could not accurately reconstruct the conductivity value (*i.e.*, 0 S/m) of the central damaged strut but instead could only approach it (*i.e.*, 96 S/m), as is shown in Figure 4.6c. The reconstructed conductivities in the undamaged struts also show significant variations and deviate from the true value of 1,000 S/m. In contrast, Figure 4.6d shows that the reconstructed conductivity values when using ERT with the normalized

Table 4.1: Image errors quantification and comparison of single-defect reconstructions in simulation

Strut-based evaluation	e_C	e_A
Without normalized sensitivity map	0.0030	0.1314
With normalized sensitivity map	0	0

sensitivity map were similar to the actual case (*i.e.*, either 1,000 or 0 S/m). In fact, the corresponding strut-based image errors e_C and e_A are all zeros as shown in Table 4.1. The improved reconstruction performance occurred because normalization compensates for the low central region sensitivity by imposing corresponding weighting factors that facilitated accurate conductivity reconstruction.

As more accurate reconstructed conductivity values were achieved by using ERT with the normalized sensitivity map, the quantitative defect detection ability was further examined with results solved with the normalized sensitivity map. A total of 24 different assumed single-defect cases considered two defect propagation situations were discussed, either along the length or depth of the strut. The first set of 12 damage cases considered a single crack propagating longitudinally in strut 1, where different damage scales (which were defined by damage width and length) were simulated by assigning a conductivity of 0 S/m to n longitudinally adjacent finite elements. The

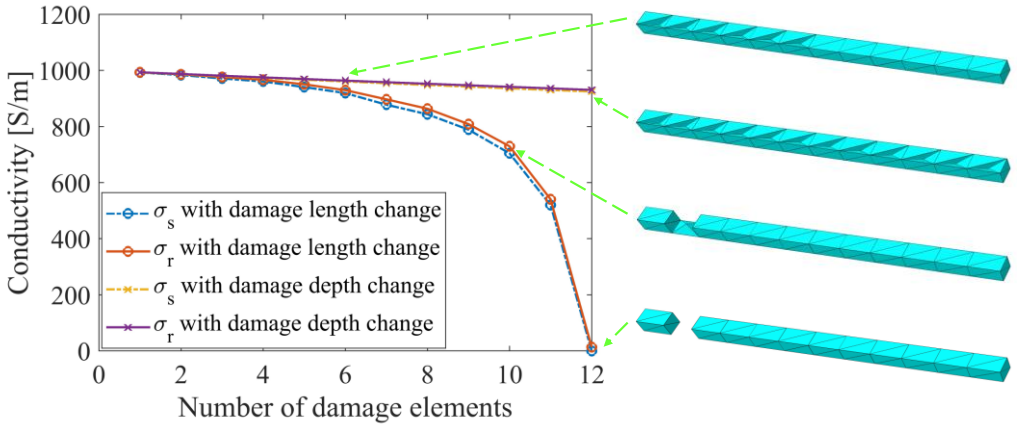

Figure 4.7: Reconstructed conductivity in the strut σ_r is consistent with representative strut conductivity σ_s. Depth and length of the damage feature are varied by assigning 0 S/m to *n* finite elements.

Table 4.2: Reconstructed value errors of single-defect reconstructions in simulation

Damage Scale	e_σ	Damage Scale	e_σ
1	0.0008	**7**	0.0192
2	0.0026	**8**	0.0198
3	0.0052	**9**	0.0198
4	0.0060	**10**	0.0251
5	0.0100	**11**	0.0209
6	0.0105	**12**	0.0137

second set of 12 damage cases were introduced on another undamaged structure, with a defect propagated transversely in strut 1 by imposing 0 S/m on n elements along the strut cross-section. Up to 12 elements were assigned with 0 S/m to simulate a fully damaged strut. In Figure 4.7, the change of the reconstructed conductivity (σ_r) within the damaged strut is consistent with the strut representative conductivity (σ_s) for both imposed damage propagation scenarios. Their consistency expresses the significance of calculating strut representative conductivity and the capability of the ERT method with the normalized sensitivity map to return conductivity values corresponding to the damaged states. The reconstructed errors (e_σ) of the damage cases with defect propagation along depth are shown in Table 4.2. The trends shown in Figure 4.7 demonstrate that the reconstructed values are more sensitive to damage propagated in the transverse direction (as opposed to the longitudinal direction), as suggested by Equation (4.3).

4.3.5 Multi-defect Detection

Multiple defect sites were also considered by introducing an additional full strut breakage to a boundary strut (strut 2), as shown in Figure 4.8a. The ERT result solved without the normalized sensitivity map in Figure 4.8b was littered with artifacts, and e_σ of strut 1 (see Table 4.3) is approximately twice that of strut 2, because strut 2 is closer to the boundary electrodes. In contrast, Figure 4.8c and 4.8d show the reconstructed conductivity distribution in 3D visualization and with

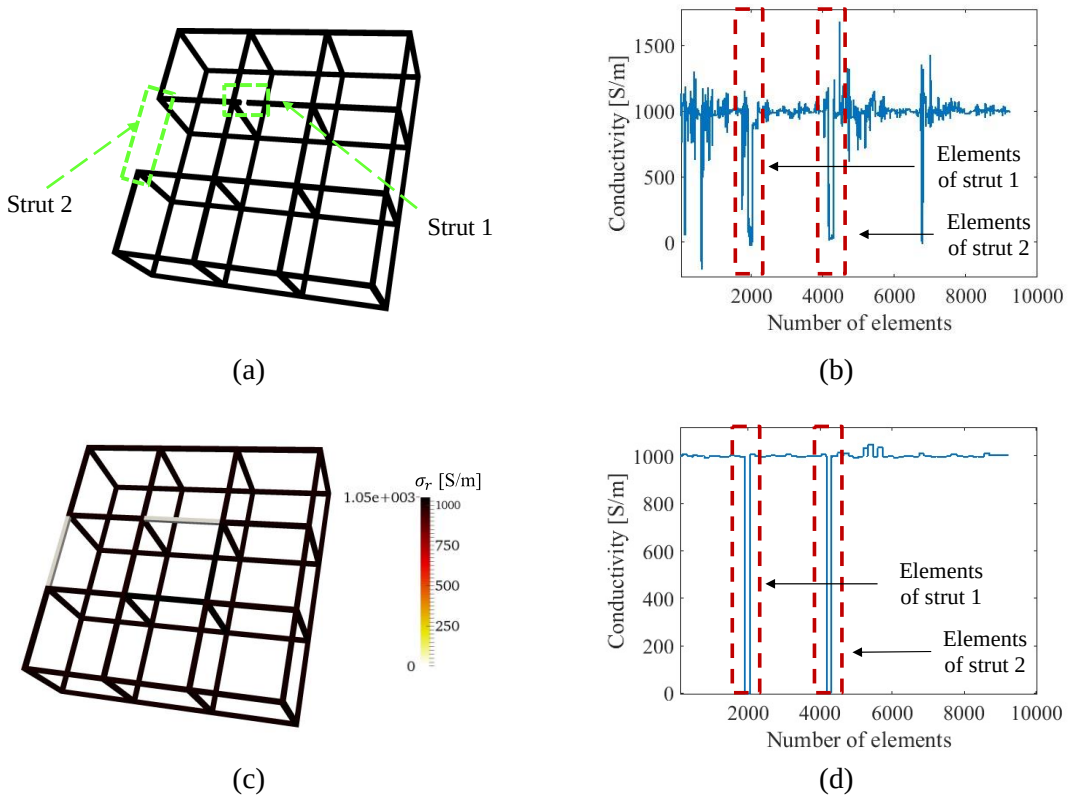

Figure 4.8: (a) A lattice structure with two damaged struts. (b) The reconstructed conductivity values of each element when solved without the normalized sensitivity map. (c) The reconstructed 3D conductivity distribution and (d) the conductivity values for each element, when solved using the normalized sensitivity map.

Table 4.3: Errors quantification and comparison of multi-defect reconstructions in simulation

Strut-based evaluation	e_C	e_A	e_σ **of strut 1**	e_σ **of strut 2**
Without normalized sensitivity map	0.0146	0.1528	0.0752	0.0329
With normalized sensitivity map	0	0	0.0032	0.0017

respect to finite elements, respectively, when using the normalized sensitivity map. In addition to significantly reducing conductivity reconstruction artifacts, normalization yielded uniform sensitivity throughout the cellular lattice structure. The reconstructed conductivity for both damaged struts approaches 0 S/m and can be clearly interpreted as breakages, as can be seen in

Figure 4.8d, and both error values are 20 times lower than the case without normalization. Overall, these simulation results demonstrated improved spatial and quantitative accuracy when the normalized sensitivity map is incorporated with ERT.

4.3.6 Application on Other Lattice Structures

To validate the effectiveness of this method on other lattice structures with different numbers of cells, simulations have been conducted for damage detection in a 3×3×3 lattice and a 4×4×1 lattice with diagonal struts. The 3×3×3 lattice has a total of 24 electrodes distributed on the first and third z-plane boundary intersections, while the 4×4×1 lattice has 32 boundary electrodes. Broken struts were applied on the two lattice structures respectively and the reconstruction results from the ERT solver are shown in Figure 4.9a and 4.9b. The ERT solver still shows excellent performance in detecting the damaged struts in these lattice structures.

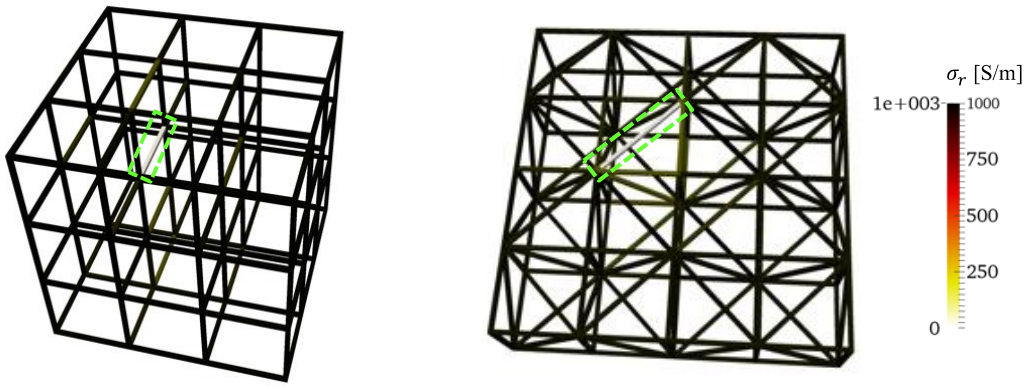

(a) (b)

Figure 4.9: 3D conductivity distribution reconstructions confirmed damage detection performance of the ERT solver in (a) a 3×3×3 lattice structure, and (b) a 4×4×1 lattice structure with diagonal struts.

4.4 Experimental Details and Results

4.4.1 3D-printed Lattice Structures

Experiments were performed on 3D-printed cellular lattice structures to validate damage detection and localization (Figure 4.10a). A commercial fused deposition modeling (FDM) Ultimaker 3+ 3D-printer fabricated 3×3×1 polylactide acid (PLA) lattice structures with cubic unit cells identical to the structure described in Section 4.3.1. The PLA lattice structure was coated with a multi-walled carbon nanotube (MWCNT) thin film. First, a paint primer layer was spray-coated onto the lattice structure. Second, an MWCNT-latex ink was prepared following the procedure described by Mortensen et al. [93] and Wang et al. [94]; MWCNTs were purchased from SouthWest NanoTechnologies. Lastly, upon complete air-drying of the nanocomposite in ambient conditions, 24 boundary electrodes were formed by drying colloidal silver paste (Ted Pella) over conductive threads (Adafruit) at the intersecting boundary nodes, without damaging the structure.

4.4.2 3D ERT Data Acquisition and Testing

The customized 3D ERT data acquisition (DAQ) system employed in this chapter is shown in Figure 4.10b. It consists of a Keysight 34980A multifunctional switch (with an internal digital

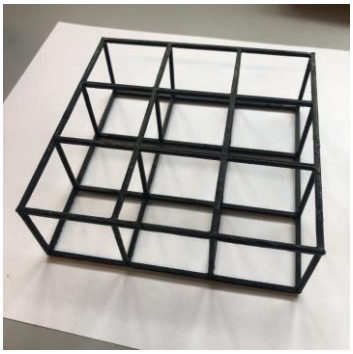

(a)

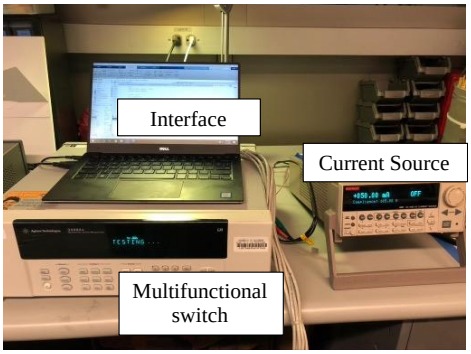

(b)

Figure 4.10: (a) A 3×3×1 lattice structure was spray-coated with a conductive, nanocomposite thin film. (b) ERT measurements were obtained using a customized data acquisition system.

multimeter) and a Keithley 6221 current source, which were connected and controlled by MATLAB. The current source was commanded to inject 10 mA of DC to an adjacent pair of boundary electrodes, while the switch sequentially measured and recorded 504 boundary voltage measurements. The same adjacent electrode method reported in Section 4.3.1 was utilized to inspect the nanocomposite-coated lattice structure.

Three sets of cases were considered: (1) undamaged state, (2) single-defect damaged state, and (3) multi-defect damaged state. First, the undamaged 3D lattice structure was interrogated to reconstruct the undamaged state conductivity distribution of the test specimens. Second, seven different single-defect damage cases (Cases #1 to #7 in Table 4.4) were prepared and tested. Each of these cases featured one damaged internal strut, where damage was introduced by mechanically etching off a portion of the film on the damaged strut. Table 4.4 shows how the single-defect damage cases were unique. The film was removed from one to four of the faces of the square-cross-section strut, while the length of the damage varied between $L/4$ to L, where L is the total length of the strut. In particular, Case #7 corresponded to the case when the film was removed from the entire strut, so the electric current could not flow through the strut (*i.e.*, to emulate complete strut breakage). Lastly, the multi-defect damaged state, Case #8, considered two damaged struts with the nanocomposite completely removed.

Table 4.4: Summary of experimental test cases

	Single-defect							**Multi-defect**
Case	#1	#2	#3	#4	#5	#6	#7	#8
Number of damaged struts	1	1	1	1	1	1	1	3
Number of damaged faces	1	1	1	1	2	3	4	8
Total damaged length	$L/4$	$L/2$	$3L/4$	L	L	L	L	$2L$

4.4.3 Single-defect Detection

Experimental realization of the ERT method depends on the robustness of the experimental data as well as modeling accuracy, where accuracy can be impaired by data with environmental noise and inaccurate modeling. It was hypothesized that the adjusted absolute imaging used in this work could diminish errors by compensating modeling errors with local minimization. An example of a direct comparison between simulated and experimentally measured boundary voltages is shown in Figure 4.11a and confirms the degree of mismatch was minor.

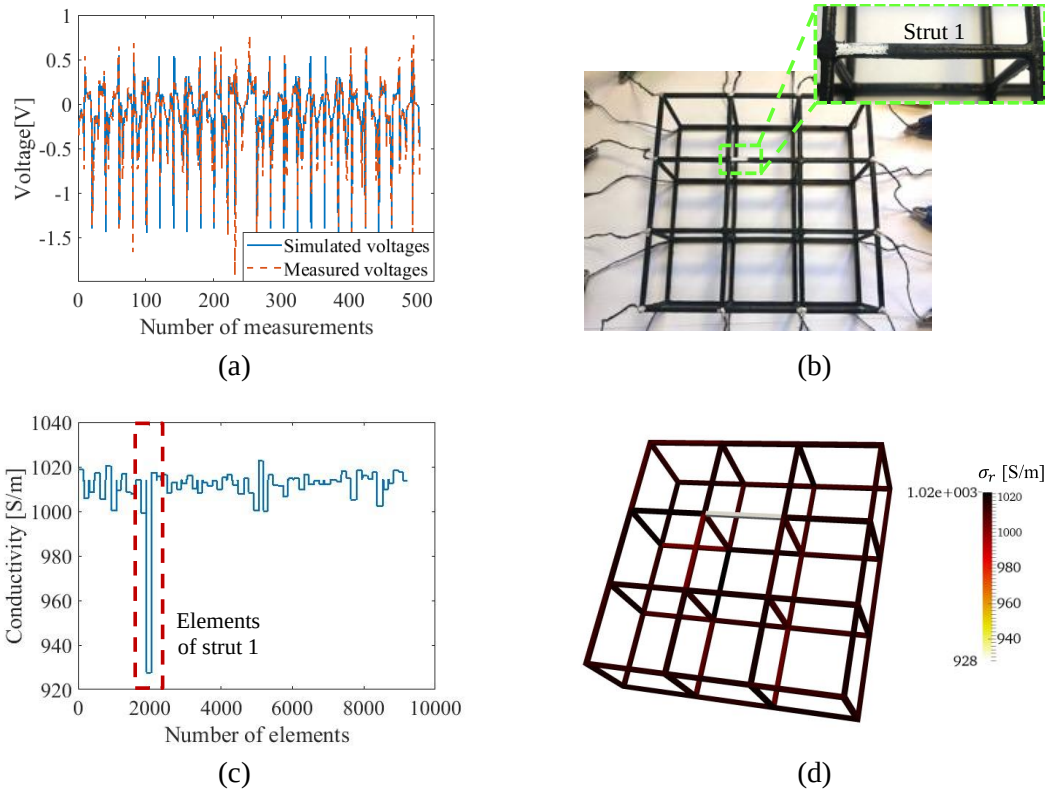

Figure 4.11: (a) Simulated voltages are compared with experimentally measured voltages. (b) The first etch (damage) was introduced in the lattice. (c) The reconstructed conductivity values of each element when solved with the normalized sensitivity map are plotted. (d) The corresponding 3D conductivity distribution successfully confirmed damage detection in strut 1.

Table 4.5: Image errors comparison of single-defect reconstructions in experiment

Strut-based evaluation	e_C	e_A
Without normalized sensitivity map	0.0696	0.1551
With normalized sensitivity map	0	0

The defect detection performance of the ERT system with the normalized sensitivity map was examined with experimental measurements in Case #1. The picture of Figure 4.11b shows that the film was etched off on the upper side of strut 1 with a total etched length of $L/4$. From the results obtained from 36 iterations in the inverse process and evaluations shown in Figure 4.11c and Table 4.5, artifacts were restrained to some extent with the application of the normalized sensitivity map. These minor conductivity artifacts were the result of experimental measurement noise and modeling inaccuracies of modeling. The reconstructed value of 928 S/m in strut 1 is related to the size of the etch and will be discussed more in the quantitative study. The reconstructed conductivity distribution of the lattice structure with a single damaged strut is visualized in Figure 4.11d.

The quantitative damage detection performance of ERT was evaluated with experimental measurements in the single-defect damaged state, from Cases #1 to #7. Although only conductive nanocomposites were coated onto PLA lattice structures, the ERT FE model still considered solid struts, because the modeling inaccuracy of strut cross-sections is admissible due to the strut-wise defect detection capability of ERT on lattice structures. This meant that actual damage, such as film etched off a single face, was modeled as a one-fourth cross-section reduction. Thus, Case #1 was assumed to have experienced a volume reduction of one-fourth A_0 and one-fourth L, as illustrated in Figure 4.12a. The reconstructed image and value were then evaluated with the

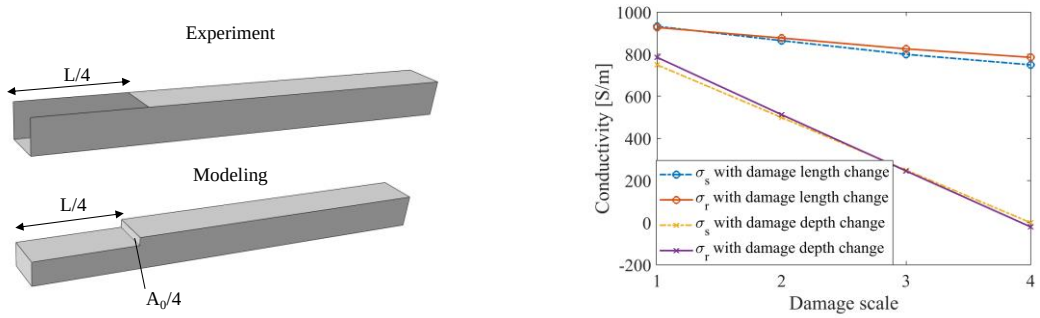

(a) (b)

Figure 4.12: (a) The actual experimental damage (Case #1) was compared to what was modeled. (b) Representative strut conductivity σ_s and reconstructed conductivity in the strut σ_r change in tandem as damage increased in severity, both along its length and depth (cross-section).

representative model and strut representative conductivity (σ_s), which was calculated using Equations (4.4) and (4.5).

The conductivity results of Cases #1 to #7 (with etches of different sizes along the length and different faces) were reconstructed using ERT with the normalized sensitivity map. Among these, Cases #1 to #4 considered damage occurring on a single face but increased in length from $L/4$ to L (*i.e.*, similar to damage propagating along the length of the strut). Cases #5 to #7 corresponded to damage growing in depth. The comparison between reconstructed conductivities solved with the normalized sensitivity map and the strut representative conductivities is presented in Figure 4.12b, while the calculated errors listed in Table 4.6 show their consistency. From Figure 4.12b, it can be seen that damage along the cross-section of the strut can be detected at a higher sensitivity than those along the length. Overall, the similarity between the reconstructed and strut representative conductivity results experimentally validated the proposed ERT method.

Table 4.6: Reconstructed value errors of single-defect reconstructions in experiment

Damage Case	**#1**	**#2**	**#3**	**#4**	**#5**	**#6**	**#7**
$\boldsymbol{e_\sigma}$	0.0053	0.0199	0.0257	0.0353	0.0134	0.0042	0.0244

4.4.4 Multi-defect Detection

In addition to the single-defect scenarios (*i.e.*, Cases #1 to #7), Case #8 with an additional broken strut (*i.e.*, strut 2) was considered. The conductivities of each element reconstructed using ERT with the normalized sensitivity map are plotted in Figure 4.13a. Similar to the previous results, damage in the broken struts could be identified, and the conductivity values approached 0 S/m. Artifacts were present in other elements, but their magnitudes are at least 83% lower than those corresponding to the two broken struts, which are also evident based on the calculated error values listed in Table 4.7. Because these correspond to experimental results, artifacts due to measurement noise and mismatch between simulation modeling and experiment are inevitable. Nevertheless, the

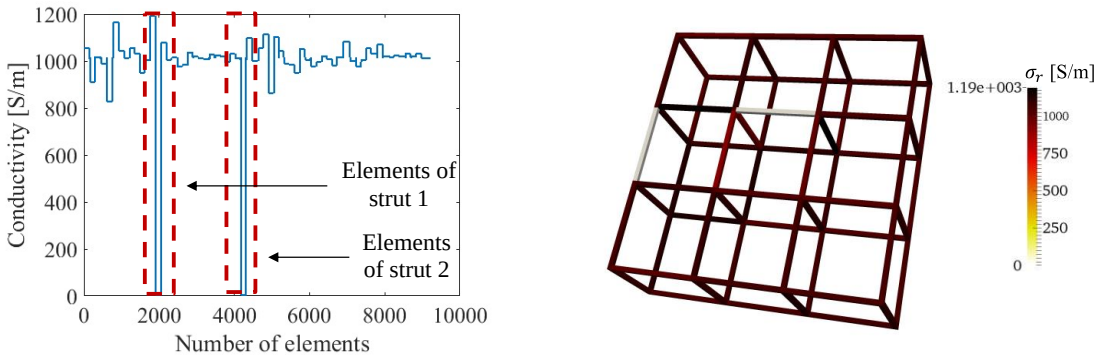

(a) (b)

Figure 4.13: (a) The reconstructed conductivity values of each element when solved with the normalized sensitivity map are plotted. (b) The corresponding 3D conductivity distribution of the lattice structure successfully identified broken struts in strut 1 and strut 2.

Table 4.7: Errors quantification and comparison of multi-defect reconstructions in experiment

Strut-based evaluation	e_C	e_A	e_σ **of strut 1**	e_σ **of strut 1**
Without normalized sensitivity map	0.0287	0.2233	0.0653	0.0804
With normalized sensitivity map	0	0	0.0056	0.0030

values of e_σ in Table 4.7 clearly show that ERT with the normalized sensitivity map outperforms classical ERT.

4.5 Results and Discussion

The simulation and experimental results showed that the 3D ERT method with the strut-based normalized sensitivity map was able to quantitatively characterize damage in cellular lattice structures. The strut-based normalized sensitivity map compensated for the low central sensitivity and diminished image artifacts, so the reconstructions had much smaller reconstruction errors in $\boldsymbol{e_C}$, $\boldsymbol{e_A}$, and $\boldsymbol{e_\sigma}$.

The implementation of the ERT method in practice may meet problems as many electrodes need to be attached for to the structure the contact-based ERT inspection. Improper manual attachment of electrodes on structures in service or measuring voltage in very high- or low-temperature environments would result in unexpected measurement noise or voltage raises or drops respectively. Inaccurate measurements may further influence the reconstruction process, hence poor damage detection performance. To solve this problem, modularized press contact electrodes with covers could be utilized, which could avoid extreme temperatures and could be assembled together to adapt to different structures. Also, electrodes numbers could be reduced to meet the minimum requirement after investigating the optimized electrode configuration in the future.

Overall, the 3D ERT method is an efficient method for detecting damage in lattice structures. With only a few electrodes attached to the boundary and their corresponding voltage measurements, the resistivity distribution that correlated to the damaged state could be captured. Currently, vibrational-based methods could only offer classification of different damage scenarios

but could not effectively pinpoint specific damaged struts unlike the 3D ERT method [95]. Moreover, ERT utilizes the intrinsic electromechanical properties of lattice structures and renders effective inspection by propagating current throughout the entire structure. Furthermore, X-ray CT-based measurements or other image processing methods require the structure to be placed between a source and detector while being rotated to obtain multiple projection slices, which requires extensive operational times and computational resources [96].

4.6 ERT and Machine Learning for Lattice Structures Damage Detection

This section investigated 3D ERT with deep ANN method as an efficient and practical NDE method for localizing defects in complex lattice structures. Traditional model-based approaches for solving the ERT inverse problem are time-consuming and computationally intensive [58,69], even though they have been successfully used in patterned, grid-like structures similar to cellular lattices [76,97]. Data-driven methods that could potentially output conductivity distributions in near-real-time would be more suitable for detecting damage in complex structural geometries (e.g., cellular lattice structures) and for use in high throughput manufacturing settings. The data-driven algorithm is significantly faster than conventional ERT while enabling greater accuracy of 3D conductivity distribution reconstructions. Experimental results are presented in this work to validate this machine-learning-based ERT solver.

4.6.1 ERT-ANN System

To effectively apply the ERT-ANN system to the structure, the model was further meshed in Abaqus with 3440 tetrahedral finte elements. The conductivity of the undamaged structure was uniformly set as 1000 S/m. This numerical model was used to solve the ERT forward problem to

determine the boundary voltage responses corresponding to different current injection schemes. These datasets were then used for training the deep ANN system.

The ERT-ANN system consisted of two sets of deep ANN structures, namely, deep ANN I and deep ANN II, was developed. Deep ANN I was used to identify the damaged strut (i.e., with a decrease in conductivity) within the cellular lattice structure. It utilizes information from 504 boundary voltage measurements to estimate the centroid of the damaged strut *j*. After identifying the damaged strut *j*, the second deep ANN II-*j*, which corresponds to the damaged strut *j*, was used to localize the exact damage within that strut. In this section, only single damage cases were considered.

Training of deep ANN I entailed preparing datasets for an undamaged case and 5000 damaged cases for the 3×3×1 cellular lattice structure shown in Figure 1a. Damage to the strut was simulated by modeling the conductivity of a randomly selected finite element of the structure and setting it to 0 S/m. For each case, the ERT forward problem was solved to obtain the boundary voltage response associated with a current injection scheme. They were then corrupted with Gaussian white noise with 66.2 dB signal-to-noise ratio (SNR). The normalized voltage difference (dV_n) between each damaged state and the undamaged state was calculated as:

$$\delta V_n = \frac{V^d - V^0}{v} \tag{4.9}$$

where v is the maximum absolute measurement on the undamaged structure, V^d and V^0 represent voltages in the damaged state and the undamaged state respectively. Because deep ANN I only focuses on detecting the damaged strut instead of the exact damage location, SVD could be used on δV_n for input dimensionality reduction [98]. Here, the dimension of the input depends on the

number of singular values included when the ratio of variance reaches a 0.995 accuracy, and a total of 72 encoded inputs δV_n^{svd} were utilized in deep ANN I. The output of deep ANN I is the centroidal coordinates of the damaged strut.

The second structure (deep ANN II) includes multiple deep ANN structures, where deep ANN II-*j* could provide the location of the single defect within strut *j*, and *j* starts from 1 to the total number of struts (*N*) in the lattice structure. To train deep ANN II-*j*, 500 damaged cases, each with a unique and randomly selected single finite element defect of 0 S/m within strut *j*, were generated. The ERT forward problem was solved for each damage case (i.e., considering the entire lattice structure). Considering that all these damaged states are from the same strut *j*, the calculated boundary responses would be similar. Thus, SVD could also be used on δV_n for a more efficient input dimensionality reduction [98]. A total of 18 encoded inputs δV_n^{svd} from SVD were selected to represent the 504 boundary voltages when strut *j* is damaged. The output of deep ANN II-*j* is the centroid of the defect element *k* within strut *j*.

The deep ANN architectures for deep ANN I and deep ANN II-*j* used in this section are illustrated in Figure 4.14a and 4.14b. With the encoded normalized voltage difference as input,

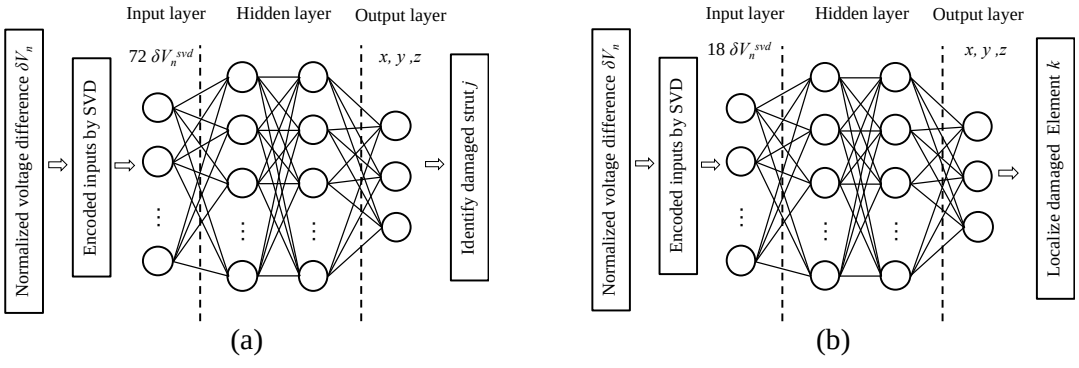

Figure 4.14: (a) The architectures of deep ANN I and (b) deep ANN II-j are illustrated.

four fully connected hidden layers with 2048 neurons in each layer were employed. For each neuron in the hidden layer, an exponential linear unit was implemented.

4.6.2 Experimental Details and Results

To validate the performance of the ERT-ANN system, experiments were conducted on 3D-printed PLA lattice structures coated with an electrically conductive MWCNT-based thin film [99]. Two different damage states (i.e., states 1 and 2) were investigated as shown in Figures 4.15a and 4.15b. Damage states 1 and 2 were introduced to the structure by mechanically etching off the conductive MWCNT thin film at portions of strut 1 or strut 2, respectively.

The effectiveness of deep ANN I on localizing the damaged strut was examined first. The calculated normalized voltage differences (δV_n) between undamaged and damaged states were

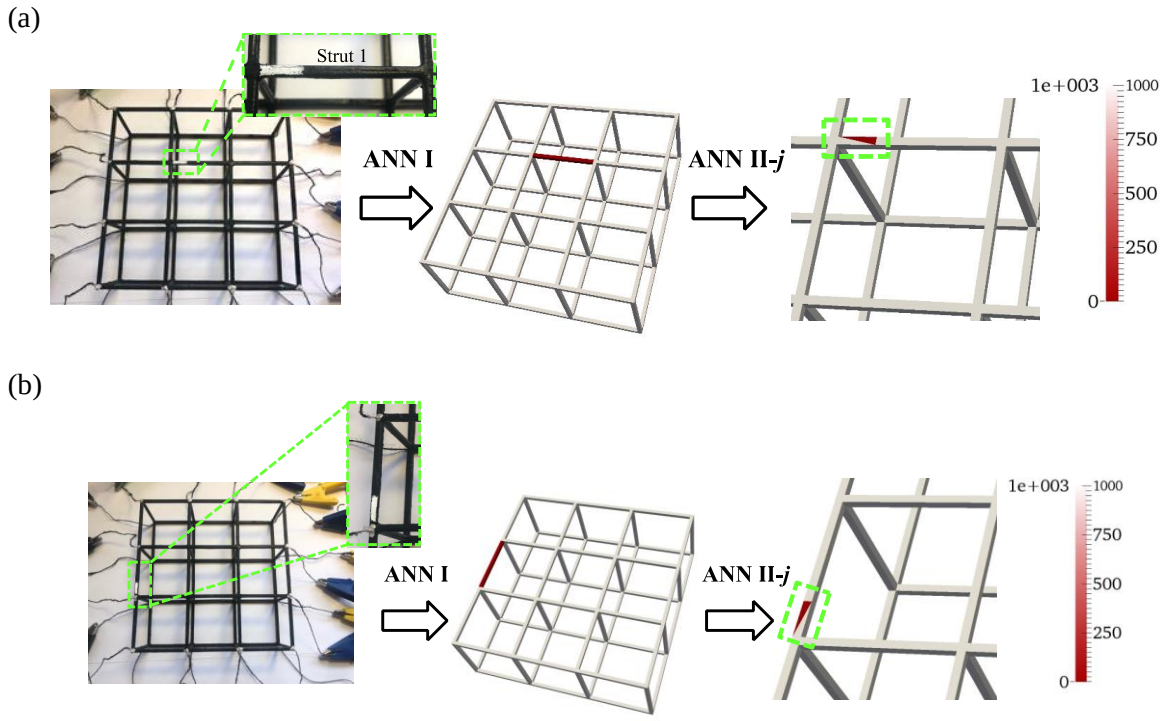

Figure 4.15: Experimental results and the visualization of (a) damage state 1 and (b) state 2 solved with the ERT-ANN system.

processed with SVD and employed in deep ANN I as inputs. The predicted locations of the strut centroids, *x*, *y*, and *z* were stated with the true centroids of damaged struts in Table 4.8. The image position errors1 for the two states are 0.1702 and 0.0683, respectively [23]. The predicted values were then employed in the k-nearest neighbors algorithm to find the damaged strut in the two cases. The middle figures in Figures 4.15a and 4.15b confirmed that deep ANN-I was able to correctly identify the damaged strut in the lattice structure for both damage states.

Then, deep ANN II-*1* and deep ANN II-*2* corresponding to strut 1 and strut 2 were then employed to estimate the specific damage locations within each respective strut. The true and the predicted *x*, *y*, and *z* of centroids for each state were stated in Table 4.8, and the image position errors for the two states are 0.0276 and 0.0413. The result visualizations are shown in the right-hand-side images in Figures 4.15a and 4.15b. The results show that deep ANN II-*j* was able to correctly identify the portion of the strut where the damage occurred. Only small deviations between the actual and predicted locations were observed. Similar to before, the predicted centroids could be fed into the k-nearest neighbors algorithm to obtain the *x*, *y*, and *z* coordinates for the damaged element. The precision of the deep ANN systems is constrained by the discretized finite element. Overall, these test results validated the damage localization performance of the ERT-ANN system for topologically ordered lattice structures with low image errors.

Table 4.8: The true and predicted centroids from ANN I and ANN II in damage state 1 and state 2

		Deep ANN I			Deep ANN II		
		x [mm]	y [mm]	z [mm]	x [mm]	y [mm]	z [mm]
State 1	True	39.00	57.00	19.00	38.76	44.57	19.73
	Predicted	44.30	61.25	19.46	39.02	45.62	19.51
State 2	True	58.00	0.00	19.00	70.61	-0.31	19.80
	Predicted	56.60	2.27	19.60	69.55	-0.20	21.06

4.7 Conclusions

This chapter demonstrated an absolute, high-performance, 3D ERT method which incorporates a strut-based normalized sensitivity map for quantitative defect detection in lattice structures with high image accuracy. The approach was applied for detecting multiple defects in open-cell lattice structures. The strut-based normalized sensitivity map addressed the issue of heterogeneous damage sensitivity, particularly lower sensitivity away from the boundaries where measurements are obtained. Simulations and experiments validated the improved defect detection capability of this method compared to classic ERT. In simulations, single- and multi-defect cases were realized by assigning 0 S/m to finite elements while the damage in experiments was realized by etching coated conductive nanocomposite thin films. Our results show that the ERT method with the normalized sensitivity map could localize defects more accurately and with smaller image errors compared to classical ERT. Quantitative damage detection performance was demonstrated by the strong consistency between reconstructed conductivity within a strut and the actual damage severity. Future work will examine the development of an electrical impedance tomography system to leverage alternating current input excitations for higher resolution defect imaging, and non-iterative reconstruction algorithms that not requiring a baseline measurement for high-speed anomalies detection instead of high-accurate conductivity reconstructions.

Moreover, an ERT-ANN system was proposed for detecting and localizing defects, such as broken or partially damaged struts, in topologically ordered conductive lattice structures. Specifically, the ERT-ANN system consisted of two ANN structures. Deep ANN-I was used to identify the damaged strut, while deep ANN-II further determined where the damage occurred within the strut. The method was trained using numerically simulated data (i.e., by considering different damage cases and calculating the boundary voltage responses using the ERT forward

problem). Upon training, experiments were performed using a conductive thin-film-coated lattice structure, where damage was introduced by etching off portions of the film in different struts. The ERT-ANN system was able to correctly locate the damaged struts and accurately identified the portion of each strut that was damaged. Overall, the data-driven ERT method could utilize boundary voltages to reconstruct the conductivity distribution of complex 3D lattice structures and detect conductivity decreases due to damage such as strut breakages, voids, or manufacturing defects. Future studies will consider different damage severities as well as more complex distributed damage scenarios.

Acknowledgement

Chapter 4 is in full, a reprint of the materials as in appears in "Multi-Defect Detection in Additively Manufactured Lattice Structures Using 3D Electrical Resistance Tomography." Shu, Yening, Saptarshi Mukherjee, Tammy Chang, Abigail Gilmore, Joseph W. Tringe, David M. Stobbe, and Kenneth J. Loh, *Sensors* 22.23 (2022), and "Electrical Resistance Tomography and Machine Learning for Lattice Structure Damage Detection." Shu, Yening, and Kenneth J. Loh, *Measurement Science and Technology* (2023). The dissertation author was the primary investigator and author of this material.

CHAPTER 5 BASELINE FREE COMPLEX CONDUCTIVITY MAPPING FOR SPATIAL DAMAGE SENSING USING NANOCOMPOSITE AND EIT

5.1 Introduction

Damage and degradation in civil, aerospace, mechanical, naval, and automotive engineering structures are unavoidable, especially since they are exposed to various environmental conditions, repeated loads, extreme events, and unexpected forces [36,44,100]. For instance, cracks and overstrains are easily generated because of internal stresses caused by temperature changes or structural swelling from the moisture absorption [100]. Especially, surface cracks may easily expedite the moisture and chemical absorption in structures, which result in loss of structural strength and stiffness, hence influencing structural mechanical behavior and integrity [100,101]. Therefore, condition assessments are profoundly needed to discern the surface cracks and overstrain in the early stage to prevent damage propagation and the subsequent reduction of structural load-carrying capacities.

Paints or coatings that are usually deposited on the surface of aircraft, automotive, and civil structures could be upgraded to multifunctional and smart paints, which could directly serve as a sensing layer for monitoring damage and overstrains. Therefore, instead of using SHM methods by introducing additional devices afterward, direct employment of multifunctional structures with intrinsic self-sensing capability or coupled sensing coats would be the most cost- and resource-efficient. Recently, the advent of nanotechnology has enabled the development of nanocomposite coats as multifunctional skin sensors [102]. Among a variety of nanomaterials, CNT has attracted significant attention because of its unique mechanical and electrical properties and wide applications. For instance, Loyola et al. [57] developed a CNT-based thin film that could be spray-deposited on the surface of unlimited size for strain and damage sensing. Zhao et al. [79] applied

inkjet-printed CNT-based thin film to perform spatial strain sensing and studied the strain sensitivity by characterizing the piezoresistive matrix. Dai et al. [103] fabricated a nanocomposite strain sensor by coating CNT onto a nonwoven carrier fabric, which is mechanically robust and linearly piezoresistive. Except for depositing extra sensing layers on the surface, Li et al. [75] has successfully fabricated multifunctional CNT-based nanocomposite paint as a strain-sensitive sensor which could not only serve as a sensing layer but also as protection.

To obtain spatial mechanical information from multifunctional skin sensors, EIT which utilizes the coupled electrical and mechanical properties of the skin sensors is extensively employed [67,75,79]. The impedance reconstructions directly reflect structural strain and damage states as the electrical impedance of those sensing skins is directly related to their mechanical fields. However, the absolute impedance reconstruction has limited accuracy because of possible modeling errors and environmental noises [67]. Time difference EIT (tdEIT) which requires measurements before and after damage could offer a more reliable estimation of the change of impedance distribution due to the damage, but the acquisition of measurements of the undamaged structure is not always achievable in practice [67]. Thus, fdEIT which reconstructs the image using measurements from two different electric current injecting frequencies is a good candidate to inspect structural mechanical states in arbitrary time steps [70,104].

In this chapter, a nanocomposite paint was fabricated to serve as a spatial strain sensor. A commercially available vinyl-based paint was used as the matrix material to design the MWCNT-based nanocomposite paint. The variation of electrical properties versus frequency in unstrained and strained states was characterized. The variation of electrical properties in different injecting frequencies enables the application of fdEIT methods. However, since the damaged area is always circumvented by the impedance perturbation of MWCNT-based paint background from different

injecting frequencies, the image for the damaged region is easily reconstructed with artifacts [70]. To increase the reconstruction accuracy, Baltopoulos et al. [58] proposed to choose the optimal hyperparameter with the L-curve method regarding different perturbations, but the preprocessing is too time-consuming. Therefore, data-driven methods that could potentially output impedance distributions in near-real-time with high accuracy would be more suitable.

Data-driven deep ANN techniques have garnered significant attention because of their adaptability for modeling nonlinear processes. Deep ANN architectures that possess multiple layers with numerous neurons could be efficiently adapted to solve EIT problems with inherent nonlinearity. As compared to a physics-based EIT approach with one-step linearization, a deep ANN could reconstruct a target's impedance distribution with higher accuracy, especially when considering the nonlinear nature of conventional EIT. Li et al. [105] and Quqa et al. [66] employed data-driven ANN methods to solve the EIT problem, and validate the better performance of deep ANN versus the traditional total variation method.

This chapter employed the deep ANN method in the fdEIT process, on a smart MWCNT-based paint with frequency-dependent electrical impedance. The process of classical fdEIT and deep ANN based fdEIT are stated in Sections 5.3.1 and 5.3.2, and simulations and experiments were conducted to validate the performance of this method.

5.2 Material

The objective of this chapter was to improve the fdEIT process with the deep ANN method while incorporating nanocomposite sensing paint to enhance surface damage detection. In this section, the fabrication and characterization of the nanocomposite paint were discussed. First, the

fabrication procedure of the MWCNT-based paint was stated. Second, long-strip samples were fabricated and the frequency-dependent piezoresistive properties were characterized.

5.2.1 Nanocomposite fabrication

To fabricate the MWCNT-based smart paint, a commercially available Pro-Line vinyl copper antifouling paint and Pro-Line vinyl paint thinner from Sherwin-Williams (Garland, TX, USA) were used as the matrix in this study. Also, to create the piezoresistive property of the smart paint, the conductive MWCNT and carbon black (CB) SC159 purchased from NanoIntegris (Boisbriand, QC, Canada) and Tokai Carbon CB (Fort Worth, TX, USA) respectively were added into the formulation.

First, the nanocomposite mixture was produced with 0.74 wt.% MWCNT, 0.37 wt.% CB and 61.89 wt.% of vinyl paint thinner. The addition of CB in the nanocomposite mixture would enhance the sensor strain sensitivity and linearity [75]. In order to disperse MWCNT and CB more uniformly, the mixture was subjected to bath sonication for 90 min. Then, 37 wt.% of vinyl paint

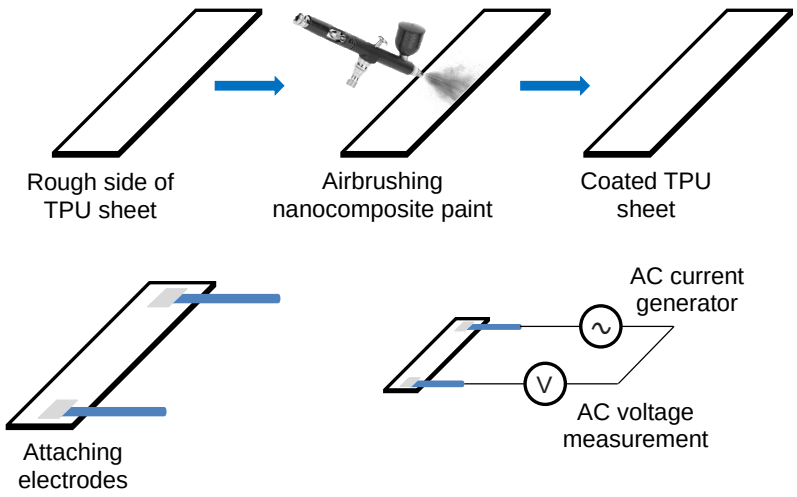

Figure 5.1: The spray-coating and characterization process of the nanocomposite paint is illustrated.

was added to the sonicated mixture and shear-mixed for 20 min at 800 rpm. The final piezoresistive nanocomposite paint was eventually ready to be sprayed. Spray-coating was then manually performed using a Paasche airbrush onto the rough side of the thermoplastic polyurethane (TPU) sheet substrate which was provided by Wiman Corporation (Sauk Rapids, MN, USA), as illustrated in Figure 5.1. Lastly, after 12 h air-drying of the nanocomposite in ambient condition, electrodes were attached on the boundary of specimens for following measurements. For the formation of electrodes, conductive threads were purchased from Adafruit, solder wire was from Voltera (Kitchener, ON, Canada), drying colloidal silver paste was from Ted Pella (Redding, CA, USA), and two-part silver epoxy was from MG Chemicals (Surrey, BC, Canada).

5.2.2 Frequency-dependent Piezoresistivity

The frequency-dependent impedance was measured while AC currents were injected with different frequencies. Long-strip specimens were formed by spraying nanocomposite paint on 5×70 mm^2 TPU sheets and then affixed to a 3D-printer fabricated dog bone-shaped PLA coupon. Voltera solder wires were soldered on the copper tape and then connected to the end of specimens

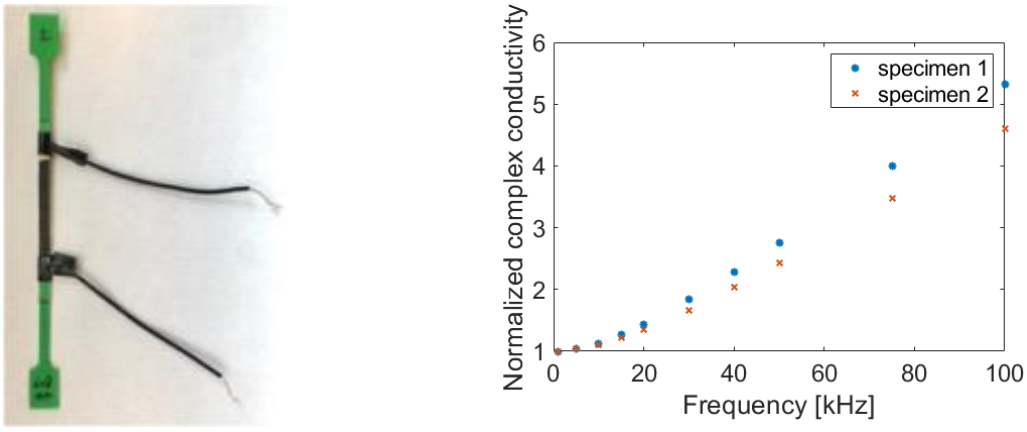

(a) (b)

Figure 5.2: (a) The nanocomposite paint was sprayed on a TPU sheet and affixed to a PLA coupon. (b) The relation between the complex conductivity of the nanocomposite paint and current injecting frequency is plotted.

with fast-drying colloidal silver paste as shown in Figure 5.2a. In the unstrained state, specimens were first connected to a Keithley 6221 current source and a Keysight 34450A digital multimeters (DMM), as illustrated in Figure 5.1, to obtain complex conductivity (γ) in different injecting frequencies from 1 kHz to 100 kHz. In Figure 5.2b, the normalized complex conductivity continuously increases when the current injecting frequency increases. The complex conductivity at 100 kHz is around five times of complex conductivity at 1 kHz. The difference of complex conductivity in different frequencies enables the application of the fdEIT method.

Then, the coupon was subjected to cyclic tensile loads with 0.08 mm peak displacement in the Test Resources 150R load frame. Meanwhile, the AC voltages were continuously measured by the digital multimeter while an AC current was flowing through the specimen. Because the AC voltage measurements were easily unstable when the excitation frequency is high, only 1 kHz – 50 kHz excitations were employed. The related study discussed by Li et al. [75] about resistance change of the smart paint under the cyclic tensile loads and its strain sensing sensitivity will not be included in this section. Instead, the average maximum impedance changes (under 0.08 mm peak displacement) during the five load cycles were recorded. The maximum normalized impedance change (ΔZ_n) at each excitation frequency was calculated by dividing the impedance change between the maximum strained state (Z_m) and the unloaded state (Z_0) by Z_0:

$$\Delta Z_n = \frac{Z_m - Z_0}{Z_0} \tag{5.1}$$

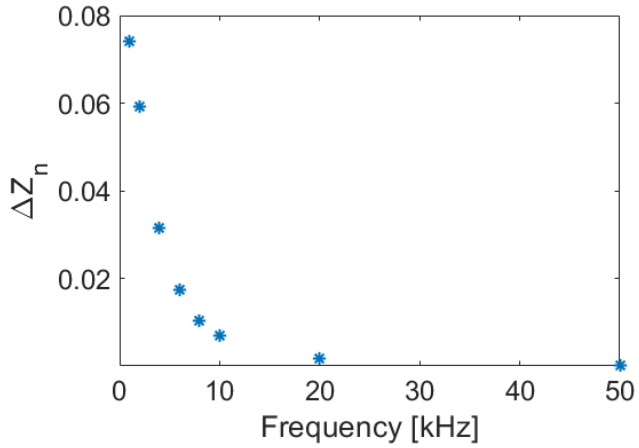

Figure 5.3: The maximum normalized impedance change under 0.08 mm tensile displacement is decreasing with the increase of injecting frequency.

As shown in Figure 5.3, ΔZ_n decreases when the injecting frequency increases. The maximum normalized impedance change is almost 0 when the frequency is 50 kHz, which represents the strain sensing sensitivity of the nanocomposite paint in 50 kHz excitation is very low. The strain-sensing property of the paint is nearly decreasing linearly when the excitation frequency is smaller than 8 kHz. With the frequency-dependent piezoresistivity, under different frequencies, the region under tensile strain will have a larger impedance difference and also a larger complex conductivity difference than the unstrained region. The properties could be utilized in the fdEIT processing to localize the strained region.

5.3 Classical fdEIT and fdEIT-ANN System

5.3.1 Classical fdEIT Solver

In this chapter, fdEIT with difference imaging was employed for complex conductivity distribution reconstruction. In the forward problem, the complete set of boundary voltages (V_ω^i) (i.e., for Ω with an assumed complex conductivity distribution (γ_ω^i) corresponding to an i^{th} condition) is obtained by injecting current with frequency ω across different unique pairs of

boundary electrodes. The adjacent, opposite, or diagonal current injection pattern can all be used to interrogate Ω, but only the adjacent current injection pattern was utilized in this chapter. It should be mentioned that the fdEIT forward problem can be used to solve for boundary voltages, $V_{\omega a}{}^{i}$ and $V_{\omega b}{}^{i}$, which correspond to i^{th} damaged state with different current injecting frequencies ω_a and ω_b. Because the complex conductivity in the damage region is always 0 S/m while the complex conductivity of the nanocomposite paint is changing with excitation frequency, the different distribution $\gamma_{\omega a}{}^{i}$ and $\gamma_{\omega b}{}^{i}$ are measured when currents with different frequencies are injected respectively. The change in conductivity distribution between those two states ($\delta\gamma$) can also be used to solve for the corresponding boundary voltage difference, δV [52,54].

For the inverse problem, difference imaging was employed in this chapter, and the conductivity change ($\delta\gamma$) between two states could be estimated with least-squares (LSQ) as Equation (2.35). Except for difference imaging, weighted difference imaging is also widely applied in fdEIT on medical imaging to remove background perturbations [70,104]. However, the method is not suitable for this chapter because the complex conductivity in the damage region is always 0 S/m, so the difference in complex conductivity distribution in the paint background would not be included in the weighted difference.

In this chapter, with a high excitation frequency ω_b and then a low excitation frequency ω_a, the nanocomposite paint will have a large complex conductivity $\gamma_{\omega b}$ and then a small complex conductivity $\gamma_{\omega a}$ while the γ_{ω} of the damage region remains 0 S/m. The $\delta\gamma$ in the nanocomposite paint region between these two injecting frequencies is positive while $\delta\gamma$ in the damage region is 0 S/m, therefore, localized low conductivity could be used for directly visualizing damage locations.

5.3.2 *The fdEIT-ANN System*

Here, an fdEIT-ANN system was leveraged to reconstruct complex conductivity distribution in the nanocomposite region and then detect the damage locations. The structure investigated in this chapter is a 50×50 mm^2 square-shaped nanocomposite thin film with 16 electrodes equidistantly attached on the boundary, as shown in Figure 5.4.

In the fdEIT-ANN system, the complex conductivity change ($\delta\gamma$) and corresponding voltages change (δV) obtained from the fdEIT forward problem would be utilized in the deep ANN structure for the training process. The trained deep ANN then could be used to identify the region with low conductivity as the damage location with the input of normalized boundary voltages change. To solve the fdEIT forward problem, a model with the same dimensionalities was constructed in Abaqus with a total of 1250 triangle meshed elements. The deep ANN system utilized 208 normalized boundary voltage differences as the input layer to calculate the normalized complex conductivity change in 1250 elements as the output layer.

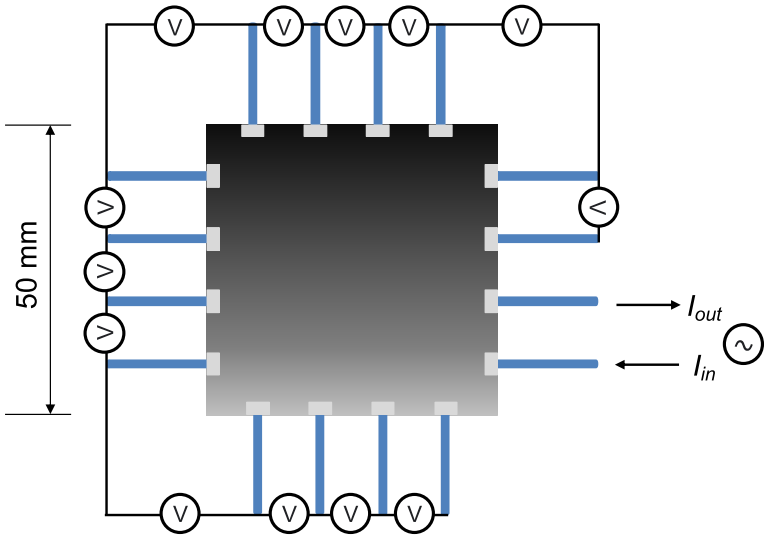

Figure 5.4: A schematic figure of a nanocomposite paint thin film with 16 boundary electrodes under EIT testing is illustrated. The EIT DAQ system injects electrical current across a pair of adjacent electrodes, while voltages are measured at all other remaining boundary electrodes.

To prepare the training sets for the ANN structure, 3000 damaged cases of the square nanocomposite paint thin film with random were generated. Randomly propagated damage in the thin film was modeled by setting γ of finite elements in the damaged region to 0 S/m. The maximum damage element number was set as 200 in this study. The complex conductivity of other finite elements was set to 11.83 S/m and 58.35 S/m respectively, corresponding to the values of nanocomposite paint in 1 kHz and 100 kHz excitation that characterized in experiments. So, a total of 6000 complex conductivity distribution states were examined with the forward problem solver to calculate the boundary voltages. The boundary voltages were then added with white Gaussian noise of 66.2 dB signal to noise ratio (SNR) considering the experimentally measured SNR is between 65 dB and 68 dB. The normalized difference ($\delta V_n{}^i$) of simulated voltages in i^{th} damage case between 100 kHz and 1kHz excitaition is calculated as:

$$\delta V_n^i = \frac{V_{100k}^i - V_{1k}^i}{V} \tag{5.2}$$

where V is the maximum absolute voltage during 1 kHz excitation. The $\delta V_n{}^i$ serves as the input. Also, the differences of complex conductivity distributions between 100 kHz and 1 kHz excitation were noramlized as $\delta\gamma_n$ before put in the output layer.

The deep ANN architecture is illustrated in Figure 5.5. With the normalized voltage difference as input, four fully connected hidden layers with 2048 neurons in each layer were employed. For each neural in the hidden layer, an exponential linear unit is implemented. Even though the ANN system was trained with material properties in 1 kHz and 100 kHz excitation frequencies, the system could be adapted to different pairs of excitation frequencies because of the normalized inputs and outputs.

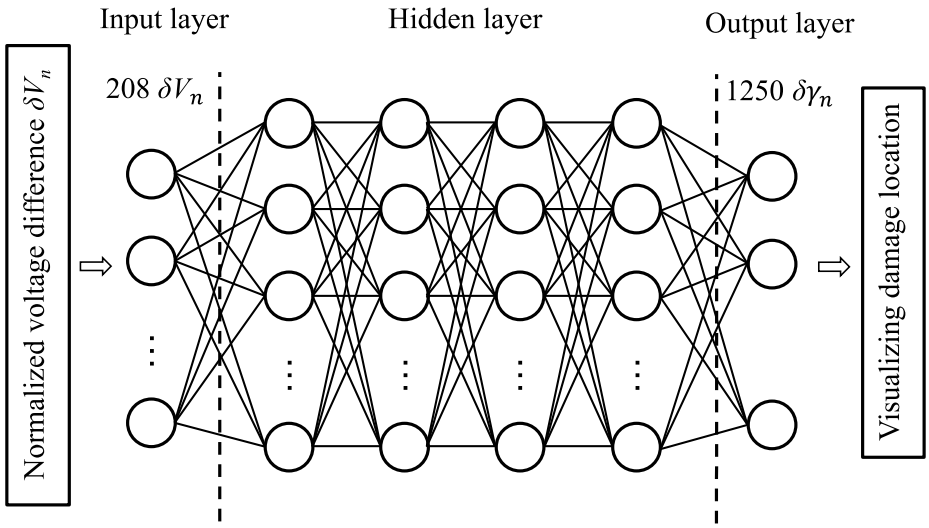

Figure 5.5: The architectures of the ANN system is illustrated.

5.4 Simulation Details and Results

5.4.1 Simulation Details

The network trained with datasets mentioned in Section 5.3.2 was used in the simulation tests directly. Four damaged cases were investigated in the simulation with randomly propagated damage as shown in Figure 5.6. Two injecting frequencies, 100 kHz and 1 kHz were selected here for the simulated fdEIT interrogation. The choice of 100 kHz and 1 kHz is a decent representation to investigate the performance of the classical fdEIT solver and the fdEIT-ANN system, and the discussion of other pairs of frequencies was not further included in this section because only the reconstructed scale would be slightly different. Therefore, the complex conductivity in the damaged regions shown as blue in Figure 5.6 maintains 0 S/m, while the undamaged regions were imposed with 58.35 S/m and 11.83 S/m complex conductivity in sequence. Then the synthetic boundary voltages were calculated by the forward problem solver for the two distributions of each damage case. The corresponding simulated noise-free boundary voltages were then corrupted by white Gaussian noise with a 66.2 dB SNR.

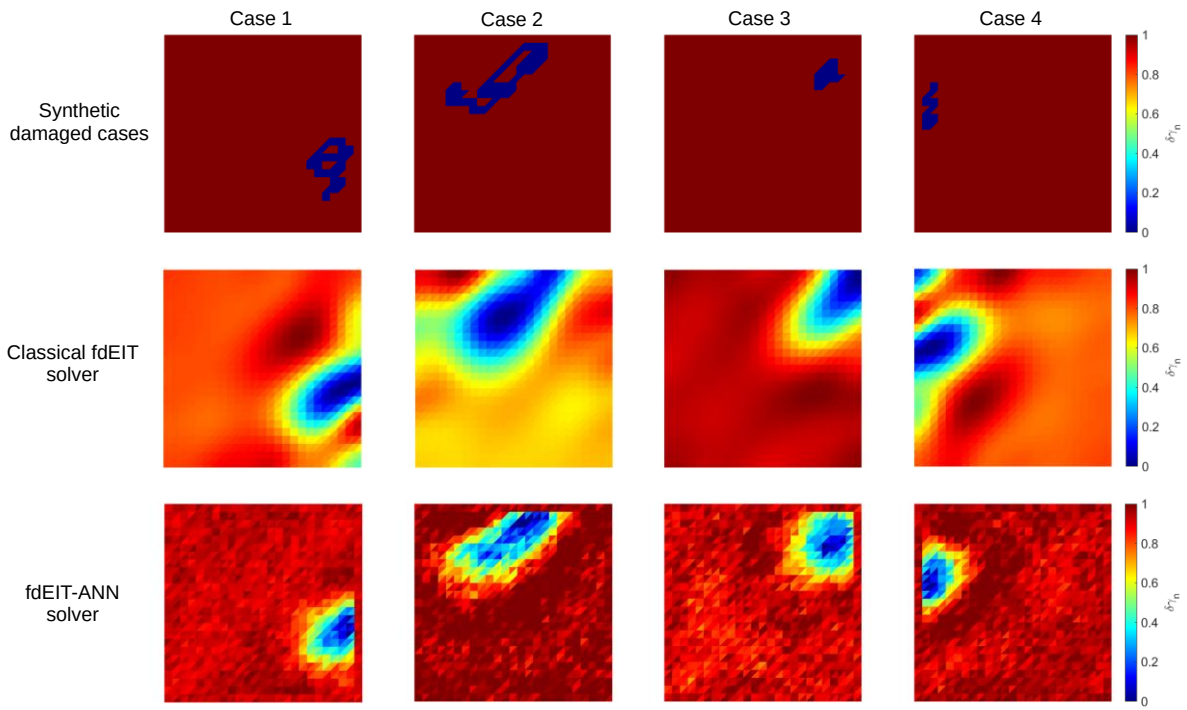

Figure 5.6: Four damaged cases were investigated in the simulation. The simulation results and the visualization of four damaged cases were obtained from the classical fdEIT and the fdEIT-ANN system.

The difference of synthetic boundary voltages in two excitation frequencies was first fed into the classical fdEIT solver to obtain the complex conductivity distribution. Then the effectiveness of the fdEIT-ANN system in detecting damaged regions was examined. The calculated normalized voltage differences (δV_n^i) were employed in the system as inputs, and the outputs $\delta\gamma_n$ of were visualized in a 2D map.

In addition, a sythetic strained state with a concentrated tensile strain shown as Figure 5.7a was considered. The region in blue was assumed to be subject to a tensile strain. According to the material characterization in Section 5.2, the piezoresistive properies decrease while the injecting frequency increases. Therefore, in order to utilize large response to obtain better reconstruction performance, 1 kHz and 50 kHz frequencies were chosen to interrogate the strained case. With 533 $\mu\varepsilon$ tensile strain, the normalized impedance change is 0.074 and 0.00018 with a 50 kHz and a

1 kHz excitation frequencies. Hence, the complex conductivity in strained and unstrained regions are 11.01 S/m and 11.83 S/m with a 1 kHz excitation, and the complex conductivity in the whole domain maintains as 30.52 S/m with a 50 kHz excitation. The corresponding synthetic boundary voltages were then calculated and fed into the classical and the fdEIT-ANN solvers for processing.

5.4.2 Evaluation criteria

The interpretation of the normalized change of complex conductivity distribution to a damage map is achieved by including the finite element in the damaged region where $\delta\gamma_n$ in the element is larger than half of the maximum complex conductivity change. To quantitatively compare the performance of damage detection between classical fdEIT and fdEIT-ANN system, evaluation criteria were employed. Here, the position error e_p and shape deformation error e_s were considered as:

$$e_p = \frac{|C_r - C_t|}{l} \tag{5.3}$$

$$e_s = \frac{A_r}{A} \tag{5.4}$$

where C_r and C_t are the centroids of the reconstructed and true damaged region, respectively, A_r is the area that is included in the reconstructed damage region but not in the true damage region, and l and A is the length and area of the square specimen [29].

5.4.3 Simulation results and discussions

The results from the classical fdEIT solver and the fdEIT-ANN system are shown in Figure 5.6. The complex conductivity distributions from the classical fdEIT were normalized by the maximum change to offer an efficient comparison with the results from the fdEIT-ANN system.

Table 5.1: Image errors quantification and comparison of four simulated damage cases

Position error e_p	Classical fdEIT solver	fdEIT-ANN system
Case 1	0.0508	0.0304
Case 2	0.0513	0.0143
Case 3	0.0409	0.0354
Case 4	0.0190	0.0151
Shape deformation error e_s	Classical fdEIT solver	Classical fdEIT solver
Case 1	0.0848	0.0240
Case 2	0.0608	0.0488
Case 3	0.2328	0.0552
Case 4	0.0608	0.0168

For the cases with damage shown in different locations, classical fdEIT solver could reconstruct the area with low $\delta\gamma_n$ roughly, but accompany an enlarged area than the true damaged region and artifacts shown at the undamaged region. In the results for Case 1 and Case 4, artifacts were shown in the bottom right corner and the top left corner respectively. The region with low $\delta\gamma_n$ values could also be identified as a damaged region and influence further decision-making. The image errors are stated in Table 5.1. The application of the iterative solver in the inverse reconstruction process may improve the results by gradually reducing the low $\delta\gamma_n$ region and approaching the true damage region, however, the artifacts in the background are difficult to be eliminated. Moreover, the processing time of the iterative solver is much longer than the one-step linearization method employed here.

In contrast, the results from the fdEIT-ANN system could detect the damaged region more accurately. Even though the background of these images is not smooth as images from the classical solver because of the unutilized regularization method, it will not influence the image evaluation because the variation of $\delta\gamma_n$ in each background finite element is much smaller than half of the maximum change. In Table 5.1, the position errors and shape deformation errors for images from the fdEIT-ANN system are both a few times smaller than from the classical fdEIT solver. For Case

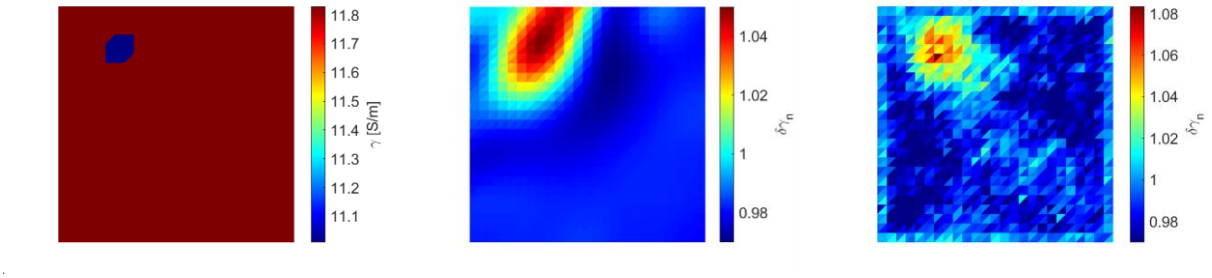

(a) (b) (c)

Figure 5.7: (a) The complex distribution for the strained case in 1 kHz excitation was shown. The reconstructed images were obtained from (b) the classical fdEIT and (c) the fdEIT-ANN system.

Table 5.2: Image errors quantification and comparison of the simulated strained case

	Classical fdEIT solver	fdEIT-ANN system
Position error e_p	0.0343	0.0279
Shape deformation error e_s	0.0872	0.0360

3 with the solid damage, the result from the fdEIT-ANN solver has a 5 times lower shape deformation error than from the classical solver. However, the topological damage is difficult to be accurately identified by the fdEIT-ANN system. For a state with strong topological damage as in Case 2, the shape deformation error only diminished 1.2 times.

Moreover, the images for the strained case were shown in Figures 5.7b and 5.7c. The complex conductivity difference between two excitations in the strained region is 19.51 S/m, which is slightly larger than the difference in the unstrained region 18.69 S/m. So the reconstructed strained region is shown in red. The result from the fdEIT-ANN system is more accurate than from the classical fdEIT solver, and the image errors for the two reconstructions are stated in Table 5.2.

5.5 Experimental details and results

5.5.1 Experimental details

Following the simulation study, experimental investigations were conducted to validate the effectiveness of the aoolication of fdEIT technique on the nanocomposite smart paint. The nanocomposite spray, prepared according to the procedure outlined in Section 5.2.1, was applied onto a square-shaped TPU sheet measuring 50×50 mm^2. The spraying process ensured an even and consistent coating of the nanocomposite on the sheet, allowing for subsequent experimental measurements and analysis. Then, 16 conductive threads were equidistantly attached to the sample with drying colloidal silver paste.

The DAQ system used in this chapter was identical to the one described in Chapter 4, depicted in Figure 4.10b. It comprises a current generator, a multifunctional switch, and an interface. The current source was set to deliver 20 mA AC currents to an adjacent pair of boundary electrodes. The switch then sequentially measured and recorded a total of 208 AC voltage measurements along the boundaries of the specimen. This setup allowed for precise control and accurate data collection during the experimental measurements.

A circular damage region was manually etched off from the nanocomposite paint sample on the left side (Figure 5.8a). Subsequently, 20 mA AC currents at frequencies of 1 kHz and 5 kHz were applied to the sample through electrodes by sequence. The resulting AC measurements were recorded and utilized for the reconstruction process.

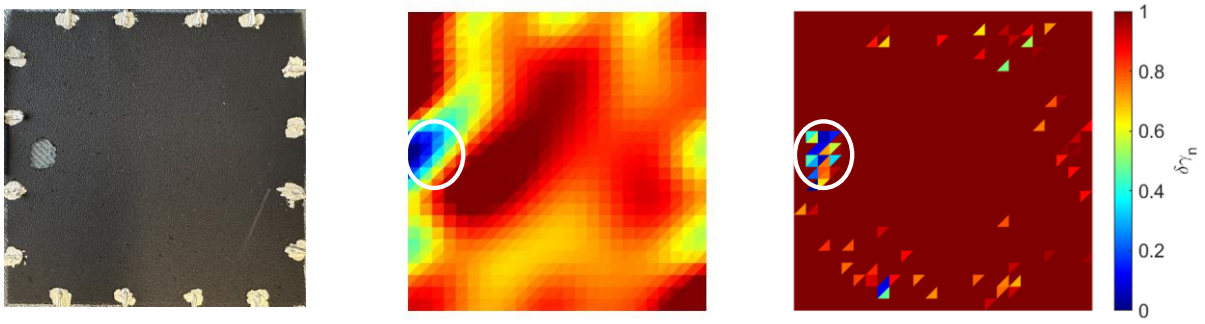

(a) (b) (c)

Figure 5.8: (a) A circle region was etched off in the nanocomposite smart paint. The reconstructed images were obtained from (b) the classical fdEIT and (c) the fdEIT-ANN system.

5.5.2 Experimental results and discussions

Figure 5.8a and 5.8b depict the reconstructed normalized complex conductivity maps obtained from the fdEIT method. Both reconstructions successfully detected the complex conductivity difference resulting from the smart paint excited at different frequencies. The damage was localized as the blue spot, indicating the normalized conductivity change close to 0. However, some artifacts were observed outside the damage area in both reconstructions. The classical solver generated smooth artifacts because of the Tikhonov regularization method, while the ANN system produced scattered artifacts.

5.6 Conclusion

In this chapter, a MWCNT-based smart paint was developed for damage and strain sensing. The unique frequency-dependent complex conductivity of the smart paint enables the application of fdEIT, eliminating the need for baseline measurements. Furthermore, the implementation of data-driven deep ANN technique enhances the efficiency of the fdEIT process. Simulations and experiments were conducted to validate the effectiveness of the proposed method in damage and strain sensing using the MWCNT-based paint and fdEIT-ANN method.

Acknowledgement

Chapter 5, in part, is currently being prepared for submission for publication of the material. Shu, Yening, Li, Sijia, and Loh, Kenneth J. The dissertation author was the primary investigator and author of this material.

CHAPTER 6 COMPOSITE DAMAGE DETECTION WITH PLANAR NONCONTACT CAPACITIVE IMAGING AND DEEP LEARNING

6.1 Introduction

As mentioned in previous chapters, CFRP composites are extensively used in aircraft, naval structures, and the automotive industry because of their outstanding lightweight and mechanical performances. Compared to conventional metals, CFRP composites have significant advantages such as light weight, enhanced mechanical strength, better fatigue performance, and high corrosion resistance [1,2,20]. However, unexpected impacts, other severe loadings, or environmental effects during their operation life may cause damage or even failure of these composite parts. The possible damage modes are not limited to delamination, fiber/matrix debonding, fiber breakage, and transverse cracks [15,16,22]. Especially, the inside damage and delamination in the laminated structures are very hard to be visually detected.

Here in this chapter, the relationship between damage modes and electrical permittivity and conductivity changes in the composites were leveraged to develop and validate experimentally a noncontact, capacitive imaging system for assessing damage and delamination in CFRP composite panels. Classical ECT operates by measuring changes in capacitance between multiple electrode pairs surrounding the object of interest, and the sensing domain is usually defined as the circular area enclosed by the boundary electrodes [62]. Circular ECT offers impressive sensitivity in the sensing domain, however, its primary limitation is the constraint on the shape of the objects that can be inserted into the circular electrode array. As an advanced variant, planar ECT focuses on a two-dimensional electrode arrangement, which expands the applicability of ECT to structures with different dimensions and shapes [63].The advent of planar ECT has also unlocked its potential for damage detection in large-scale complex structures, such as fleets or aircraft. Inspectors can

employ the designed planar ECT electrode array to efficiently scan these structures, enabling rapid and accurate assessments of their internal properties. This non-invasive approach to structural health monitoring ensures the early identification of potential issues, thereby enhancing overall safety and operational efficiency.

To guarantee effective scanning, processing time must be minimized. A supervised machine learning method that utilizes the deep ANN has been used in the capacitive imaging solver for achieving a high-resolution and time-efficient damage detection process. Adjacent measurements from the planar capacitive electrodes with strong sensitivity were employed in this chapter to render the measurement reduction, which not only decreases the influence of the low signal-to-noise ratio from measurements of other pairs of electrodes but also improves the deep ANN performance by reducing the input dimensionality. Because of the electrically conductive characteristic of CRRP composite, the complex impedance model was utilized here to generate training data for the network. With the presence of damage, the permittivity and conductivity are decreasing in a certain area and could be captured by the capacitance measurements. A portable planar electrode array has been prototyped. The imaging system has been used to visualize subsurface damage features and to characterize spatial damage sensing accuracy and sensitivity.

6.2 Methods

6.2.1 Classical Planar ECT solver and Complex Impedance Model

In this chapter, a 12-electrode planar ECT system was with a 4×3 rectangular electrode array assembly was utilized as shown as Figure 6.1. The 20×20 mm^2 electrodes were deposited on

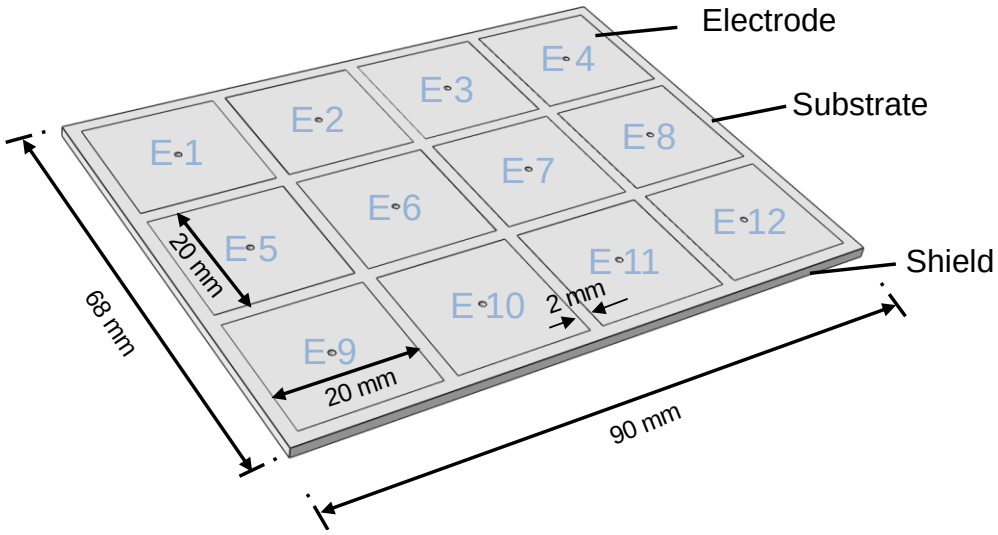

Figure 6.1: A 12-electrode planar ECT system was assembled to form a 4×3 rectangular array.

one surface of the substrate. During the inspection, the ECT electrode array would be placed close to the target surface, and a 15 V AC voltage with 1.25 MHz frequency will be excited in each electrode by sequence while others remain grounded. In each excitation, the capacitance between the excited electrodes and the following grounded electrodes will be measured. Here, a total of 66 capacitance measurements would be recorded for each inspection for the following reconstruction and damage characterization processes. The inspection continues to the following regions of interest after the completion of a full set of measurements.

The classical planar ECT solver used in this chapter also consists of the forward problem and the inverse problem [22]. In Section 2, the governing equation for the ECT method for nonconductive materials is explained in detail. However, due to the conductive properties of CFRP, a complex impedance model should be used for its characterization instead of the general ECT model for nonconductive materials. The ECT impedance model is updated as:

$$\nabla \cdot \left((\frac{\sigma}{i\omega} + \varepsilon) \nabla \phi \right) = 0 \text{ in } \Omega \tag{6.1}$$

The Dirichlet and Neumann boundary conditions are:

$$\phi = V_l \text{ on } \Gamma_1 \tag{6.2}$$

$$(\frac{\sigma}{i\omega} + \varepsilon) \frac{\partial \phi}{\partial n} = 0 \text{ on } \Gamma_2 \tag{6.3}$$

The complex impedance is represented by a complex quantity that has both a real and imaginary component. The real component is related to the conductivity of the material, while the imaginary component is related to its electrical permittivity. When dealing with nonconductive materials such as CFRP composites, the inspected object could be viewed as a parallel combination of an equivalent capacitor and resistor in the model. The relative influence of the capacitor and resistor on the impedance is determined by the frequency. When a low frequency is excited on the material with low conductivity, the capacitor dominates. While inspecting a high-conductive material, the resistor dominates [61]. While increasing the excitation frequency may allow capacitor dominates on a high-conductive material [61]. Here in this chapter, considering the conductive properties of CFRP composites, a high excitation frequency of 1.25 MHz was chosen.

In the forward problem, electrical capacitances between electrodes would be calculated for a given distribution of conductivity and dielectric properties with Equation (6.4) using the finite difference method [62].

$$C_{lm} = \frac{1}{V} \int_{e_l} \varepsilon \frac{\partial \phi_l}{\partial n} dS \tag{6.4}$$

The change of conductivity distribution and electrical permittivity would be both taken into account and would be captured in the capacitance measurements. In Figure 6.2, the comparison of

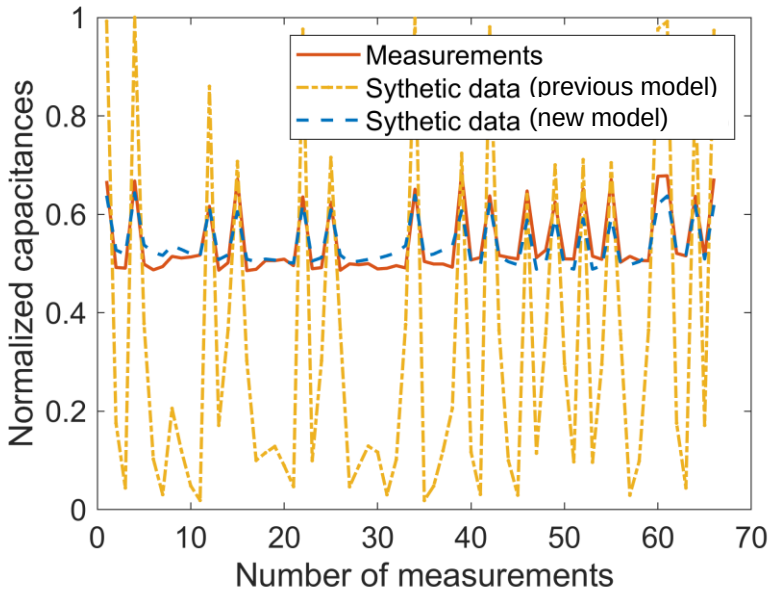

Figure 6.2: A total of 66 normalized measurements from the 12-electrode planar ECT system on a CFRP panel were compared with the synthetic data from the nonconductive ECT model and the complex impedance model.

normalized capacitance measurements on a CFRP panel and the synthetic data from the previous model and the new complex impedance model was shown. The influence of the material conductivity makes normalized capacitance measurements drift above, which has a low upper bound and a high lower bound. That is because the conductive property and electron movement decreases the difference between capacitances measured from two close electrodes and two electrodes far away. Therefore, synthetic capacitance data generated from the new complex impedance model is more consistent with capacitance measurements than the data from the previous model.

In the inverse problem, measurements were taken within the planar electrodes array to reconstruct the electrical properties of the inspected domain. Two different conditions were investigated, an undamaged state and a damaged state, and measurements were taken for each condition. The difference between the two measurements would then be utilized in difference

imaging with the one-step linearization method to reconstruct the electrical properties change in the domain. Electrical properties within the CFRP panel are influenced by its internal structure and composition, and the presence of damage will alter the values. Damage and delamination in the CFRP composites can reduce the permittivity of the panel while causing the conductivity to decrease or become 0 S/m. Therefore, electrical conductivity and permittivity distributions both could offer damage state information of the inspected CFRP panel. However, because the dielectric properties dominate in the high-frequency excitation in this study, only permittivity distributions were reconstructed here. This updated model will help improve the damage characterization on CFRP composites.

6.2.2 Reduced measurements

The planar configuration of electrodes in a capacitive imaging system can have a significant impact on the sensitivity and accuracy of the measurements obtained. Specifically, due to the nature of the capacitive imaging technique, measurements obtained from adjacent electrodes are likely to produce a larger response than measurements obtained from electrodes that are farther away. Even though the capacitance measurements obtained from adjacent pairs of electrodes and from electrodes that are further apart will exhibit less difference in CFRP composites due to their conductivity properties, the change in capacitance observed in the electrodes that are further apart due to a change in the electrical properties distribution is still very low. In addition, measuring capacitance accurately from electrodes that are farther apart can be challenging due to the potential influence of environmental noise.

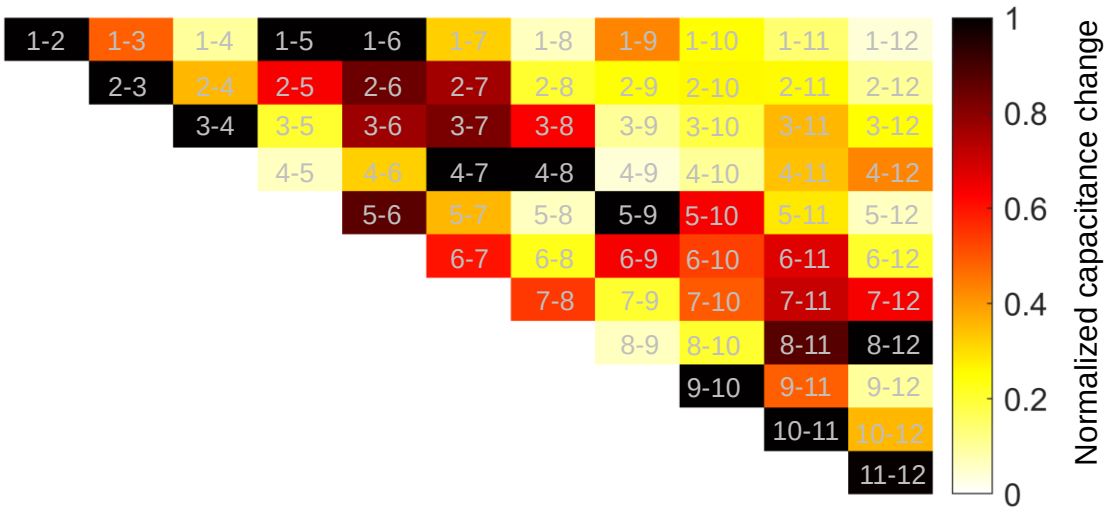

Figure 6.3: Synthetic normalized capacitance change between a simulated CFRP composite on top and air.

To reduce the impact of environmental noise on the measurements and to improve the efficiency of the measurement process, it may be advisable to prioritize measurements with larger response amplitudes. To quantify the responses, a CFRP composite was simulated to place on the top of the planar electrode array, and the synthetic capacitances were computed using the forward problem solver with the complex impedance model. The normalized synthetic capacitance change were calculated as:

$$C_{lm}^{N} = \frac{C_{lm}^{c} - C_{lm}^{a}}{max(C_{lm}^{c} - C_{lm}^{a})} \tag{6.5}$$

where $C_{lm}{}^{c}$ is the capacitance calculated when a CFRP is placed on the top of the electrodes array, while $C_{lm}{}^{a}$ is the synthetic capacitance measurements of air.

In Figure 6.3, the normalized capacitance changes were plotted. The horizontal adjacent pairs of electrodes such as 1-2, 2-3, 3-4, vertical adjacent pairs of electrodes such as 1-5, 5-9, and diagonal adjacent pairs of electrodes such as 1-6, 2-7, all shows in red or black which represent

large change of capacitances between the two states. Capacitance changes in other pairs of electrodes shown in orange or yellow in this figure are much lower than from those adjacent electrodes. Especially the normalized capacitance changes between Electrode 1 and Electrode 12, which are the farthest electrode pair, is very low and shown in light yellow. Therefore, to effectively reduce the effects of measurement noise and improve data quality, only measurements between adjacent pairs of electrodes are utilized to form a set of reduced measurements and following reconstruction process. This process help simplify the mathematical modeling of the system and improve the computational efficiency of the reconstruction algorithms.

6.2.3 Planar ECT-ANN System

In the classical ECT solver, the inverse problem solver with difference imaging technique was used to reconstruct the electrical permittivity distribution. However, as mentioned in Section 2, the model-based solver is computationally inefficient and could hardly be applied in the real time scanning inspection process. Therefore, a planar ECT-ANN system was generated in this chapter to reconstruct permittivity distribution change using variation of capacitance measurements.

In the planar ECT-ANN system, the conductivity change $\delta\varepsilon$ and corresponding capacitance change (δC) obtained from the planar ECT forward problem solver using FE method would be fed into the deep ANN as outputs and inputs for training process. The efficiency and accuracy of the deep ANN were enhanced by converting the output of 3D inspected region into a 2D map. This help reduce the dimensionality of output to 1884 neurons, and it was achieved by projecting the tetrahedral finite element onto 1884 triangle finite elements using the k-nearest neighbors algorithm based on the element centroid. Here, the reduced 29 adjacent measurements were used

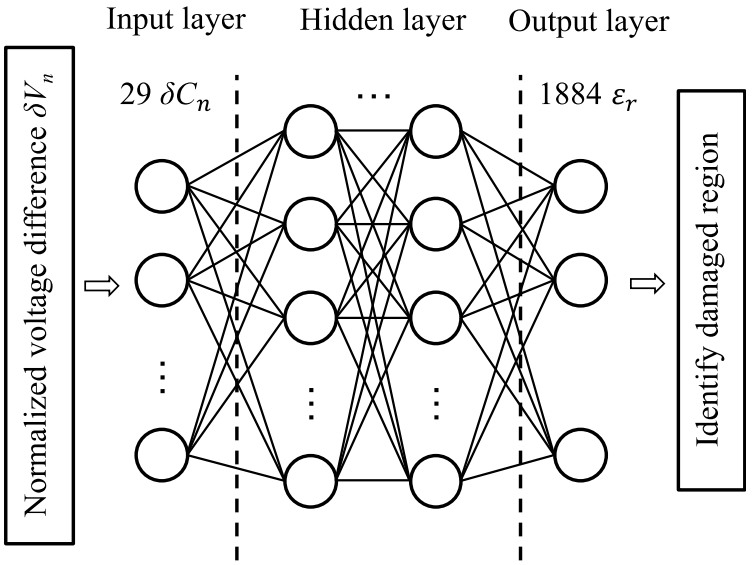

Figure 6.4: The architectures of the deep ANN system is illustrated.

as input to train the networks, and finally obtain a deep ANN system with the reduced adjacent measurements. The trained deep ANN system then could be used to identify the region with permittivity decrease as the damage location with the input of capacitances change.

To prepare the training sets, an undamaged case and 5000 damaged cases with random finite element defect were examined with the forward problem solver for capacitance measurements. The electrical permittivity and conductivity decrease to 8.854×10^{-12} F/m and 0 S/m respectively in the damaged region. The measurements were then added with white Gaussian noise of 66.2 dB signal to noise ratio (SNR) and the normalized difference of simulated voltages between each damaged state and undamaged state is calculated as:

$$\delta C_n = \frac{C^d - C^0}{c} \tag{6.6}$$

where c is the maximum absolute measurement on the undamaged structure. The output in ANN is the normalized electrical permittivity change:

$$\delta\varepsilon_n = \frac{\varepsilon^d - \varepsilon^0}{\varepsilon^0} \tag{6.7}$$

where ε^d is the electrical permittivity distribution in the damage state, and ε^d is in the undamaged state. In Figure 6.4, the deep ANN architecture is illustrated. After being trained, the ECT-ANN system can be used to reconstruct images of the electrical permittivity distribution. The distribution could be used to identify damage by detecting decrease in the permittivity caused by the damage.

6.3 Experimental Details

To validate the effectiveness of this method, a prototype planar ECT system was manufactured and utilized to conduct experiments. The assembly consists of a panel with an electrode array, a data acquisition (DAQ) unit, and RG 174 coaxial cables connecting the two parts together. The electrode array was commercially printed with PCB (Printed Circuit Board) with aluminum, including 12 boundary electrodes, each 20×20 mm^2, arranged in a 3×4 pattern on the front surface of the board. A 1 mm diameter hole was drilled in the center of each electrode, allowing for a conductive path between the front and back surfaces of the PCB in a constrained region. To further improve the electrical performance of the ECT system, a conductive shield was printed onto the remaining region of the back surface of the PCB with a gap. The shield was designed to minimize electromagnetic interference (EMI) effects, which can cause unwanted noise and interference in ECT measurements. By printing the shield onto the back surface of the PCB, the ECT system was able to operate more reliably and with greater accuracy. A total of 12 RG174 coaxial cables were respectively soldered on the electrode region and the shield region of the board backside, and then connected to the DAQ unit. A commercialized high-speed capacitance measuring unit was utilized for ECT interrogation and DAQ. The unit outputs 1.25 MHz, 15 V peak-to-peak, square waves, and travels with the cable to the electrodes array for ECT interrogation.

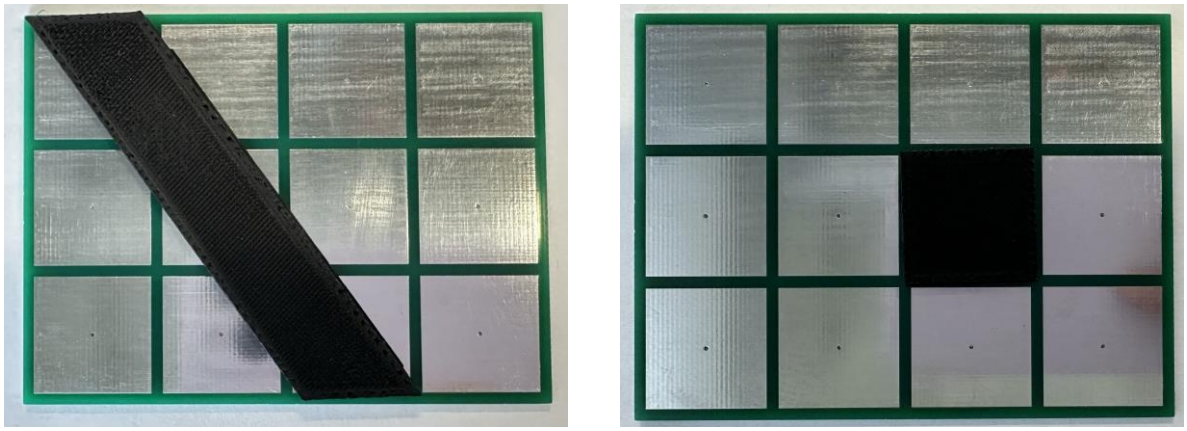

(a) (b)

Figure 6.5: (a) A 45-degree block with 1 mm thickness, and (b) a 22×22×1 mm^3 rectangular cuboid block were 3D printed with conductive PLA and placed on the ECT electrode array.

6.3.1 Modularized Conductive PLA

Prior to the direct examination of CFRP panels with impact damage or delamination, conductive PLA blocks which were fabricated by the FDM Ultimaker 3+ 3D-printer were first used for the examination. This is due to the similar conductive properties of the PLA modules and the CFRP composites. The conductive PLA modules can be placed onto the ECT electrode array at different locations and with varying sizes to simulate the conductivity and electrical permittivity perturbations that are observed in damaged CFRP panels. This allows for testing of the planar ECT system's ability to detect and locate perturbations in the region of interest in a more comprehensive and flexible manner. First, a 45° block with 1 mm thickness (Figure 6.5a) that could diagonally cover electrode 1 to electrode 11 was 3D printed for the following evaluation of reduced measurement efficiency. Additionally, 22×22×1 mm^3 rectangular cuboid blocks which could cover an electrode and its surrounding gaps, as shown in Figure 6.5b, were fabricated. These blocks were used to test the planar ECT system's ability to accurately localize conductivity and permittivity perturbations.

6.3.2 Impact Damage Imaging

To further test the ECT ability of impact damage detection on the CFRP panel, A CFRP composite was fabricated using Hexcel HexForce Carbon Fiber Fabric Plain Weave 3k 5.8oz/197gsm Style 282 and epoxy resin infused using the VARTM (Vacuum Assisted Resin Transfer Molding) process. Three regions with dimensions of 125 mm x 75 mm were chosen and fixed at the boundaries in the composite panel. The three regions were then subjected to impact using a 0.254 mm radius dropping the ball with three different energies: 10.1 J, 20.2 J, and 30.4 J, respectively. The impact energy from the dropping ball will be transferred to the CFRP panel, propagating through the material as stress waves. If the impact energy in this test surpasses the material's ultimate strength, stress waves can cause damage such as delamination, fiber breakage, or matrix cracking to some extent in the impacted region. The extent and severity of the damage will depend on the impact energy and the design of the composite structure.

During the inspection process, the undamaged region within the CFRP panel was first examined to obtain the undamaged state measurement C^0. Then the impacted regions were then inspected by the ECT electrode array for the measurements of the different damaged states C^i.

6.3.3 Delamination Imaging

Other than damage caused by impact, delamination is also a common type of damage in composite materials, and it can significantly reduce the structural integrity of the material. In this chapter, the use of ECT to detect and image delamination in a CFRP panel was also investigated. Four CFRP panels measuring 68×90 mm^2 and containing $[0]_6$ plies were fabricated by vacuum bagging, each featuring single-layer delamination of varying sizes and locations. The process of fabricating the CFRP panels with delamination involved stacking six layers of prepregs and then

curing them using the vacuum bagging method. Delamination was purposely introduced between the third and fourth prepregs using release film of varying sizes, including 22×22 mm^2, 22×45 mm^2, 22×68 mm^2, and 45×45 mm^2. The resulting composites with delamination were labeled as D1, D2, D3, and D4, with D1 having the smallest delamination and D4 having the largest. In addition to fabricating the composite panels with delamination, an undamaged panel with the same six-prepreg stacking was also produced without introducing any release films. This panel is referred to as P1.

First, ECT interrogation was conducted on the undamaged composite panel P1 to obtain measurements in the undamaged state. Then, the panels with delamination (D1-D4) were inspected in order, and the differences in measurements were used as input for both the classical ECT solver and the planar ECT-ANN system. The detailed results of the ECT interrogation as well as the analysis using the classical ECT solver and ECT-ANN system are presented in the following section.

6.4 Experimental Results

The planar ECT system was used to interrogate the CFRP panels with impact damage and delamination, as well as the conductive PLA modules. The resulting measurements were then processed using both the classical ECT solver and the ECT-ANN system. The following section presents a detailed analysis of the results obtained from these experiments.

6.4.1 Modularized Conductive PLA Imaging

In Figure 6.6, the imaging results of a diagonal PLA block placed on the ECT electrode array were presented. The results obtained from the classical solver using the full set of

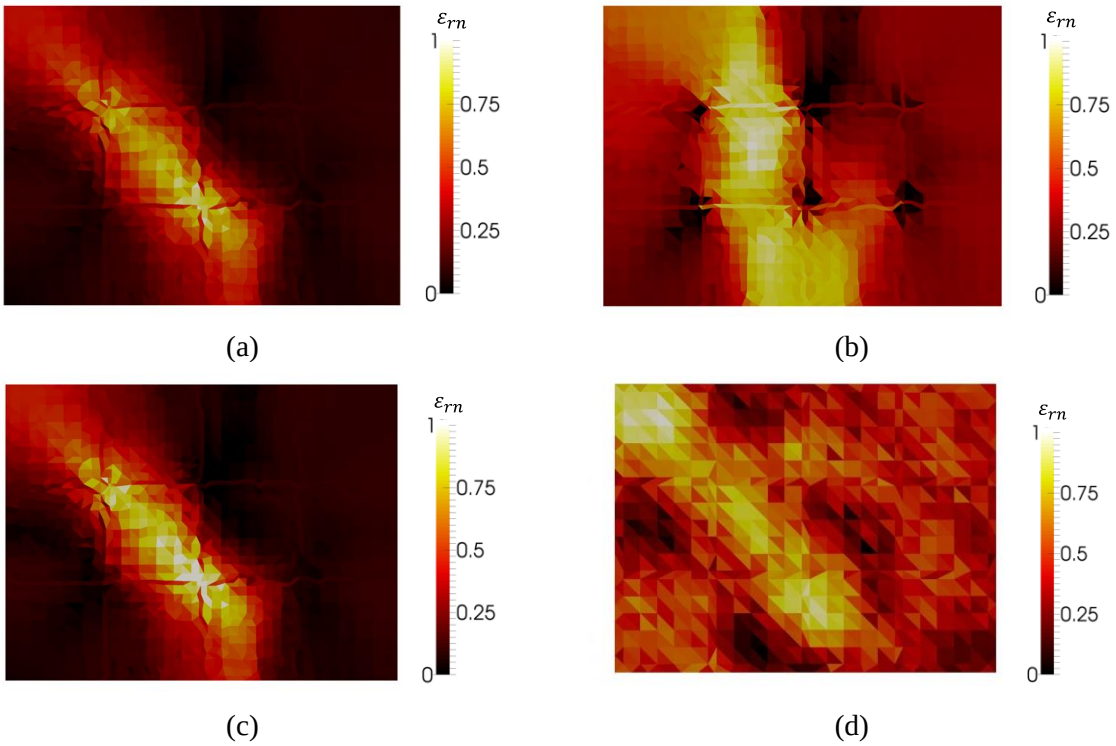

Figure 6.6: A diagonal PLA was placed on the ECT electrode array and the measurements was employed for reconstructions by (a) classical ECT solver with the whole set of measurements, (b) classical ECT solver with H/V measurements, (c) classical ECT solver with H/V/D measurements, (d) ECT-ANN system with reduced measurements.

measurements, the reduced measurements from H/V (horizontal and vertical) adjacent electrodes, and the reduced measurements from H/V/D (horizontal, vertical and diagonal) adjacent electrodes were displayed in Figures 6.6a to 6.6c, respectively. The classical solver with reduced H/V/D measurements was able to produce an image that was almost identical to the image produced with the full set of measurements. This is because the perturbation was mostly captured by the adjacent pairs of electrodes. However, the results from the H/V measurements neglected the variation of measurements in diagonal adjacent electrode pairs. As a result, the imaging in Figure 6.6b was distorted and did not accurately reflect the actual location of the perturbation. In Figure 6.6d, imaging from the planar ECT-ANN with reduced measurements was shown to also detect the

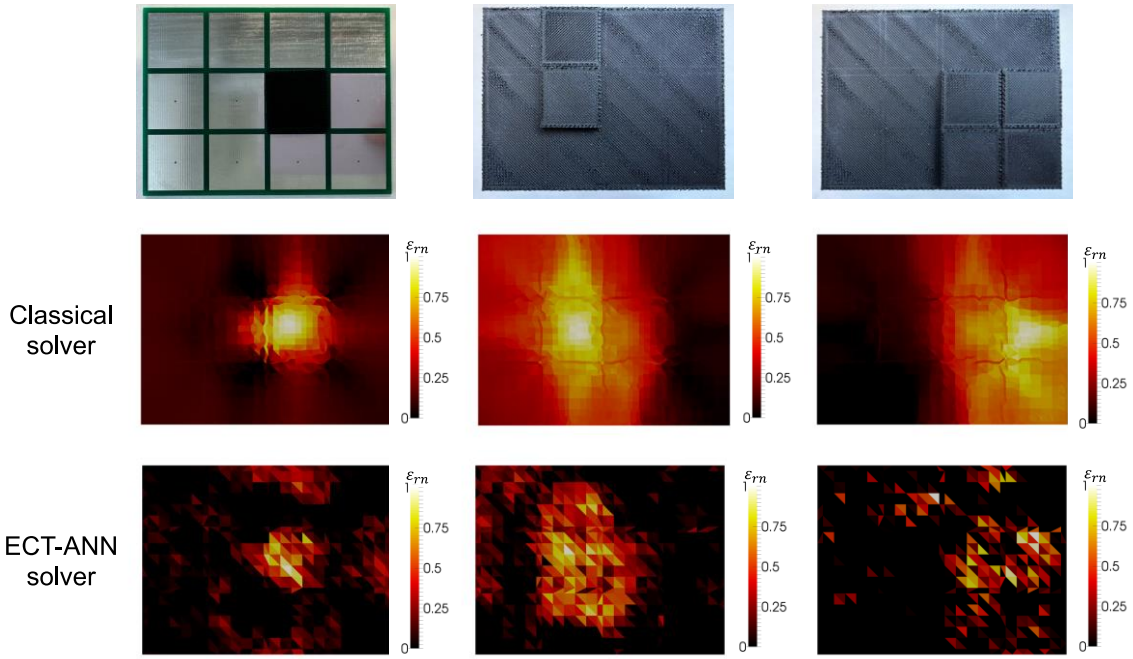

Figure 6.7: Conductive PLA modules were placed on the ECT electrodes and then a conductive base. The reconstructions were solved with the corresponding measurements by classical ECT solver with reduced measurements (second row) and ECT-ANN system with reduced measurements (third row).

diagonal pattern of the perturbation. The planar ECT-ANN system was able to produce an image with much less time while still maintaining accuracy to some extent.

After evaluating the effectiveness of reduced H/V/D measurements, the study proceeded to examine the imaging ability of perturbations of small conductive PLA modules on the planar ECT system. A small module was first placed on the electrode array, and then two additional modularized PLA perturbations were placed on a 68×90×1 mm^3 3D-printed conductive PLA base to simulate a subsurface perturbation. Both the classical ECT solver and the planar ECT-ANN system were able to accurately identify the location of the perturbations caused by the conductive PLA modules.

6.4.2 Impact Damage Imaging Results

Following the evaluation of the planar ECT system's imaging capability in detecting small perturbations of conductive PLA modules, the study continues by investigating its effectiveness in imaging impact damage in CFRP panels. To evaluate the localization ability of the planar ECT system, the electrode array was first used to interrogate the panel under 30.4 J impact in the region of the blue box shown in Figure 6.8a to 6.8b. The planar ECT-ANN system was used to process the measurement difference between the damaged state and an undamaged state, and the solved images are shown in Figure 6.8a and 6.8b. The damaged region was indicated by a relative decrease in electrical permittivity in the reconstructions. By moving the inspection location, the damaged imaging area was found to move accordingly, thereby validating the effectiveness of this method in detecting impact damage. The reconstructed damaged region shown in the images is

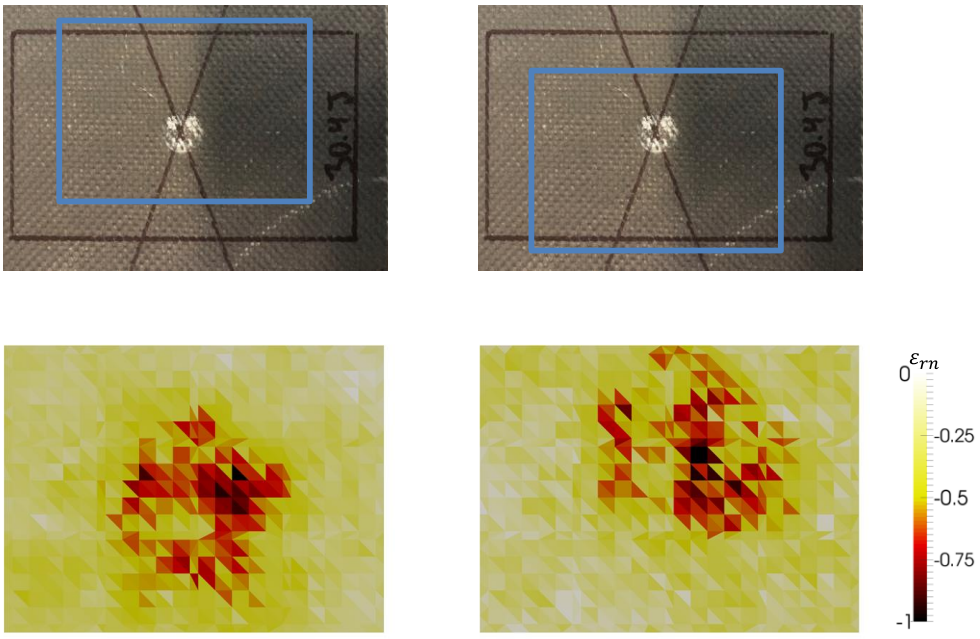

Figure 6.8: Impact (30.4 J) imaging solved by ECT-ANN system with reduced measurements.

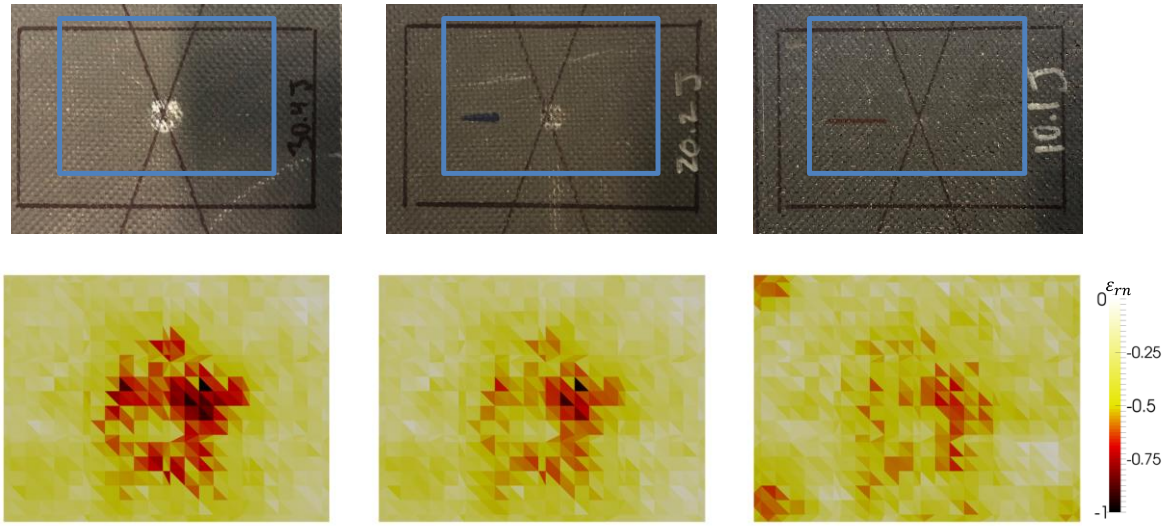

Figure 6.9: Impact (30.4 J, 20.2 J, 10.1 J) imaging solved by the ECT-ANN system with reduced measurements.

larger than the actual impact contact region, which can be attributed to the propagation of stress waves throughout the material.

Furthermore, the regions under different impact energy levels were then inspected using the ECT electrode array. The reconstruction results were normalized by the maximum change in the case under 30.4 J impact and shown in Figure 6.9a to 6.9c. The images demonstrate that increased impact energy results in larger permittivity decreases. However, in the case of the CFRP panel subjected to a 10.1 J impact, image artifacts were observed on the left side of the reconstruction due to the relatively small perturbation.

6.4.3 Delamination Imaging Results

Finally, the CFRP panels with intentionally introduced delamination were examined using the planar ECT system. The results of the classical ECT solver and the planar ECT-ANN system are presented in Figure 6.10, which demonstrates their ability to effectively detect and image the delamination damage.

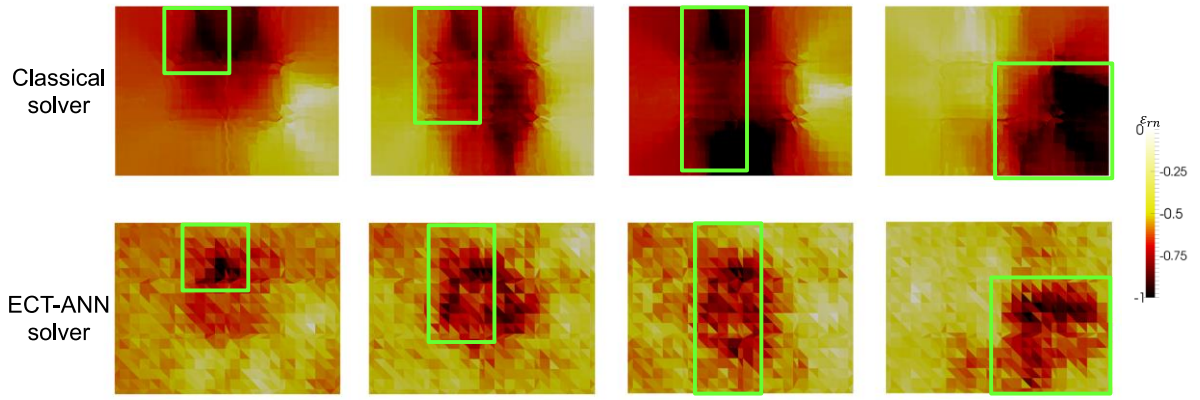

Figure 6.10: Delamination imaging solved by the ECT-ANN system with reduced measurements.

6.5 Conclusion

In conclusion, the planar ECT-ANN system proved to be an effective method for detecting damage in CFRP panels. The system was able to accurately detect and localize perturbations in the electrical permittivity of the material, both in simulated perturbations using conductive PLA modules and in actual impact damage and delamination in CFRP panels. The effectiveness of the system was demonstrated through experiments using different impact energies and sizes of delamination. Furthermore, the use of reduced H/V/D measurements was also evaluated and found to be effective in reducing measurement time while maintaining accuracy. Overall, the planar ECT-ANN system provides a promising approach for non-destructive evaluation of CFRP structures, with potential applications in aerospace, automotive, and other industries.

Acknowledgement

Chapter 6, in part, is currently being prepared for submission for publication of the material. Shu, Yening, Dela-cueva, Janelle, Kim, Hyonny, and Loh, Kenneth J. The dissertation author was the primary investigator and author of this material.

CHAPTER 7 CONCLUSION

In this thesis, the objective was to investigate the effectiveness of non-invasive electrical tomographic imaging techniques, including ERT, EIT, and ECT, for damage detection in advanced structures such as CFRP composites and lattice structures. The thesis aimed to overcome the limitations of classical methods and explore modifications and enhancements to improve their applicability. Additionally, machine learning methods were incorporated to increase computational efficiency and real-time defect detection. Through simulation and experimental studies, the performance of these techniques was evaluated, and their results were compared with classical solvers. The findings highlight the potential of electrical tomographic imaging techniques for damage detection in advanced structures, addressing the need for accurate and efficient inspection methods in the field.

7.1 Conclusion and Contributions

In chapter 2, the fundamental aspects of electrical tomographic methods, including ERT, EIT, and ECT, were introduced. The chapter covers the forward problems associated with these methods, explaining how the boundary measurements relate to the internal electrical properties of the object. It also delves into the inverse problem, which involves reconstructing the electrical properties from the boundary measurements. Additionally, the chapter introduces deep ANN as a potential tool for electrical tomographic imaging. By providing this foundational knowledge, Chapter 2 establishes the basis for the subsequent modifications and enhancements to the solvers discussed in later chapters.

Chapter 3 presents an integrated non-destructive anisotropic characterization and ERT solver for defect detection in an electrically anisotropic CFRP laminate. The chapter considers the

anisotropic properties resulting from UD plies and misalignments and investigates their impact on the ERT solver. The anisotropic ERT solver demonstrates superior performance in damage assessment compared to classical ERT, delivering solutions with reduced shape deformations, position errors, and artifacts. The advantages of the anisotropic ERT solver for anisotropic materials are discussed through simulations and experiments. The chapter also explores different current injection patterns, highlighting the effectiveness of the opposite pattern in accurately localizing and quantifying defects located far from boundary electrodes.

The contribution of this chapter goes beyond the development of the anisotropic ERT solver for defect detection in CFRP laminates. The approach also incorporates a non-invasive method to obtain the anisotropic properties, making it highly applicable for industrial inspection purposes. This chapter provides a comprehensive examination of the differences between the classical ERT solver and the anisotropic solver, starting from the forward problem and considering the variations in measurements. Additionally, the investigation of different current injection patterns offers valuable insights for future applications, aiming to achieve more accurate and effective inspection results. By addressing the challenges associated with anisotropic materials and exploring advanced techniques, this chapter lays the foundation for enhancing defect detection and assessment capabilities in various industrial sectors.

In chapter 4, significant contributions were made in the field of electrical tomographic imaging on lattice structures. This chapter has demonstrated the effectiveness of a 3D ERT method for quantitative defect detection in lattice structures by incorporating a strut-based normalized sensitivity map and an adjusted absolute imaging method. Both simulations and experiments have validated the enhanced performance of this method in localizing defects with smaller image errors and accurately assessing damage severity. The results highlight the strong consistency between the

reconstructed conductivity within a strut and the actual damage. This chapter addresses two key challenges associated with lattice structures: low central sensitivity of traditional imaging methods and the quantitative damage detection in topologically ordered geometries. By incorporating a strut-based normalized sensitivity map, this chapter provides a direct solution to compensate for the low central sensitivity and improve the localization of damage in central struts. This advancement has significant influence on quality assessment in industrial manufacturing process, where precise defect detection is crucial. Moreover, the proposed adjusted absolute imaging technique offers a direct and quantitative assessment of damage severity. This is particularly valuable in lattice structures with thin struts, where it is challenging to accurately localize the exact location of damage. The ability to obtain quantitative values for damage severity enhances the precision and effectiveness of defect assessment. The improved defect detection and quantification capabilities provided by this chapter have the potential to enhance the structural integrity and reliability of lattice structures in real-world applications.

Chapter 5 introduced EIT which considers the complex impedance/conductivity of the material. This shift allows for a more comprehensive understanding of the electrical properties and behavior of the inspected material. The MWCNT-based smart paint developed in the chapter exhibits complex conductivity that varies with frequency. This unique characteristic enables the application of fdEIT, which eliminates the need for baseline measurements and enhances the accuracy of damage detection.

Moreover, this thesis also makes a significant contribution by exploring the application of deep ANN in electrical tomographic methods. In chapter 4 to 6, deep ANN models were integrated into ERT, EIT and ECT methods to enhance their efficiency and accuracy. Several simplification techniques were employed to optimize the deep ANN models, such as reducing the complexity of

the network architecture. These simplification methods not only improve the computational efficiency of the deep ANN models but also maintain their effectiveness in capturing the electrical properties perturbations. By harnessing the power of deep ANN models, this research opens up new avenues for faster and more reliable electrical tomographic imaging, making it highly applicable in real-time industrial inspections, large-scale structural monitoring, and other time-sensitive applications.

In chapter 4, an ERT-ANN system has been proposed for detecting and localizing defects in conductive lattice structures. The system utilizes two deep ANN, deep ANN-I for identifying damaged struts and deep ANN-II for determining the location of damage within the struts. Training of the ERT-ANN system using simulated data and subsequent experiments using conductive thin film coated lattice structures have demonstrated its capability to accurately locate damaged struts and identify the specific portions of each strut that are damaged. The data-driven ERT method presented in this chapter offers a valuable tool for reconstructing the conductivity distribution of complex 3D lattice structures and detecting conductivity decreases associated with various forms of damage. The integration of deep ANN techniques further enhances the effectiveness and efficiency of the fdEIT process in chapter 5, allowing for accurate and reliable damage and strain detection. Both simulations and experiments have demonstrated the effectiveness of the proposed method.

In Chapter 6, the integration of deep ANN techniques contributes to enhance the system's efficiency for damage detection in CFRP panels. This chapter explored the use of reduced measurements, specifically the H/V/D measurements, which proved to be effective in reducing measurement time while maintaining detection accuracy. The combination of deep ANN

algorithms and the utilization of reduced measurements in the planar ECT system offers a promising approach for damage detection on CFRP structures.

7.2 Future Research

The findings and developments presented in this thesis open up avenues for future research in the field of tomographic imaging and damage detection. In addition to the 2D ERT on composite structures, the development of a 3D anisotropic ERT method that can accurately account for through-thickness anisotropy could be one area of future exploration. This would involve refining the modeling approach and incorporating detailed models to capture the complex behavior of materials in three dimensions. Additionally, investigating the ability of the ERT method to detect defect propagation would be valuable for understanding how damage spreads within a structure and how it impacts its overall integrity.

Another promising area for future research is the exploration of multi-modal imaging using EIT or ECT. Both EIT and ECT techniques capture information about the electrical conductivity and permittivity of the inspected material. By acquiring voltage phase information in addition to the traditional measurements, it becomes possible to obtain a more comprehensive characterization of the material's electrical properties. This multi-modal approach opens up opportunities for advanced image processing techniques to be applied. By leveraging the combined reconstructions from one set of measurements, image processing algorithms can be employed to enhance the accuracy and resolution of defect detection and localization. Furthermore, the use of nanocomposite thin films that are sensitive to specific stimuli, such as corrosion or other damage modes, can be incorporated into the multi-modal imaging framework. By introducing these specialized films to the inspected material, it becomes possible to obtain multiple damage mode

reconstructions. This multi-modal approach, incorporating voltage amplitude and phase information, advanced image processing techniques, and the use of stimuli-responsive thin films, has the potential to revolutionize defect detection and characterization in various industries. It can provide more accurate and detailed reconstructions of complex damage scenarios, enabling proactive maintenance and improved decision-making in structural integrity assessments.

Moreover, the application of machine learning on electrical tomographic method could be further investigated. Firstly, the method can be evaluated and validated on more complex damage scenarios and varying levels of damage severities. By expanding the range of simulated and experimental cases, a comprehensive assessment of the method's effectiveness and versatility can be achieved. In addition, the training process of the machine learning models can be enriched by incorporating experimental results into the training dataset. This can provide real-world data that better represents the complexities and variabilities encountered in practical scenarios. By integrating experimental results, the models can be further refined and fine-tuned to improve their accuracy and robustness. Another avenue for future research is the exploration of transfer learning techniques. Transfer learning allows the knowledge gained from training on one dataset or structure to be transferred and adapted to another dataset or structure. By leveraging pre-trained models or learned features, the training process can be accelerated, and the model's performance can be improved even with limited data. Transfer learning can facilitate the adaptation of machine learning-based damage detection methods to various inspected materials and structures, enabling faster deployment and wider applicability.

In summary, future research in tomographic imaging should strive to address the limitations of existing methods, explore multi-modal imaging approaches, develop real-time imaging systems, and expand the application of these techniques to new industries and materials.

REFERENCE

1. TODOROKI, A.; UEDA, M.; HIRANO, Y. Strain and Damage Monitoring of CFRP Laminates by Means of Electrical Resistance Measurement. *J. Solid Mech. Mater. Eng.* **2007**, *1*, 947–974, doi:10.1299/jmmp.1.947.

2. Hegde, S.; Satish Shenoy, B.; Chethan, K.N. Review on Carbon Fiber Reinforced Polymer (CFRP) and Their Mechanical Performance. *Mater. Today Proc.* **2019**, *19*, 658–662, doi:10.1016/j.matpr.2019.07.749.

3. Zadpoor, A.A. Mechanical Performance of Additively Manufactured Meta-Biomaterials. *Acta Biomater.* **2019**, *85*, 41–59, doi:10.1016/j.actbio.2018.12.038.

4. Crupi, V.; Epasto, G.; Guglielmino, E. Comparison of Aluminium Sandwiches for Lightweight Ship Structures: Honeycomb vs. Foam. *Mar. Struct.* **2013**, *30*, 74–96, doi:10.1016/j.marstruc.2012.11.002.

5. Kang, H.; Kim, J. Damage Mitigation of a Steel Column Subjected to Automobile Collision Using a Honeycomb Panel. *J. Perform. Constr. Facil.* **2020**, *34*, 04019107, doi:10.1061/(asce)cf.1943-5509.0001394.

6. Yan, C.; Hao, L.; Hussein, A.; Young, P.; Raymont, D. Advanced Lightweight 316L Stainless Steel Cellular Lattice Structures Fabricated via Selective Laser Melting. *Mater. Des.* **2014**, *55*, 533–541, doi:10.1016/j.matdes.2013.10.027.

7. Tang, S.; Hu, C. Design, Preparation and Properties of Carbon Fiber Reinforced Ultra-High Temperature Ceramic Composites for Aerospace Applications: A Review. *J. Mater. Sci. Technol.* **2017**, *33*, 117–130, doi:10.1016/j.jmst.2016.08.004.

8. Altin Karataş, M.; Gökkaya, H. A Review on Machinability of Carbon Fiber Reinforced Polymer (CFRP) and Glass Fiber Reinforced Polymer (GFRP) Composite Materials. *Def. Technol.* **2018**, *14*, 318–326, doi:10.1016/j.dt.2018.02.001.

9. Sayam, A.; Rahman, A.N.M.M.; Rahman, M.S.; Smriti, S.A.; Ahmed, F.; Rabbi, M.F.; Hossain, M.; Faruque, M.O. *A Review on Carbon Fiber-Reinforced Hierarchical Composites: Mechanical Performance, Manufacturing Process, Structural Applications and Allied Challenges*; Springer Nature Singapore, 2022; Vol. 32; ISBN 0123456789.

10. Liu, H.; Xiao, Z.; Zhao, X.L.; Al-Mahaidi, R. Prediction of Fatigue Life for CFRP-Strengthened Steel Plates. *Thin-Walled Struct.* **2009**, *47*, 1069–1077, doi:10.1016/j.tws.2008.10.011.

11. Zhou, J.; Shrotriya, P.; Soboyejo, W.O. On the Deformation of Aluminum Lattice Block Structures: From Struts to Structures. *Mech. Mater.* **2004**, *36*, 723–737, doi:10.1016/j.mechmat.2003.08.007.

12. Queheillalt, D.T.; Wadley, H.N.G. Titanium Alloy Lattice Truss Structures. *Mater. Des.* **2009**, *30*, 1966–1975, doi:10.1016/j.matdes.2008.09.015.

13. Helou, M.; Kara, S. Design, Analysis and Manufacturing of Lattice Structures: An Overview. *Int. J. Comput. Integr. Manuf.* **2018**, *31*, 243–261, doi:10.1080/0951192X.2017.1407456.

14. Yin, H.; Zhang, W.; Zhu, L.; Meng, F.; Liu, J.; Wen, G. Review on Lattice Structures for Energy Absorption Properties. *Compos. Struct.* **2023**, *304*, 116397, doi:10.1016/j.compstruct.2022.116397.

15. Abry, J.C.; Choi, Y.K.; Chateauminois, A.; Dalloz, B.; Giraud, G.; Salvia, M. In-Situ Monitoring of Damage in CFRP Laminates by Means of AC and DC Measurements. *Compos. Sci. Technol.* **2001**, *61*, 855–864, doi:10.1016/S0266-3538(00)00181-0.

16. Ghobadi, A. Common Type of Damages in Composites and Their Inspections. *World J. Mech.* **2017**, *07*, 24–33, doi:10.4236/wjm.2017.72003.

17. Tran, H.T.; Liang, X.; To, A.C. Efficient Prediction of Cracking at Solid-Lattice Support Interface during Laser Powder Bed Fusion via Global-Local J-Integral Analysis Based on Modified Inherent Strain Method and Lattice Support Homogenization. *Addit. Manuf.* **2020**, *36*, 101590, doi:10.1016/j.addma.2020.101590.

18. Echeta, I.; Feng, X.; Dutton, B.; Leach, R.; Piano, S. Review of Defects in Lattice Structures Manufactured by Powder Bed Fusion. *Int. J. Adv. Manuf. Technol.* **2020**, *106*, 2649–2668, doi:10.1007/s00170-019-04753-4.

19. Wu, Y.; Yang, L. Elastic and Failure Characteristics of Additive Manufactured Thin Wall Lattice Structures with Defects. *Thin-Walled Struct.* **2021**, *161*, 107493, doi:10.1016/j.tws.2021.107493.

20. Visal, S. A Review Paper on Properties of Carbon Fiber Reinforced Polymers Power Generation Using Rumblers View Project Design and Analysis of Solar Structural and Mountings for Solar Panel View Project Swapnil Deokar A Review Paper on Properties of Carbon Fiber Re. **2016**, *2*, 238–243.

21. Kim, D.W.; Lim, J.H.; Kim, S.W.; Kim, Y.H. Micro-Computed Tomography-Aided Modeling for Misaligned and Noncircular Fibers of Unidirectional Composites and Validation under a Transverse Tensile Loading. *Compos. Sci. Technol.* **2021**, *212*, 108879, doi:10.1016/j.compscitech.2021.108879.

22. Gupta, S.; Kim, H. (eric); Kim, H.; Loh, K.J. Planar Capacitive Imaging for Composite Delamination Damage Characterization. *Meas. Sci. Technol.* **2020**, *32*, doi:10.1088/1361-6501/abb484.

23. Alam, P.; Mamalis, D.; Robert, C.; Floreani, C.; Ó Brádaigh, C.M. The Fatigue of Carbon Fibre Reinforced Plastics - A Review. *Compos. Part B Eng.* **2019**, *166*, 555–579, doi:10.1016/j.compositesb.2019.02.016.

24. Fawzia, S.; Kabir, M.H. A Review on Environmental Durability of CFRP Strengthened System. *Australas. Struct. Eng. Conf. 2012 past, Present Futur. Struct. Eng.* **2012**, 416.

25. Sennewald, C., Kaina, S., Weck, D., Gruhl, A., Thieme, M., Hoffmann, G., Stephani, G., Böhm, R., Cherif, C., Andersen, O. and Kieback, B. Metal Sandwiches and Metal-Matrix-Composites Based on 3D Woven Wire Structures for Hybrid Lightweight Construction. *Adv. Eng. Mater.* **2014**, *16*, 1234–1242, doi:10.1002/adem.201400180.

26. Jiang, S.; Sun, F.; Zhang, X.; Fan, H. Interlocking Orthogrid: An Efficient Way to Construct Lightweight Lattice-Core Sandwich Composite Structure. *Compos. Struct.* **2017**, *176*, 55–71, doi:10.1016/j.compstruct.2017.05.029.

27. Park, S.I.; Rosen, D.W.; Choi, S. kyum; Duty, C.E. Effective Mechanical Properties of Lattice Material Fabricated by Material Extrusion Additive Manufacturing. *Addit. Manuf.* **2014**, *1*, 12–23, doi:10.1016/j.addma.2014.07.002.

28. Nagesha, B.K.; Dhinakaran, V.; Varsha Shree, M.; Manoj Kumar, K.P.; Chalawadi, D.; Sathish, T. Review on Characterization and Impacts of the Lattice Structure in Additive Manufacturing. *Mater. Today Proc.* **2020**, *21*, 916–919, doi:10.1016/j.matpr.2019.08.158.

29. Dong, G.; Wijaya, G.; Tang, Y.; Zhao, Y.F. Optimizing Process Parameters of Fused Deposition Modeling by Taguchi Method for the Fabrication of Lattice Structures. *Addit. Manuf.* **2018**, *19*, 62–72, doi:10.1016/j.addma.2017.11.004.

30. Dar, U.A.; Mian, H.H.; Abid, M.; Topa, A.; Sheikh, M.Z.; Bilal, M. Experimental and Numerical Investigation of Compressive Behavior of Lattice Structures Manufactured through Projection Micro Stereolithography. *Mater. Today Commun.* **2020**, *25*, 101563, doi:10.1016/j.mtcomm.2020.101563.

31. Tan, C.; Li, S.; Essa, K.; Jamshidi, P.; Zhou, K.; Ma, W.; Attallah, M.M. Laser Powder Bed Fusion of Ti-Rich TiNi Lattice Structures: Process Optimisation, Geometrical Integrity, and Phase Transformations. *Int. J. Mach. Tools Manuf.* **2019**, *141*, 19–29, doi:10.1016/j.ijmachtools.2019.04.002.

32. Lewis, J.A. Direct Ink Writing of 3D Functional Materials. *Adv. Funct. Mater.* **2006**, *16*, 2193–2204, doi:10.1002/adfm.200600434.

33. Leung, C.K.Y.; Elvin, N.; Olson, N.; Morse, T.F.; He, Y.F. A Novel Distributed Optical Crack Sensor for Concrete Structures. *Eng. Fract. Mech.* **2000**, *65*, 133–148, doi:10.1016/s0013-7944(99)00112-5.

34. Glisic, B.; Inaudi, D. Development of Method for In-Service Crack Detection Based on Distributed Fiber Optic Sensors. *Struct. Heal. Monit.* **2012**, *11*, 161–171, doi:10.1177/1475921711414233.

35. Tuttle, M.E.; Brinson, H.F. Resistance-Foil Strain-Gage Technology as Applied to Composite Materials. *Exp. Mech.* **1984**, *24*, 54–65, doi:10.1007/BF02323207.

36. Das, A.K.; Leung, C.K.Y.; Wan, K.T. Application of Deep Convolutional Neural Networks for Automated and Rapid Identification and Computation of Crack Statistics of Thin Cracks in Strain Hardening Cementitious Composites (SHCCs). *Cem. Concr.*

Compos. **2021**, *122*, 104159, doi:10.1016/j.cemconcomp.2021.104159.

37. Mohan, A.; Poobal, S. Crack Detection Using Image Processing: A Critical Review and Analysis. *Alexandria Eng. J.* **2018**, *57*, 787–798, doi:10.1016/j.aej.2017.01.020.

38. Dung, C.V.; Sekiya, H.; Hirano, S.; Okatani, T.; Miki, C. A Vision-Based Method for Crack Detection in Gusset Plate Welded Joints of Steel Bridges Using Deep Convolutional Neural Networks. *Autom. Constr.* **2019**, *102*, 217–229, doi:10.1016/j.autcon.2019.02.013.

39. Gholizadeh, S. A Review of Non-Destructive Testing Methods of Composite Materials. *Procedia Struct. Integr.* **2016**, *1*, 50–57, doi:10.1016/j.prostr.2016.02.008.

40. D'Orazio, T.; Leo, M.; Distante, A.; Guaragnella, C.; Pianese, V.; Cavaccini, G. Automatic Ultrasonic Inspection for Internal Defect Detection in Composite Materials. *NDT E Int.* **2008**, *41*, 145–154, doi:10.1016/j.ndteint.2007.08.001.

41. Singh, A.K.; Berggren, S.; Zhu, Y.; Han, M.; Huang, H. Simultaneous Strain and Temperature Measurement Using a Single Fiber Bragg Grating Embedded in a Composite Laminate. *Smart Mater. Struct.* **2017**, *26*, doi:10.1088/1361-665X/aa91ab.

42. Dhital, D.; Lee, J.R. A Fully Non-Contact Ultrasonic Propagation Imaging System for Closed Surface Crack Evaluation. *Exp. Mech.* **2012**, *52*, 1111–1122, doi:10.1007/s11340-011-9567-z.

43. Honarvar, F.; Varvani-Farahani, A. A Review of Ultrasonic Testing Applications in Additive Manufacturing: Defect Evaluation, Material Characterization, and Process Control. *Ultrasonics* **2020**, *108*, 106227, doi:10.1016/j.ultras.2020.106227.

44. Gupta, S.; Lin, Y.A.; Lee, H.J.; Buscheck, J.; Wu, R.; Lynch, J.P.; Garg, N.; Loh, K.J. In Situ Crack Mapping of Large-Scale Self-Sensing Concrete Pavements Using Electrical Resistance Tomography. *Cem. Concr. Compos.* **2021**, *122*, 104154, doi:10.1016/j.cemconcomp.2021.104154.

45. Hou, T.C.; Lynch, J.P. Electrical Impedance Tomographic Methods for Sensing Strain Fields and Crack Damage in Cementitious Structures. *J. Intell. Mater. Syst. Struct.* **2009**, *20*, 1363–1379, doi:10.1177/1045389X08096052.

46. Griffith, W.I. The Accelerated Characterization of Viscoelastic Composite Materials. *Virginia Polytech. Inst. State Univ.* **1980**.

47. Kanerva, M.; Antunes, P.; Sarlin, E.; Orell, O.; Jokinen, J.; Wallin, M.; Brander, T.; Vuorinen, J. Direct Measurement of Residual Strains in CFRP-Tungsten Hybrids Using Embedded Strain Gauges. *Mater. Des.* **2017**, *127*, 352–363, doi:10.1016/j.matdes.2017.04.008.

48. Gopalakrishnan, K.; Khaitan, S.K.; Choudhary, A.; Agrawal, A. Deep Convolutional Neural Networks with Transfer Learning for Computer Vision-Based Data-Driven

Pavement Distress Detection. *Constr. Build. Mater.* **2017**, *157*, 322–330, doi:10.1016/j.conbuildmat.2017.09.110.

49. Usamentiaga, R.; Venegas, P.; Guerediaga, J.; Vega, L.; López, I. Automatic Detection of Impact Damage in Carbon Fiber Composites Using Active Thermography. *Infrared Phys. Technol.* **2013**, *58*, 36–46, doi:10.1016/j.infrared.2013.01.004.

50. He, Y.; Deng, B.; Wang, H.; Cheng, L.; Zhou, K.; Cai, S.; Ciampa, F. Infrared Machine Vision and Infrared Thermography with Deep Learning: A Review. *Infrared Phys. Technol.* **2021**, *116*, 103754, doi:10.1016/j.infrared.2021.103754.

51. Thompson, A.; Maskery, I.; Leach, R.K. X-Ray Computed Tomography for Additive Manufacturing: A Review. *Meas. Sci. Technol.* **2016**, *27*, doi:10.1088/0957-0233/27/7/072001.

52. Gupta, S.; Gonzalez, J.G.; Loh, K.J. Self-Sensing Concrete Enabled by Nano-Engineered Cement-Aggregate Interfaces. *Struct. Heal. Monit.* **2017**, *16*, 309–323, doi:10.1177/1475921716643867.

53. Brown, B.H. Electrical Impedance Tomography (EIT): A Review. *J. Med. Eng. Technol.* **2003**, *27*, 97–108, doi:10.1080/0309190021000059687.

54. Vauhkonen, M. *Electrical Impedance Tomography and Prior Information*; 1997; Vol. 14; ISBN 9517817002.

55. Schulte, K.; Baron, C. Load and Failure Analyses of CFRP Laminates by Means of Electrical Resistivity Measurements. *Compos. Sci. Technol.* **1989**, *36*, 63–76, doi:10.1016/0266-3538(89)90016-X.

56. Dai, H.; Gallo, G.J.; Schumacher, T.; Thostenson, E.T. A Novel Methodology for Spatial Damage Detection and Imaging Using a Distributed Carbon Nanotube-Based Composite Sensor Combined with Electrical Impedance Tomography. *J. Nondestruct. Eval.* **2016**, *35*, 1–15, doi:10.1007/s10921-016-0341-0.

57. Loyola, B.R.; Saponara, V. La; Loh, K.J.; Briggs, T.M.; Bryan, G.O.; Skinner, J.L. Spatial Sensing Using Electrical Impedance Tomography. **2013**, *13*, 2357–2367.

58. Baltopoulos, A.; Polydorides, N.; Pambaguian, L.; Vavouliotis, A.; Kostopoulos, V. Damage Identification in Carbon Fiber Reinforced Polymer Plates Using Electrical Resistance Tomography Mapping. *J. Compos. Mater.* **2013**, *47*, 3285–3301, doi:10.1177/0021998312464079.

59. Schueler, R.; Joshi, S.P.; Schulte, K. Damage Detection in CFRP by Electrical Conductivity Mapping. *Compos. Sci. Technol.* **2001**, *61*, 921–930, doi:10.1016/S0266-3538(00)00178-0.

60. Shu, Y.; Mukherjee, S.; Chang, T.; Gilmore, A.; Tringe, J.W.; Stobbe, D.M.; Loh, K.J. Multi-Defect Detection in Additively Manufactured Lattice Structures Using 3D Electrical

Resistance Tomography. *Sensors* **2022**, *22*, doi:10.3390/s22239167.

61. Li, Y.; Soleimani, M. Imaging Conductive Materials with High Frequency Electrical Capacitance Tomography. *Meas. J. Int. Meas. Confed.* **2013**, *46*, 3355–3361, doi:10.1016/j.measurement.2013.05.020.

62. Gupta, S.; Loh, K.J. Noncontact Electrical Permittivity Mapping and PH-Sensitive Films for Osseointegrated Prosthesis and Infection Monitoring. *IEEE Trans. Med. Imaging* **2017**, *36*, 2193–2203, doi:10.1109/TMI.2017.2707390.

63. Wenru Fan, C.W. Damage Detection for CFRP Based on Planar Electrical Capacitance Tomography. *Struct. Durab. Heal. Monit.* **2020**, *14*, 303, doi:10.32604/SDHM.2020.011009.

64. Harley, J.B.; Sparkman, D. Machine Learning and NDE: Past, Present, and Future. **2020**, *090001*.

65. Hopfield, J.J. Artificial Neural Networks. *IEEE Circuits Devices Mag.* **1988**, *4*, 3–10.

66. Quqa, S.; Shu, Y.; Li, S.; Loh, K.J. Pressure Mapping Using Nanocomposite-Enhanced Foam and Machine Learning. *Front. Mater.* **2022**, *9*, 1–12, doi:10.3389/fmats.2022.862796.

67. Hallaji, M.; Seppänen, A.; Pour-Ghaz, M. Electrical Impedance Tomography-Based Sensing Skin for Quantitative Imaging of Damage in Concrete. *Smart Mater. Struct.* **2014**, *23*, doi:10.1088/0964-1726/23/8/085001.

68. Holder, David S., E. *Electrical Impedance Tomography: Methods, History and Applications*; CRC Press, 2004;

69. Vauhkonen, M.; Vadâsz, D.; Karjalainen, P.A.; Somersalo, E.; Kaipio, J.P. Tikhonov Regularization and Prior Information in Electrical Impedance Tomography. *IEEE Trans. Med. Imaging* **1998**, *17*, 285–293, doi:10.1109/42.700740.

70. Wu, C.; Soleimani, M. Frequency Difference EIT with Localization: A Potential Medical Imaging Tool during Cancer Treatment. *IEEE Access* **2019**, *7*, 21870–21878, doi:10.1109/ACCESS.2019.2898091.

71. Borsic, A.; Graham, B.; Adler, A.; Lionheart, W. Total Variation Regularization in Electrical Impedance Tomography. **2007**.

72. Zhao, Y.; Gschossmann, S.; Schagerl, M.; Gruener, P.; Kralovec, C. Characterization of the Spatial Elastoresistivity of Inkjet-Printed Carbon Nanotube Thin Films. *Smart Mater. Struct.* **2018**, *27*, doi:10.1088/1361-665X/aad8f1.

73. D. N. Dyck, D.A.L. A Method of Computing the Sensitivity of Electromagnetic Quantities to Changes in Materials and Sources. *IEEE Trans. Magn.* **1994**, *30*, 3415–3418.

74. Zhao, Y.; Schagerl, M.; Gschossmann, S.; Kralovec, C. In Situ Spatial Strain Monitoring of a Single-Lap Joint Using Inkjet-Printed Carbon Nanotube Embedded Thin Films. **2018**, doi:10.1177/1475921718805963.

75. Li, S.; Shu, Y.; Lin, Y.-A.; Zhao, Y.; Yeh, Y.-J.; Chiang, W.-H.; Loh, K.J. Distributed Strain Monitoring Using Nanocomposite Paint Sensing Meshes. *Sensors* **2022**, *22*, 812, doi:10.3390/s22030812.

76. Gupta, S.; Vella, G.; Yu, I.N.; Loh, C.H.; Chiang, W.H.; Loh, K.J. Graphene Sensing Meshes for Densely Distributed Strain Field Monitoring. *Struct. Heal. Monit.* **2020**, *19*, 1323–1339, doi:10.1177/1475921719877418.

77. Nonn, S.; Schagerl, M.; Zhao, Y.; Gschossmann, S.; Kralovec, C. Application of Electrical Impedance Tomography to an Anisotropic Carbon Fiber-Reinforced Polymer Composite Laminate for Damage Localization. *Compos. Sci. Technol.* **2018**, *160*, 231–236, doi:10.1016/j.compscitech.2018.03.031.

78. Hamilton, S.J.; Lassas, M.; Siltanen, S. A Direct Reconstruction Method for Anisotropic Electrical Impedance Tomography. *Inverse Probl.* **2014**, *30*, 0–33, doi:10.1088/0266-5611/30/7/075007.

79. Zhao, Y.; Gschossmann, S.; Schagerl, M.; Gruener, P.; Kralovec, C. Characterization of the Spatial Elastoresistivity of Inkjet-Printed Carbon Nanotube Thin Films. *Smart Mater. Struct.* **2018**, *27*, 105009, doi:10.1088/1361-665X/aad8f1.

80. Abascal, J.F.P.J.; Arridge, S.R.; Atkinson, D.; Horesh, R.; Fabrizi, L.; De Lucia, M.; Horesh, L.; Bayford, R.H.; Holder, D.S. Use of Anisotropic Modelling in Electrical Impedance Tomography; Description of Method and Preliminary Assessment of Utility in Imaging Brain Function in the Adult Human Head. *Neuroimage* **2008**, *43*, 258–268, doi:10.1016/j.neuroimage.2008.07.023.

81. Gao, X.; Wei, T.; Dong, H.; Song, Y. Damage Detection in 2.5D C/SiC Composites Using Electrical Resistance Tomography. *J. Eur. Ceram. Soc.* **2019**, *39*, 3583–3593, doi:10.1016/j.jeurceramsoc.2019.04.046.

82. De Baere, I.; Van Paepegem, W.; Degrieck, J. The Use of Rivets for Electrical Resistance Measurement on Carbon Fibre-Reinforced Thermoplastics. *Smart Mater. Struct.* **2007**, *16*, 1821–1828, doi:10.1088/0964-1726/16/5/037.

83. Dos Santos, C.A.M.; De Campos, A.; Da Luz, M.S.; White, B.D.; Neumeier, J.J.; De Lima, B.S.; Shigue, C.Y. Procedure for Measuring Electrical Resistivity of Anisotropic Materials: A Revision of the Montgomery Method. *J. Appl. Phys.* **2011**, *110*, doi:10.1063/1.3652905.

84. Hinckley, M. Statistical Evaluation of the Variation in Laminated Composite Properties Resulting from Ply Misalignment. *Adv. Opt. Struct. Syst.* **1990**, *1303*, 497, doi:10.1117/12.21532.

85. Yurgartis, S.W. Measurement of Small Angle Fiber Misalignments in Continuous Fiber Composites. *Compos. Sci. Technol.* **1987**, *30*, 279–293, doi:10.1016/0266-3538(87)90016-9.

86. Adler A, Arnold JH, Bayford R, Borsic A, Brown B, Dixon P, Faes TJ, Frerichs I, Gagnon H, Gärber Y, Grychtol B. GREIT: A Unified Approach to 2D Linear EIT Reconstruction of Lung Images. *Physiol. Meas.* **2009**, *30*, 34–55, doi:10.1088/0967-3334/30/6/S03.

87. Gupta, S.; Lee, H.J.; Loh, K.J.; Todd, M.D.; Reed, J.; Drew Barnett, A. Noncontact Strain Monitoring of Osseointegrated Prostheses. *Sensors (Switzerland)* **2018**, *18*, doi:10.3390/s18093015.

88. Gallo, G.J.; Thostenson, E.T. Spatial Damage Detection in Electrically Anisotropic Fiber-Reinforced Composites Using Carbon Nanotube Networks. *Compos. Struct.* **2016**, *141*, 14–23, doi:10.1016/j.compstruct.2015.07.082.

89. Thomas, A.J.; Kim, J.J.; Tallman, T.N.; Bakis, C.E. Damage Detection in Self-Sensing Composite Tubes via Electrical Impedance Tomography. *Compos. Part B Eng.* **2019**, *177*, 107276, doi:10.1016/j.compositesb.2019.107276.

90. Li, H.; Cao, L.; Xu, C.; Liu, B.; Yang, B.; Dong, X.; Fu, F. Optimized Method for Electrical Impedance Tomography to Image Large Area Conductive Perturbation. *IEEE Access* **2019**, *7*, 140734–140742, doi:10.1109/ACCESS.2019.2944209.

91. Polydorides, N.; McCann, H. Electrode Configurations for Improved Spatial Resolution in Electrical Impedance Tomography. *Meas. Sci. Technol.* **2002**, *13*, 1862–1870, doi:10.1088/0957-0233/13/12/309.

92. Ren, S.; Wang, Y.; Liang, G.; Dong, F. A Robust Inclusion Boundary Reconstructor for Electrical Impedance Tomography with Geometric Constraints. *IEEE Trans. Instrum. Meas.* **2019**, *68*, 762–773, doi:10.1109/TIM.2018.2853358.

93. Mortensen, L.P.; Ryu, D.; Zhao, Y.; Loh, K.J. Rapid Assembly of Multifunctional Thin Film Sensors for Wind Turbine Blade Monitoring. *Key Eng. Mater.* **2013**, *569–570*, 515–522, doi:10.4028/www.scientific.net/KEM.569-570.515.

94. Wang, L.; Loh, K.J.; Brely, L.; Bosia, F.; Pugno, N.M. An Experimental and Numerical Study on the Mechanical Properties of Carbon Nanotube-Latex Thin Films. *J. Eur. Ceram. Soc.* **2016**, *36*, 2255–2262, doi:10.1016/j.jeurceramsoc.2015.12.052.

95. Pérez, M.A.; Font-Moré, J.; Fernández-Esmerats, J. Structural Damage Assessment in Lattice Towers Based on a Novel Frequency Domain-Based Correlation Approach. *Eng. Struct.* **2021**, *226*, doi:10.1016/j.engstruct.2020.111329.

96. Rathore, J.S.; Vienne, C.; Quinsat, Y.; Tournier, C. Influence of Resolution on the X-Ray CT-Based Measurements of Metallic AM Lattice Structures. *Weld. World* **2020**, *64*, 1367–1376, doi:10.1007/s40194-020-00920-4.

97. Lin, Y.A.; Zhao, Y.; Wang, L.; Park, Y.; Yeh, Y.J.; Chiang, W.H.; Loh, K.J. Graphene K-Tape Meshes for Densely Distributed Human Motion Monitoring. *Adv. Mater. Technol.* **2021**, *6*, 1–9, doi:10.1002/admt.202000861.

98. Zhu, L. Research and Implementation of SVD in Machine Learning. **2017**, 471–475.

99. Loyola, B.R.; Briggs, T.M.; Arronche, L.; Loh, K.J.; La Saponara, V.; O'Bryan, G.; Skinner, J.L. Detection of Spatially Distributed Damage in Fiber-Reinforced Polymer Composites. *Struct. Heal. Monit.* **2013**, *12*, 225–239, doi:10.1177/1475921713479642.

100. Ray, B.C.; Rathore, D. Environmental Damage and Degradation of FRP Composites: A Review Report. *Polym. Compos.* **2015**, *36*, 410–423, doi:10.1002/pc.

101. Collings, T.A.; Stone, D.E.W. Hygrothermal Effects in CFC Laminates: Damaging Effects of Temperature, Moisture and Thermal Spiking. *Compos. Struct.* **1985**, *3*, 341–378, doi:10.1016/0263-8223(85)90061-3.

102. Loh, K.J.; Azhari, F. Recent Advances in Skin-Inspired Sensors Enabled by Nanotechnology. *Jom* **2012**, *64*, 793–801, doi:10.1007/s11837-012-0358-5.

103. Dai, H.; Thostenson, E.T.; Schumacher, T. Processing and Characterization of a Novel Distributed Strain Sensor Using Carbon Nanotube-Based Nonwoven Composites. *Sensors (Switzerland)* **2015**, *15*, 17728–17747, doi:10.3390/s150717728.

104. Jun, S.C.; Kuen, J.; Lee, J.; Woo, E.J.; Holder, D.; Seo, J.K. Frequency-Difference EIT (FdEIT) Using Weighted Difference and Equivalent Homogeneous Admittivity: Validation by Simulation and Tank Experiment. *Physiol. Meas.* **2009**, *30*, 1087–1099, doi:10.1088/0967-3334/30/10/009.

105. Li, X.; Zhou, Y.; Wang, J.; Wang, Q.; Lu, Y.; Duan, X.; Sun, Y.; Zhang, J.; Liu, Z. A Novel Deep Neural Network Method for Electrical Impedance Tomography. *Trans. Inst. Meas. Control* **2019**, *41*, 4035–4049, doi:10.1177/0142331219845037.